POST-EARTHQUAKE FIRE PERFORMANCE ANALYSIS OF FIRE DOORS IN TALL BUILDINGS

by

Muhammet Çalayır

B.S., Civil Engineering, Kocaeli University, 2017

Submitted to the Institute for Graduate Studies in
Science and Engineering in partial fulfillment of
the requirements for the degree of
Master of Science

Graduate Program in Civil Engineering

Boğaziçi University

2021

To my mother

ACKNOWLEDGEMENTS

Over and above all, I owe a great debt of thanks to my mother, Nezihe Çalayır, for her unconditional love, confidence in me, and the innumerable efforts she made in my whole life. I shall never have adequate words to thank her for providing such a solid foundation and supporting me at my crossroads in pursuing an academic career.

I would like to extend my sincere gratitude to my supervisor, Prof. Serdar Selamet, for his persistent guidance, understanding, and commitment to my Master's research.

I express my deepest appreciation to Prof. Serdar Soyöz and Prof. Alper İlki for serving on my committee, reviewing my thesis, and providing me with insightful comments.

I owe a great depth of gratitude to Assoc. Prof. Seval Pınarbaşı Çuhadaroğlu and Assoc. Prof. Fuad Okay for their advice and encouragement since my undergraduate studies.

I wish to place on record a special thanks to Boğaziçi University Structures Laboratory's and TSE Laboratory's technicians. They have been very essential and helpful in allowing the distinguished experimental parts of this project to be completed.

The financial supports provided by Bogazici University Research Fund (13084-D) and Newton Collaborative Research Programme (NRCP1516/4/72) are truly appreciated.

Last but not least, I am grateful to Göktuğ Tüfekçi for always being the true friend of all bright and difficult times. As the only witness of the whole process of my challenges in both undergraduate and graduate years, his enthusiasm was invaluable in formulating the research questions coupled with insightful criticism. He raised precious points in our discussions and contributed to increasing the productivity of our daily coffee talks in front of the library and the online study sessions during the COVID-19 pandemic.

ABSTRACT

POST-EARTHQUAKE FIRE PERFORMANCE ANALYSIS OF FIRE DOORS IN TALL BUILDINGS

Seismic excitations prior to a fire incident can cause damage to passive fire safety systems such as fire-rated doors, posing a high level of risk for the fire protection of the residents and building property. Seismic cracks on corners and joints, as well as lateral distortions, can widen the clearances between the door leaf and its frame, resulting in the fire door set being ineffective in preventing the rapid spread of smoke and flame. This is likely to render the means of egress inoperable and compound escape times in a fire hazard, especially in heavily occupied tall buildings. Although some building codes require periodic inspections for fire doors not to surpass the allowed clearances, no specification for the technical investigations for potential damages to these devices after an earthquake is provided. In the scope of this research, the earthquake and post-earthquake fire performance of fire door specimens were examined through the numerical and experimental stages. A 40-story tall residential building was modeled and designed. The structural model was subjected to nonlinear time-history analyses to determine maximum inter-story drifts at various possible fire door locations on the typical floor plan. To determine damage states of the fire door assemblies, one-way static and displacement-controlled quasi-static reversed cyclic loadings were carried out by employing the maximum drift demands obtained in the numerical analyses. Tested and damaged 90-minute-rated fire doors were then exposed to the fire-resistance rating test to examine whether they would be capable during their standardized time of resistance. However, the resultant earthquake-induced damage predominantly caused up to 70% of the reduction in their fire-resistance rating. This study primarily demonstrates that fire doors, particularly those in tall buildings, should be inspected promptly for repair or replacement based on the extent of damage caused by moderate to major earthquakes.

ÖZET

YÜKSEK YAPILARDAKİ YANGIN KAPILARININ DEPREM SONRASI YANGIN PERFORMANS ANALİZİ

Yangına dayanıklı kapılar gibi pasif yangından koruma sistemlerinde, bir yangın olayından önce deprem etkileri nedeniyle meydana gelebilecek hasar, bina sakinlerinin ve bina mülkünün yangın güvenliği açısından kritik bir tehdit oluşturmaktadır. Kapı çerçevesinin köşelerinde ve birleşim bölgelerinde oluşabilecek sismik çatlaklar veya yanal çarpılmalar, kapı kanadı ile çerçevesi arasında boşlukların açılmasına neden olarak kapı sisteminin duman ve alevin hızla yayılmasını önlemede etkisiz kalmasına neden olabilir. Bu, özellikle insan ve eşya yoğunluğu fazla olan yüksek yapılarda, bir yangın tehlikesi durumunda, muhtemel kaçış planını etkisiz hale getirebilir ve tahliye sürelerini artırabilir. Bazı bina yönetmelikleri, yangın kapılarının izin verilen boşlukları aşmaması için periyodik muayeneler gerektirmesine rağmen, bir depremden sonra bu bölme elemanlarına gelebilecek olası hasarlara yönelik teknik denetlemeler için herhangi bir şartname yoktur. Bu araştırma kapsamında yangın kapı numunelerinin deprem ve deprem sonrası yangın performansı numerik ve deneysel aşamalarla incelendi. 40 katlı yüksek bir konut binası modellenip tasarlandı. Bina modeli, tipik kat planındaki olası yangın kapısı konumlarında maksimum göreli kat ötelemelerini belirlemek için zaman tanım alanında doğrusal olmayan analizlere tabi tutuldu. Yangın kapıları üzerindeki hasar seviyelerini belirlemek için, numerik analizlerde elde edilen maksimum göreli kat öteleme değerleri referans alınarak tek yönlü statik ve deplasman kontrollü yarı statik ters çevrimsel yüklemeler gerçekleştirildi. Test edilmiş ve hasar görmüş 90 dakika yangına dayanıklılık sertifikalı yangın kapıları, standart direnç süreleri boyunca etkili olup olmayacaklarını incelemek için yangına dayanıklılık derecelendirme testine tabi tutuldu. Sonuç olarak, deprem hasarının yangın kapılarının yangına dayanıklılık derecelerinde %70'e varan düşüşe neden olduğu kaydedildi. Bu çalışma, özellikle yüksek binalardaki yangın kapılarının orta derece ve üzeri şiddetteki depremlerden hemen sonra denetlenerek tespit edilen hasarın boyutuna bağlı olarak onarım veya değişim yapılması gerektiğini önermektedir.

TABLE OF CONTENTS

LIST OF FIGURES

LIST OF TABLES

LIST OF ACRONYMS/ABBREVIATIONS

2D	Two Dimensional
3D	Three Dimensional
AFAD	Disaster and Emergency Management Presidency
ASCE	American Society of Civil Engineers
ATC	Applied Technology Council
BS	British Standards
CFD	Computational Fluid Dynamics
CP	Collapse Prevention
CSI	Computers and Structures, Inc.
CTBUH	Council on Tall Buildings and Urban Habitat
FEA	Finite Element Analysis
FEMA	Federal Emergency Management Agency
FRR	Fire Resistance Rating
HRR	Heat Release Rate
IO	Immediate Occupancy
LATBSDC	Los Angeles Tall Buildings Structural Design Council
LS	Life Safety
MSE	Mean Squared Error
NFPA	National Fire Protection Association
NLTHA	Nonlinear Time History Analyses
NIST	National Institute of Standards and Technology
O	Operational
PBD	Performance-Based Design
PFP	Passive Fire Protection
PEER	Pacific Earthquake Engineering Research Center
SEAOC	Structural Engineers Association of California
SRSS	Square Root of the Sum of Squares
TBI	Tall Buildings Initiative
TBSC	Turkish Building Seismic Code
TS	Turkish Standards

LIST OF SYMBOLS

A_g	Cross-sectional area of a column
A_s	Total area of longitudinal reinforcements
A_{sh}	Total cross-sectional area of stirrups and ties in single spacing
a_i	Span length between longitudinal reinforcements for space no *i*
b_0	Width of confined core
b_w	Width of section
D	Over strength factor
d	Effective height of a section
E_c	Tangent modulus of elasticity of concrete
E_{ce}	Effective modulus of elasticity of concrete
$E_d^{(V)}$	Earthquake load in the vertical direction
E_s	Modulus of elasticity of reinforcing steel
E_{sec}	Secant modulus of elasticity of concrete
ε_{cc}	Strain at compressive strength of confined concrete
ε_{co}	Strain at compressive strength of unconfined concrete
f_c	Stress at concrete
f_{cc}	Compressive strength of confined concrete
f_{ce}	Expected compressive strength of concrete
f_{ck}	Characteristic compressive strength of concrete
f_{co}	Compressive strength of unconfined concrete
f_{csd}	Design shear strength of concrete
f_{cse}	Expected shear strength of concrete
f_{ctd}	Design tensile strength of concrete
f_{cte}	Expected tensile strength of concrete
f_e	Effective confining stress
f_{ex}	Effective confinement pressure on X direction
f_{ey}	Effective confinement pressure on Y direction
f_s	Stress at reinforcing steel
f_{su}	Ultimate strength of reinforcing steel

f_{sy}	Yield strength of reinforcing steel
f_{syd}	Design tensile strength of reinforcing steel
f_{sye}	Expected tensile strength of reinforcements
G	Gravitational constant
g	Gravitational constant
G_c	Shear modulus of concrete
G_{ce}	Effective shear modulus of concrete
h	Height of section
h_o	Height of confined core
k_e	Confinement effectiveness factor
L_F	Distance between closest active fault and project site
n	Live load contribution factor
m	Number of ground motion pairs
$m_j^{(s)}$	Seismic mass at node j
P	Maximum compressive load from nonlinear analysis
Q	Capacity
Q_y	Yield capacity
R	Structural behavior factor
R_{JB}	Joyner-Boore distance
r	Parameter defining shape of monotonic stress-strain curve of concrete
S_1	Spectral acceleration coefficient for 1s period
S_S	Spectral acceleration coefficient for short period
$S_{ae}(T)$	Elastic spectral acceleration at period T
S_{D1}	Design spectral acceleration coefficient for 1s period
S_{DS}	Design spectral acceleration coefficient for short period
s	Spacing between confinements
T	Natural vibration period
T	Temperature
t	Time
T_A	Left corner period for spectrum
T_B	Right corner period for spectrum
T_L	Constant spectral displacement range period limit

T_P	Fundamental period of the structure
V_{s30}	Shear wave velocity at first 30 m of soil
w_i	Weight of period
$w_j^{(s)}$	Seismic weight at node j
$w_{G,j}^{(s)}$	Seismic weight at node j from dead loads
$w_{Q,j}^{(s)}$	Seismic weight at node j from live loads
x	Ratio of strain to strain at compressive strength of confined concrete
a	Hilber-Hughes-Taylor Method coefficient
β	Hilber-Hughes-Taylor Method coefficient
Δ	Displacement
ε_s	Strain at reinforcing steel
ε_{sh}	Strain hardening initiation strain
ε_{su}	Ultimate strain capacity
γ	Hilber-Hughes-Taylor Method coefficient
γ_c	Specific weight of concrete
ξ_i	Critical damping ratio for mode i
λ_c	Confined concrete strength modifier
ω_i	Natural vibration frequency of mode i
$\emptyset$	Diameter of reinforcement
v_c	Poisson's ratio of concrete
ρ_S	Ratio of shear reinforcement
ρ_{sh}	Volumetric confinement ratio
ρ_x	Confinement ratio on X direction
ρ_y	Confinement ratio on Y direction
$\sum X$	Total mass participation ratio on X direction
$\sum Y$	Total mass participation ratio on Y direction
θ	Rotation
Δt	Time interval

1. INTRODUCTION

1.1. General

Fire safety engineering employs fire prevention, passive and active fire extinguishing measures, and egress approaches to enhance the fire protection of the occupants and building content. Passive fire safety is, as the name implies, an inactive mode of fire protection. While being incorporated in the building's structure inherently, it is built to curtail the possible rapid spread of flames, smoke, and hot gases. The primary aim is to serve as a physical barrier to mitigate and suppress the fire so that living beings can evacuate safely, and firefighters secure more time. It also preserves critical structural elements from fire and increases their fire resistance to avoid fire-induced structural collapse mechanisms. According to the Society of Fire Protection Engineers (SFPE), four key components can be used to establish passive fire protection in a structural system:

- *Structural fire protection:* This can be implemented by using fireproof agents such as intumescent paint and coatings, gypsum-based plasters and cementitious components, mineral wool wraps, and fire-retarded external cladding facades to protect structural members, particularly those made of structural steel. Concrete composition is another reliable method for retaining structural integrity against fire.

- *Compartmentation:* Fire spreading can be confined from one compartment to another allowing a safer evacuation by utilizing fire/smoke partitions such as fire-rated walls, floors, and ceilings.

- *Opening protection:* Fire doors and windows are mounted in a fire barrier opening to serve for the opening's fire safety and to enclose the fire within its initial ignition. Fire resistance would not be effective unless the opening is protected.

- *Firestopping materials:* Minor structural modifications and reconstructions may cause a fire barrier to be penetrated. Previous repairs and workmanship defects could

create breaches in fire partitions. If these spaces are not adequately sealed and covered with a suitable firestop device, the fire barriers become less effective in preventing the fire from spreading beyond the area of its source.

Passive fire prevention features are generally favored to active systems since they offer inherent fire resilience without the need for direct human interference in detecting and controlling the fire. Nevertheless, periodic inspection, testing, and maintenance of these systems should be carried out to ensure that required nominal fire resistance is retained for a possible fire outbreak because a minor change to the prescribed specification can lead to the unit performing a much lower fire rating than initially certified. While these nonstructural life safety content can be distorted by poor workmanship and service use, they can be damaged more severely during a seismic action.

1.2. The Impact of Post-Earthquake Fires on the Urban Environment

The energy input that earthquakes impart to a structure is deemed to be dissipated through the inelastic behavior of structural elements and residual stresses or drifts within the structural system. Although the structural stiffness and strength are ensured by the structure's primary load-resisting system, nonstructural components and systems (NCSs) are subjected to the same dynamic domain and more susceptible to irreparable damage when earthquakes hit. In the 2010 Chile Earthquake, about 50% of inspected hospitals were affected due to pipe leakage in the fire sprinkler system [69], which demonstrates that nonstructural damage can severely affect the service of the building. There is a need to keep NCSs intact to maintain the functionality especially in critical facilities; nevertheless, seismic design, and even periodic inspection of them are not explicitly included in the many codes. Provided that the initial investment on NCSs accounts for 70 to 85% of the total construction cost of a typical building [46], the risk for an economic downtime after a major earthquake continues in seismic-prone regions.

Table 1.1. List of the fire following earthquake events until 2014.

Event	Country	Year	Date	Magnitude (Mw)
San Francisco	USA	1906	18-Apr	7.8-8.3
Tokyo	Japan	1923	1-Sep	7.9
Napier (Hawkes Bay)	New Zealand	1931	2-Feb	7.75
Long Beach	USA	1933	10-Mar	6.3
Niigata	Japan	1964	16-Jun	7.5
San Fernando	USA	1971	9-Feb	6.6
Managua	Nicaragua	1972	23-Dec	5.5-6.5
Morgan Hill	USA	1984	24-Apr	6.2
Mexico City	Mexico	1985	19-Sep	8.1
Whitter Narrows	USA	1987	1-Oct	5.7
Loma Prieta	USA	1989	17-Oct	7.1
Hokkido Nansei-Oki	Japan	1993	12-Jul	7.8
Northridge	USA	1994	17-Jan	6.7
Kobe (Hanshin)	Japan	1995	17-Jan	6.9
Marmara	Turkey	1999	17-Aug	7.4
Napa	USA	2000	3-Sep	5.0
Maule	Chile	2010	27-Feb	8.8
Christchurch	New Zealand	2010 and 2011	4-Sep 22-Feb	7.1 and 6.3
Great-East Japan	Japan	2011	11-Mar	9.0
South Napa	USA	2014	24-Aug	6.0

Besides extensive financial losses, other consequences including human fatalities may occur especially in cascading multi-hazard events. Post-earthquake fire (PEF) damage can be worse than that caused by the earthquake itself [63]. Table 1.1 lists the historical fire following earthquake (FFE) events (20 earthquakes from 7 countries) [39]. In the 1906 San Francisco Earthquake, it was estimated that the FFE accounted for 80% of the total damage, irrespective of an earthquake, and more than 3,000 people died [62]. In the 1923 Tokyo Earthquake, FFE resulted in the majority of the 140,000 deaths, and 77% of 575,000 buildings were destroyed by fire [64, 75]. In the 1995 Kobe Earthquake, 500 fatalities, and approximately 7000 destroyed buildings were due to fires alone [26]. Compared to the consequences of fires immediately after an earthquake, if active and passive fire protection systems are not checked regularly for potential damages, the situation with their reduced fire resistance is unlikely to change in fires occurring after a period in earthquake-damaged buildings.

The 1994 Northridge and 1995 Hyogo-Ken Nanbu earthquakes resulted in significant damage to fire-proofing [60, 30, 41, 66] in buildings. In the 1995 Kobe

Earthquake, damages to 40.8% of the sprinkler systems and 30.7% of the fire doors were reported as stated in Table 1.2 [36]. The loss of egress routes as a result of the collapse of precast concrete stair units in at least four multi-story buildings necessitated the evacuation of occupants from windows following the 2011 Christchurch Earthquake [22]. In the Lyttelton aftershock of the 2011 Canterbury Earthquake, approximately 10% of observed PFP systems in moderately damaged buildings were compromised [16].

Table 1.2. Damages to fire protection systems after the 1995 Kobe Earthquake.

Type of fire protection systems	Number of systems surveyed	Number of damaged systems	Percentage (%) of damaged systems
Sprinkler system	544	222	40.8
Indoor fire hydrant	451	107	23.7
Foam extinguishing system	83	20	24.1
Halogenated extinguishing system	162	109	10.5
Automatic fire alarm system	542	71	20.1
Emergency generator unit	444	161	16
Fire doors	524	17	30.7

1.3. Reliance of Fire Protection Systems During and After Earthquakes

Fire extinguishing solutions often rely on active fire protection (e.g., automatic sprinklers) in tall buildings. Besides the detection and suppression mechanism of active systems is perceived to be less reliable than passive fire protection (PFP), the operability of sprinklers is at risk if the storage tank water supplies and electricity supply to pumping systems are lost during seismic excitations. In addition, potential obstructions on the roads and evacuation routes within buildings and multiple callouts may increase the response time of the fire brigade [16]. Considering that many building codes permit a reduction in PFP where sprinklers are installed [17], this represents a serious deficiency in the fire resistance performance of PFP systems such as fire doors and eventually leads to failure in a fire spread if it is already damaged in an earthquake event.

Fire door assemblies must be periodically checked to ensure the following measures: (1) door leaves are aligned with no visible sign of bowing or any other structural faults, (2) door frames are fastened securely to the wall partitions and free of damage, (3) the gaps between the door leaf and the frame must be neither too small to get stuck nor large enough

as to impede effective fire and smoke-sealing (4) heat-activated intumescent fire seals and smoke seals are fitted properly with no damage, (5) hinges, latches, self-closing devices, and automated release mechanisms are all functional. Any fire door sets proven to be defective shall be repaired or replaced.

The annual inspection and maintenance of fire-rated door assemblies are required according to the NFPA 80 [51]. Whereas BS 9999 [9] stipulates every six months for the checks of all fire doors. These time intervals can be rearranged especially for densely populated tall buildings. Besides, there is no specification worldwide regarding the technical investigation of fire doors after an earthquake, there is even still no legislation on periodic fire door inspection in many earthquake-prone countries. To gain a further understanding of this phenomenon, where there is limited research available to make a reliable assessment, this study investigates the seismic and post-seismic fire performance of fire doors, as well as the failure modes and reductions in their FRR when they are subjected to maximum drift demand in case of a design-level earthquake.

1.4. Research Significance

The damage caused by an earthquake to passive fire protection systems is indeed variable, and as a matter of fact, the loss in their fire resistance is likewise unpredictable with the current literature. This research not only helps to fill the gap in the current literature by producing applicable experimental data on the damage states of drift-sensitive nonstructural components in tall buildings under design-level earthquakes and post-earthquake fire performance of fire doors but also make a sufficient impact for repair/replacement criteria of fire doors to be included in the next-generation design codes.

1.5. Objectives and Scope

This research aims to address the concern of a lack of design code/guideline for the likelihood of damage to fire prevention systems, which has the potential to increase the risk of casualties and property loss in the event of a fire outbreak following an earthquake. Specifically, it has been attempted to determine the extent of damages to fire-rated doors in tall buildings under design-level earthquakes, as well as how these damages influence their fire resistance rating performance. The reliability of the remaining fire resistance of fire

doors during post-earthquake fires is difficult to evaluate since their potentially reduced performance levels are not currently quantified in design codes. Although some building regulations stipulate periodic checks to ensure not exceeding permissible clearances for fire doors, no provision regarding the inspections following an earthquake is provided. Provided that there is currently no global design code for fire following an earthquake, the purpose of this study is to demonstrate the necessity for a design code/guideline for the repair and replacement of earthquake-damaged fire protection systems in order to avoid catastrophic scenarios in built environments.

1.6. Thesis Outline

This thesis has seized the opportunity to establish relevance between two major sections: nonlinear design, analyses, and seismic response quantities of a generic tall building, followed by earthquake simulation and subsequent fire rating tests of fire door specimens for fire resistance loss assessment. The outline, on the other hand, is divided into five core chapters that go into further detail. In Chapter 1, background information for the motivation and primary objectives of this research are summarized. Chapter 2 specifically addresses previous studies available in the literature on earthquake or post-earthquake fire performance of passive fire protection partitions and fire doors. Chapter 3 focuses on the accurate determination of the inter-story drift ratio demands under nonlinear time-history analyses at various locations where fire doors can be placed in the floor plan of a generic tall building developed within the framework of performance-based design. In chapter 4, after observing the damage modes on fire door assemblies under seismic drift demands of design-level earthquakes via mechanical testing and assessing their effects on the serviceability of fire doors, post-earthquake fire performance of seismically damaged fire doors, as well as the failure modes and reductions in their fire ratings are analyzed. Ultimately, Chapter 5 provides the study's closing comments as well as recommendations for further experimental and numerical research.

2. BACKGROUND

2.1. Post-Earthquake Fire Research on Individual PFP Systems

Earthquake damage to passive fire protection (PFP) items can create cracks or other openings larger than permissible clearances that can lead to increase ventilation of compartment fires. These openings also allow the migration of smoke and hot gases on the unexposed face, which predominantly causes integrity loss to happen in a short time. Experimenting with PFP systems is essential to quantify accurately their earthquake performance and remaining fire resistance for a potential post-earthquake fire event.

Sekizawa et al. [65] developed a simplified model for seismic-induced fire risk assessment for the probability of failure of both active and passive fire protection systems. The implemented approach considers building size and type, mounted fire safety systems, fire service reaction, and input ground motion intensity. Even in regular operation, there is a likelihood that fire prevention systems may fail due to maintenance faults. They used the current Japanese recommendations [35] that suggested an effective 50% reduction in fire resistance for partitions subjected to 0.33% transient drift. It was concluded that in case of any component of a fire sprinkler system is not functioning as intended, the system as a whole cannot operate properly, which increases the role of PFP systems.

Porter et al. [58] proposed a new approach called assembly-based vulnerability for determining the seismic fragility of specific buildings. A cycle was used to simulate shaking, response, damage, repair, and loss. The technique is repeated for various ground motion intensities that the structure may experience until generating a complete seismic vulnerability function. After gathering the seismic damage statistics, they stated that visible damage can be observed at a drift ratio of 0.4% where smoke distribution is expected through gaps and cracks by dislodged stopping plaster, and fire spread can occur at a drift ratio of 0.85% when the drywall partition is likely to separate from the framing.

Sharp and Buchanan’s [67, 68] findings from the previous experiments [20] on timber-framed walls subjected to lateral seismic loading reported that the damage sustained

by the wall system became substantial at a drift level of 0.6%, which can allow the fire cell to be compromised. Further cycling up to drift ratios of 1.3% may cause the wall to lose much of its fire resistance. Damage to partitions may block passengers' safe egress by obstructing doors, degrading their fire resistance, or preventing them from functioning as expected in a fire or smoke alarm.

Taylor [70] addresses insufficiently fire-protected penetrations for building services and the incidence of flawed fire and smoke doors as the prominent concerns about the reliable performance of passive fire protection. Although the sprinkler system is the most effective tool for controlling fires in tall buildings, smoke control and pressurization are typically dependent on an external power source. Therefore, adequate passive fire protection should be provided while they are constructed to accommodate seismic forces without sustaining damage to maintain fire and smoke prevention.

Collier [15, 16] tested five timber-framed and two steel-framed walls (one contains a fire door) under a cyclic loading history designated to simulate a sequence of earthquake demands ranging from 1 to 2.5% drift ratio to observe a variety of damages for subsequent fire testing. Flaming from gaps caused by detachment of the wall linings, notably around the perimeter of the specimens, and cracks on corners and joints were identified as the primary causes of the reductions in fire rating. Most of the decrements in FRR occurred within a range of 30% to 70% of the control test's fire resistance. The FRR of a 60-minute-rated plasterboard lined wall can be reduced by up to 50% under a design-level earthquake. The first mode of failure for almost all the specimens was Integrity (E). It was concluded that after a drift ratio of 1% in the racking phase, the fire resistance (Integrity) rapidly declines. For the specimen included a fire door, clearances between the door leaf and its frame were measured at the end of each cycle of the racking test, 0% drift ratio position following the racking test, and just before the fire rating test. A maximum of 1.25% (40mm) is achieved during the racking test. Following the wall's Integrity failure at 36 minutes, the 60-minute-rated fire door failed Integrity at 51 minutes (15% reduction) due to flaming at the top of the door leaf, while no Insulation failure occurred for the fire door assembly.

Hoehler et al. [33] carried out a comprehensive test program to study the mechanical performance of a broad range of passive fire-proofing items by applying the FEMA 461 [28]

loading protocol as well as their functionality in succeeding fire tests. They revealed that various PFP systems have different capacities to allow deformation while retaining their smoke and fire ratings.

2.2. Post-Earthquake Fire Research on Full-Scale Buildings

A five-story reinforced concrete building outfitted with various nonstructural components and systems (NCSs) was subjected to 13-ground motion tests with increasing intensity, seven with base isolation (BI) and six with a fixed base (FB) arrangement, on a large high-performance outdoor shake table (LHPOST) at the University of California, San Diego (UCSD) [45]. The building was conceptually designed to resist up to 2.5% IDR. The largest motion, where the peak IDR reached up to 6% in FB configuration, caused interior doors to either completely open or close because the door latches and door frames were severely distorted.

Table 2.1. Pre-fire earthquake test sequence and seismic response quantities.

Test Name	Seed Earthquake Ground Motion	PIDR (%)
FB-1: CNP100	Canoga Park - 1994 Northridge Earthquake (Service level)	0.47
FB-2: LAC100	LA City Terrace- 1994 Northridge Earthquake (Service level)	0.56
FB-3: ICA50	ICA - 2007 Npisco (Peru) Earthquake (50% scale)	0.94
FB-4: ICA100	ICA - 2007 Npisco (Peru) Earthquake (100% scale)	1.41
FB-5: DEN67	TAPS Pump Station 9 - 2002 Denali Earthquake 67% scale (Design level)	2.75
FB-6: DEN100	TAPS Pump Station 9 - 2002 Denali Earthquake 100% scale (MCE level)	5.99

Compartment ventilation parameters can affect the rate of heat release (HRR), total heat released, flame length, the generation of hot spots, the direction of flame/smoke propagation, etc. The compartment's airtightness was determined by comparing the external and internal pressure imbalances (gross leakage area) after each base-isolated and fixed-based shake test.

A blower door fan was employed to provide an indicator of the entire leakage area on the 3rd floor. The fan was placed into the bottom of the interim door opening, and a manometer was installed to the right of the door frame to read fan flow and compartment pressure. The data was then utilized to compute the average effective leakage area per test. The findings suggest that the latter two experiments led to a substantial leakage area, which possibly influences fire growth and smoke distribution.

Following the largest motion test, the 3rd floor was then exposed to fires (500 kW to 2000 kW), and it was highlighted that the loss of compartmentation due to ground motions caused smoke and fire spread and increased ventilation openings rendered the means of egress ineffective. Specifically, dislodged gypsum wallboard from walls, holes formed at joint locations, and damage to fire door assemblies impaired compartment barrier components. The main concern is that loss of compartment integrity prevents passengers when attempting to escape and makes it challenging for the fire brigade to carry out rescue and firefighting operations in a potential fire spread.

Another post-earthquake fire testing was performed for a full-scale six-story cold-formed steel wall braced building on the LHPOST [77]. The building was subjected to seven earthquake motions scaled to apply service, design, and maximum considered earthquake (MCE) demands, and the physical damages on fire-rated and non-fire-rated doors were recorded and classified. The subsequent live-fire tests were conducted after service (EQ1) and MCE (EQ7) levels shaking, at two selected floors in which four fire-rated doors were installed. During pre-fire EQ7 simulation, the peak IDR was recorded as 1.70%. Following the fire test, all four doors on level 2 and three doors on level 6 were inoperable. A rich set of data including door damage states and the associated damage modes has emerged from these tests.

Table 2.2. Seismic tests procedure and obtained response quantities.

Test Name	Seed Earthquake Ground Motion	PIDR (%)
EQ1: RIO-25	Rio Dell Overpass – 1992 Cape Mendocino (Service level)	0.08
EQ2: CNP-25	Canoga Park – 1994 Northridge (Service level)	0.09
EQ3: CUR-25	Curico – 2010 Maule, Chile (Service level)	0.10
EQ4: CUR-25	Canoga Park – 1994 Northridge (Service level)	0.10
EQ5: CNP-50	Canoga Park – 1994 Northridge (50% Design level)	0.24
EQ6: CNP-100	Canoga Park – 1994 Northridge (Design level)	0.89
EQ7: CNP-150	Canoga Park – 1994 Northridge (MCE level)	1.70

Provided that the drift demands remained extremely low (PIDR < 0.1%) during the service level testing (EQ1-EQ3), all the doors operated successfully with no visual damage. The damage began on four corridor doors during design level motion (PIDR ~ 1.0%), albeit the observed damage remained relatively modest (e.g., door frame screw popping and corner gapping). The damage was sustained and became significant during the MCE level motion EQ7 (PIDR > 1.5%).

Table 2.3. Door damage states and the associated damage modes.

Damage State	Physical Damage
Minor (DS-1)	Door frame gapping, door frame screw withdrawal, door frame loosening
Moderate (DS-2)	Door jam, door frame distortion, door latch failure
Severe (DS-3)	Door frame severe distortion, door frame detachment

2.3. Seismic Performance of Door Systems

The literature specifically addressing the post-earthquake serviceability of fire-rated or non-fire-rated doors is limited. Aoki [2] stated that residential doors are obstructed due to lateral deformations of structural members under seismic activity. The primary factor is that the gap between the door leaf and its frame is relatively small to dissipate the large deflections induced by an earthquake. His findings enabled the development of an underlying trigonometric relation (2.1) for determining the drift ratio level where door leaf can jam within the door frame as follows:

$$\frac{\Delta}{H} = \frac{\delta}{h} \approx \frac{a}{w} \approx \frac{b}{w} \tag{2.1}$$

where Δ is the relative story displacement (drift), H is the story height, δ is the lateral deformation of the door frame, h is the door frame height, a is the gap between door leaf and frame at the top, w is the width of the door frame, and b is the gap between door leaf and frame at the bottom.

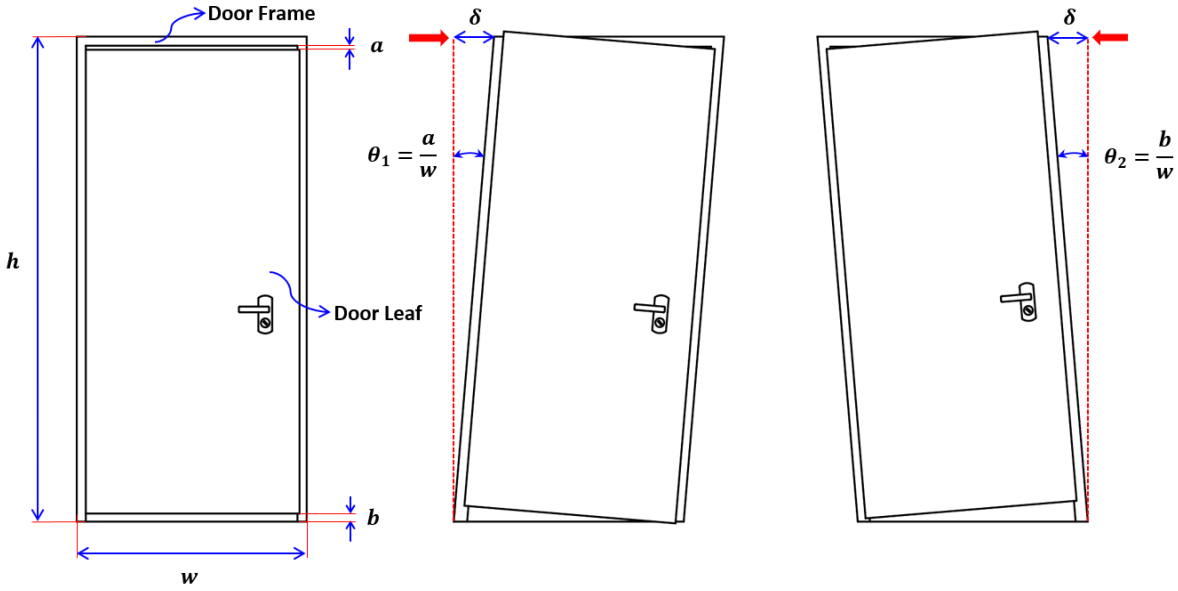

Figure 2.1. In-plane deformation concept for door systems under lateral loadings.

Forcael et al. [31] conducted quasi-static cyclic tests on a full-scale prototype of a reinforced concrete frame including a timber residential door (700x2400 mm) by adopting recommendations in FEMA 356 [27] and FEMA 461 [28] loading protocols to investigate and evaluate the effects of varying seismic drift demands on the operability of residential doors. They recorded that for an inter-story drift ratio (IDR) of 0.6%, a residential door can get obstructed while exhibiting disturbances resulting from excessive spacing, out-of-plane deformations, distortions at the door lock level, and flattening of the door frame.

Chang et al. [11] tested four (D1-D4) single-leaf (900x2100 mm) and two (D5-D6) double-leaf (1370x2100 mm) steel exist doors that could be installed in a high-rise residential building in Taiwan. They observed that doors operate smoothly if the IDR is less

than the critical value of 0.5%. As IDR reaches 0.7%, the door lock can get stuck. When IDR is greater than 1.1%, even the door frame can be severely distorted.

Table 2.4. IDRs recorded in associated damage modes.

Door Label	**Damage Modes**					
	Door Lock Slight Damage	*Door Lock Severe Damage*	*Door Latch Slight Damage*	*Door Latch Severe Damage*	*Slight Collision of Door Assembly*	*Severe Collision of Door Assembly*
D1	0.4	0.5	0.6	0.7	1.7	N/A
D2	0.4	0.5	0.9	1.5	0.9	1
D3	0.6	0.8	0.9	1	1.1	N/A
D4	0.5	0.6	N/A	0.8	0.6	0.8
D5	N/A	0.3	N/A	0.5	0.6	1.7
D6	N/A	0.1	0.3	0.4	0.4	1

They further remarked that the severely deteriorated door lock was the initial mode of damage that impeded the door from opening smoothly after the simulated seismic loading in each sample. Thus, the exit doors should remain unlocked during an earthquake for emergency safety purposes. When the IDR exceeded 1.0%, both the door lock and the door catch suffered substantial damage.

Chen et al. [12] investigated a 6-story L-type reinforced concrete hotel in two separated units connected with a seismic expansion joint in Taiwan that remained in a damaged state following the 1999 Chi-Chi Earthquake (Mw=7.6). They surveyed and measured the exit doors in detail, compared the material, construction, and location of damaged and undamaged doors, and assessed the causes of damages and affecting parameters. They listed the expected damage scenarios and their recurrence ratios as stated in Table 2.5.

Table 2.5. Identified damage types induced on surveyed exit doors.

Damage mode #	Description of the damage mode	Recurrence (%)
1	The door leaf exceeded the doorsill or upper frame	73%
2	The side frame was bent by infill wall	40%
3	The upper frame was bent under compression of infills	14%
4	The side/upper frame was deformed by infill wall	27%
5	The frame components were separated	0%
6	The lock-strike caved in the locking bent and got stuck	27%
7	The axis of the hinge was pulled off	2%

After surveying 17 steel and 205 wooden doors, they simply re-categorized them into three types; doors that can be opened smoothly, (2) doors that can be opened only with difficulty, and (3) doors that cannot be opened at all. According to the recordings, 41% were unable to be opened, 28% opened hardly, and just 31% opened smoothly. They also revealed that steel doors outperformed wooden doors in terms of seismic resistance.

3. CASE STUDY

3.1. Building Properties

A generic tall residential building consisting of 35-story above and 5-story below the ground level was designed and investigated in this study. The tower has a load-bearing system in which seismic loads are resisted by moment-resisting frames and uncoupled or coupled structural walls. The base of the tower was assumed to be set into a slightly raised landscaped podium, which creates space for parking garages beneath the building. The basement floors were confined on all sides by perimeter walls. The structural layout and the geometry of the floor plan are presented in Figure 3.1.

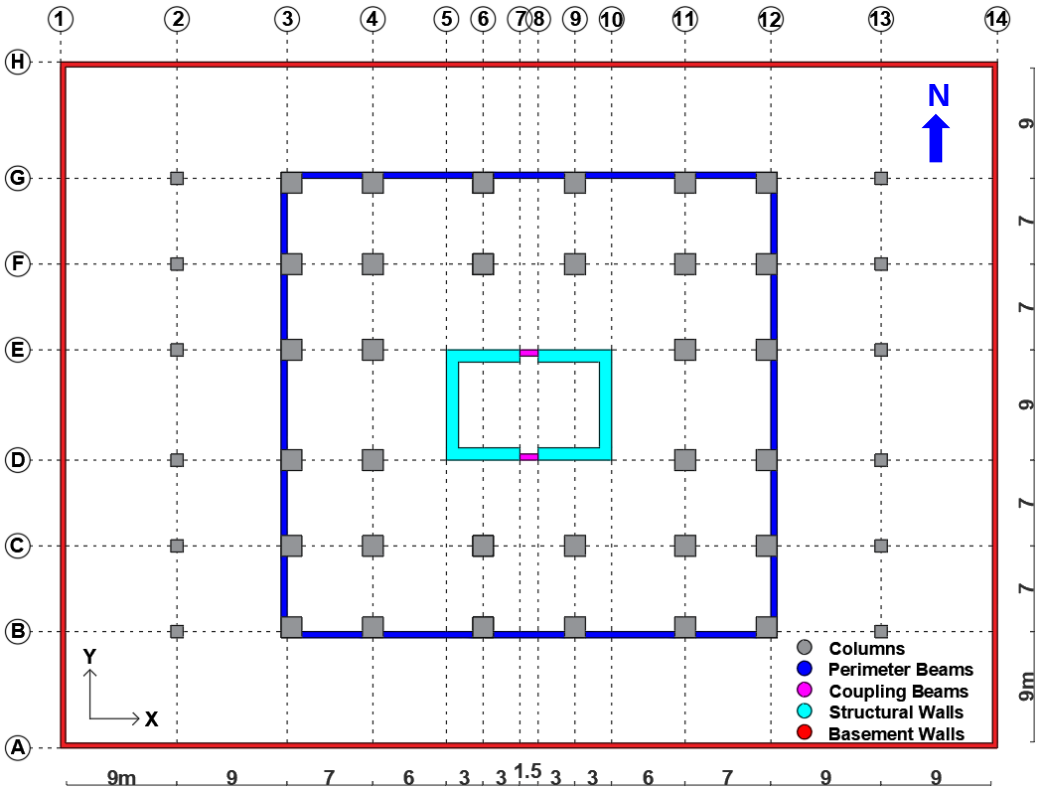

Figure 3.1. The structural layout of the tall residential building.

Each tower floor was assumed to have an identical structural plan, except the dimensions of the structural members were reduced group by group at every seven floors as the building height increases. The height of the basement floors is 3.10 m, whereas the tower floors have 3.30 m in height. The total height of the structure is 134.00 m, and the clear

height of the tower is 118.50 m. While the basement floors cover a surface area of almost 4153 m^2, the tower floors have a nearly 1425 m^2 area.

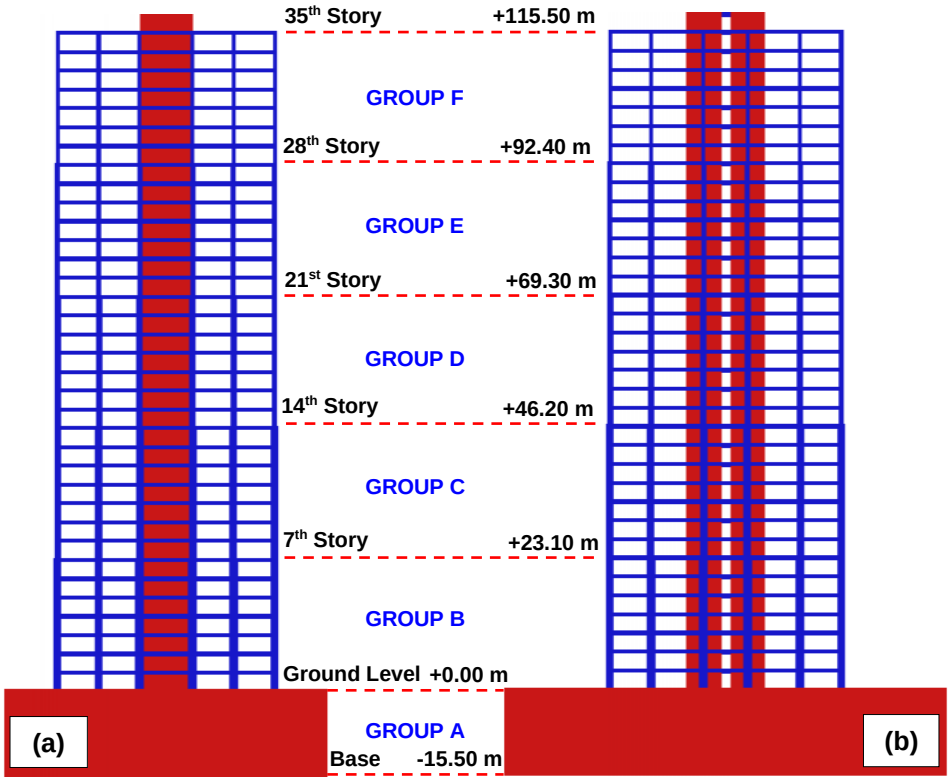

Figure 3.2. The 2D view of the building model in (a) YZ plane, and (b) XZ plane.

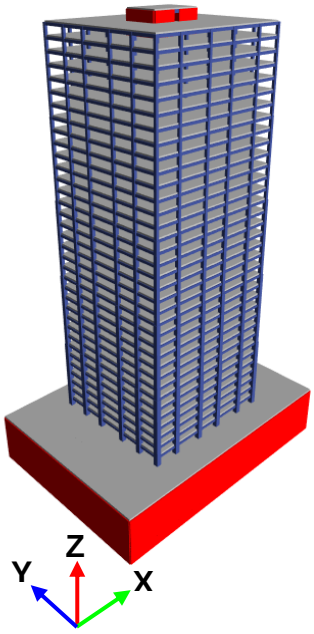

Figure 3.3. The 3D illustration of the building model generated in CSI ETABS [25].

3.2. Seismic Design Parameters

The target performance levels (e.g., O, LS, CP) in the TBSC [74] are provided in accordance with the seismic hazard levels which are defined based on seismic wave behavior as it travels through the soil medium, regional, and site-specific geology/geotechnical factors, and previous earthquakes.

Table 3.1. Probabilistic quantities of earthquake hazard levels used in this study [74].

Probability of Exceedance in 50-Year	**Mean Recurrence Interval**	**Earthquake Hazard Level**
2%	2475 Years	DD-1 (Maximum Considered Earthquake)
10%	475 Years	DD-2 (Standard Design Earthquake)
68%	43 Years	DD-4 (Service Earthquake)

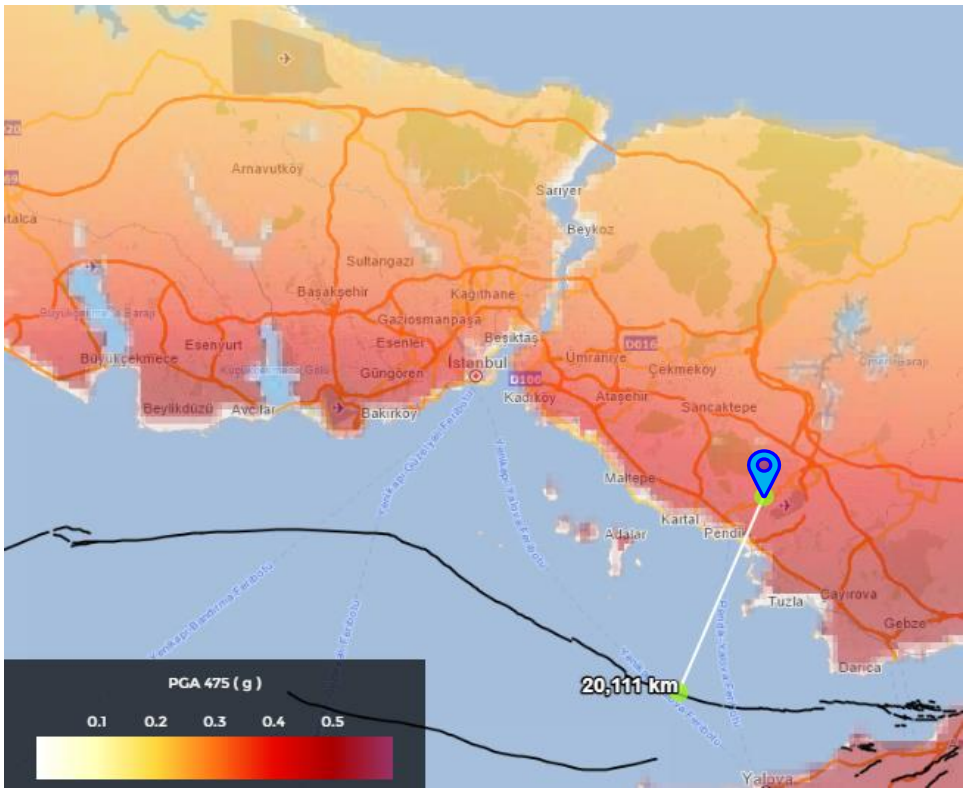

Figure 3.4. The Joyner-Boore distance (20.111 km) between the location of the case study building and the closest active fault line.

The building occupancy category and building importance factor for the issued tall building were classified as $BOC = 3.0$ (residential facility) and $I = 1.0$, respectively [74].

Spectral acceleration coefficients (Table 3.2.) at the site coordinates (40.905627 N, 29.281342 E) required to define the elastic design spectrum were obtained from the earthquake hazard map [73] provided by the Disasters and Emergency Management Agency in Turkey. The hypothetical local site's soil type was assumed to correspond to a Site Class ZC (very dense soil/soft rock) condition [74].

Table 3.2. Spectral and design acceleration coefficients corresponding to ground motion intensity levels used in this study.

Ground Motion Intensity Level	**S_S**	**S_1**	**S_{DS}**	**S_{D1}**	**PGA (g)**
DD-1	1.731	0.499	2.077	0.748	0.693
DD-2	0.987	0.277	1.184	0.416	0.405
DD-4	0.270	0.071	0.351	0.106	0.117

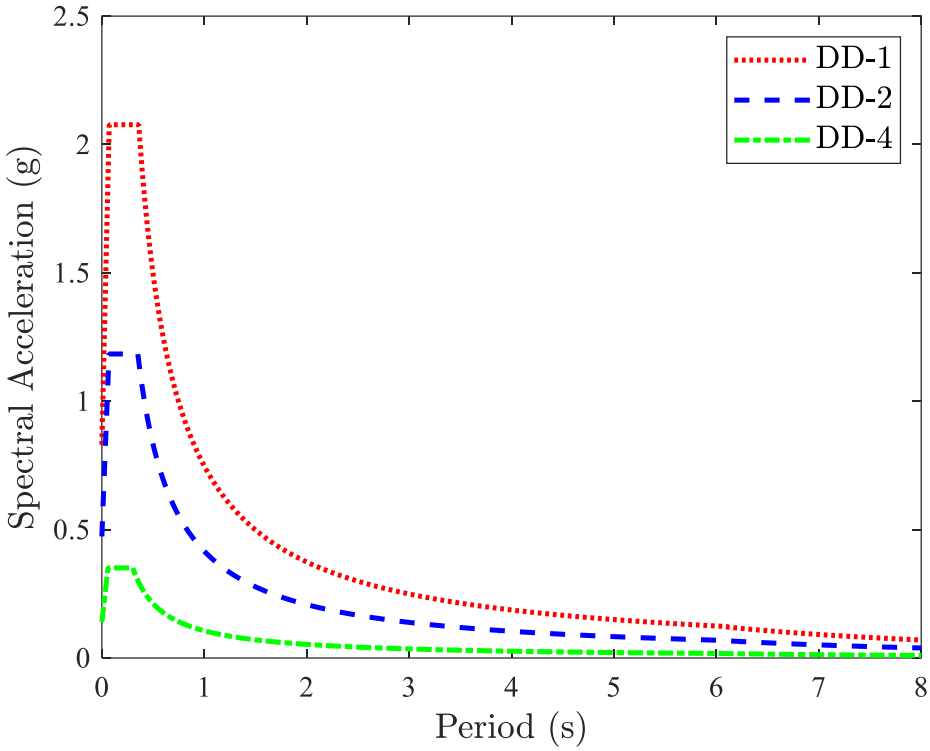

Figure 3.5. Horizontal Elastic Design Spectra with 5% damping.

3.3. Design Stages

A tall building structural system is proportioned and reinforced following the capacity design principles, where linear-elastic analysis is often used for preliminary design to determine required strength corresponding to the yielding actions [5] Since we take advantage of the concept of ductility regarding the inelastic energy dissipation of materials, a structural behavior coefficient R is determined to reduce the seismic loads in the initial design. Beyond the conventional/prescriptive seismic design, the building's actual/accurate behavior is then attempted to be represented by explicitly modeling and assessing post-yield ductility, energy dissipation, deformation, and strength capacity of elastic and inelastic components in nonlinear dynamic analyses with real earthquake records [57].

The term *performance* commonly refers to a building's condition after a natural disaster, and it indicates the limiting of damage level expected to be satisfactory. In the design of structural systems, our primary objective is to secure human life, preserve building content, and retaining the service of the building. Performance levels are set to achieve safety, reparability, and serviceability design objectives. Performance levels for a structure can vary on demand regarding the reasonable balance between construction cost and the risk of damage.

Under the design-level ground motion intensity, with the short-period design spectral acceleration coefficient of $S_{DS} = 1.184$ and building occupancy category of $BOC = 3$, the building was assigned a seismic design category of $SDC = 1$. Since the height of the tower from the base is $HN = 118.5\,m$, the building height category of the structure was determined as $BHC = 1$. The building resists the seismic loads by reinforced concrete coupled and uncoupled highly ductile structural walls in the X and Y directions, respectively, with a combination of reinforced concrete highly ductile moment-resisting frames in both directions. Therefore, the structural system behavior factors in the X direction as $R_X = 8$ and the Y direction as $R_Y = 7$ were employed in the design. The overstrength factor for both directions was taken as $D = 2.5$. TBSC [74] applies a three-stage design procedure for this type of building:

- *Design Stage 1 (Preliminary/conceptual design):*

The structure was designed following the strength-based approach under the linear combination of gravity loads with lateral loads such as wind, soil pressure, or reduced earthquake demands of a 5% damped elastic design spectrum for design-level ground motion intensity (DD-2). Life Safety performance was sought to be achieved, referring to major structural and severe nonstructural component damage without any loss of life. Internal stresses were amplified by the overstrength factor when members are designed to resist brittle behavior (e.g., shear forces, diaphragm in-plane forces, punching shear stresses). A seismic accidental eccentricity as 5% of the perpendicular plan size to the loading direction must be included in the analyses to consider the inaccuracy in estimating the mass and stiffness centers. Structural irregularities including torsional irregularity (A1), diaphragm discontinuity (A2), projections in plan (A3), weak-story (B1), soft-story (B2), discontinuity of vertical structural members (B3) were all checked and satisfied. The coefficients regard to second-order effects were computed for each floor and compared with the given limits in the code. When the modal superposition method was performed, reduced earthquake forces were magnified for both loading directions by employing the base shear value from equivalent static earthquake load analysis. Under updated internal forces, demand/capacity ratios shall satisfy the criteria for the strength of structural members, whereas inter-story drifts shall fulfill the serviceability requirements.

- *Design Stage 2 (Serviceability evaluation):*

This assessment step demands structural members to respond simply elastic (or practically elastic with minor nonlinear deformation) under the presence of service level seismic intensity (DD-4). Operational performance level was intended to be satisfied, referencing negligible damage to nonessential services. Structural members' capacities shall be computed by sectional analysis of the cross-sections considering expected material strengths rather than design quantities. Higher stiffness modifiers must be utilized for reinforced concrete structural members to accommodate the anticipated lower level of damage. Therefore, in the calculation of internal forces, $R/I = 1$ and $D = 1$ were used for the seismic load reduction factor.

The site-specific design spectrum for the service level ground motion intensity was generated with a 2.5% damping ratio, while spectral accelerations defined for 5% damping are multiplied by 1.25. An additional 5% accidental eccentricity is not required to be included in the analyses. The minimum base shear criterion, as applied in the preliminary design, was not employed. Demand/capacity ratios for internal forces in ductile structural components must not exceed 1.5, whereas they must not surpass 0.7 for non-ductile structural components.

- *Design Stage 3 (Collapse level evaluation/design improvement):*

The performance of the tall building was assessed under the DD-1 level earthquakes with the aim of delivering the probability of partial or complete collapse to a reasonable minimum. It refers to an allowable degree of damage in structural members regarding ductile response quantities while all other brittle response quantities remain in the elastic range. Considering inherent variability in material strength and strain hardening, the probable peak strength of structural elements corresponds to expected (mean) strength values, enabling actual structural performance capabilities to be evaluated. For nonlinear modeling, all structural components or element groups' force-deformation relationships were manually defined. The damping ratio was set as 2.5% for the modes considered for the generation of 2.4% modal damping and 0.1% Rayleigh proportional damping for higher mode shapes [59]. Nonlinear time-history analyses were then carried out under compatible 11-pair of ground motions that were selected concerning the site-specific benchmarks (e.g., moment magnitude, rupture distance, shear wave velocity of the soil medium, and fault type) and scaled on the 5% damped elastic design spectrum for MCE level ground motion intensity since ground motion prediction relations are commonly formulated for 5% viscous damping ratio [2]. Deformation and strength demands were determined for displacement-controlled (nonlinear inelastic behavior) and force-controlled (linear elastic behavior) response parameters, respectively, and compared with the performance limits. Eventually, the design was revised to satisfy the targeted performance level.

Table 3.3. Performance objectives and evaluation/design approaches

Ground Motion Level	Normal Performance	Assessment/Design Methodology
DD-2	Life Safety	Strength-Based Design
DD-4	Operational	Strength-Based Design
DD-1	Collapse Prevention	Deformation-Based Design

3.4. Linear Modelling and Analysis

The strength-based analysis is a static-linear procedure employed to verify strength, stiffness, stability, and serviceability characteristics of a structural system to withstand reduced seismic loads by utilizing code-prescribed behavior factors depending on the categorized inherent ductility supply of a building type. While we adopt the same reduction factor for all cross-sections in modeling to account for their inelastic energy dissipation under equivalent static forces when solving complex structural systems, we follow a modeling procedure where structural elements remain linear elastic through the analysis phase, which is computationally efficient. Assuming this constitutive model, strains in defined materials are too small/negligible, stress is proportional to strain, the material returns to its original state when the loads are removed, the unloading path is identical to the loading path, and the loading rate does not influence the material behavior [38]. Permanent deformations such as cracking, yielding, or crushing are not recognized in this approach. Therefore, this method is likely to produce approximate, unsafe, or over-conservative results from one structural element to another, particularly in tall buildings. Nevertheless, for conceptual design and initial optimization close to the final design under gravity and lateral loads, strength-based design is a useful tool. The seismic codes' reinforcement detailing criteria shall be followed to ensure that the structural members contain sufficient ductile capability. Modal analysis is performed to check the appropriateness of the building model’s dynamic properties.

For the strength-based design of the structure, the linear-elastic model of the generic building (mechanical characteristics of materials, initial dimensions of the structural elements, predetermined geometry, etc.) was generated in CSI ETABS software [25]. Frame objects were used to model beam-column formulation as straight lines connecting two nodes

and accounting for axial load, biaxial bending, torsion, and biaxial shear [7]. Shell objects accommodating membrane (only in-plane stiffness) and plate-bending (flexural stiffness) behavior were used to model slabs and structural walls [18]. The damping properties (e.g., viscous damping) and effective rigidities for structural members given in Table 3.4 were applied based on TBSC [74].

Table 3.4. Effective stiffness modifiers that enable reinforced concrete structural elements to be regarded as cracked sections.

Structural Members	**Design Stages**			
	I	**II**	**I**	**II**
Walls - Slab (In-Plane)	**Axial**		**Shear**	
Structural Walls	0.50	0.75	0.50	1.00
Basement Walls	0.80	1.00	0.50	1.00
Slabs	0.25	0.50	0.25	0.80
Walls - Slab (Out of Plane)	**Bending**		**Shear**	
Structural Walls	0.25	1.00	1.00	1.00
Basement Walls	0.50	1.00	1.00	1.00
Slabs	0.25	0.50	1.00	1.00
Frame Elements	**Bending**		**Shear**	
Coupling Beams	0.15	0.30	1.00	1.00
Moment Frame Beams	0.35	0.70	1.00	1.00
Moment Frame Columns	0.70	0.90	1.00	1.00
Structural Walls (Equivalent frame)	0.50	0.80	0.50	1.00

3.4.1. Material Properties

In the design, C50 concrete class with characteristic compressive strength of $f_{ck} = 50$ MPa was used. The specific weight of concrete was assumed as $\gamma_c = 25\ \mathrm{kN/m^3}$ for dead load calculations. The modulus of elasticity of concrete as $E_c = 37000$ MPa, and the shear modulus of concrete as $G_c = 15417$ MPa, while utilizing Poisson's ratio of concrete as $v_c = 0.2$, were computed by employing the following equations:

$$E_c = 3250\sqrt{f_{ck}} + 14000 \tag{3.1}$$

$$G_c = \frac{E_c}{2(1+v_c)}. \tag{3.2}$$

For reinforcement detailing, B420C reinforcing steel grade with a yield strength of $f_{yk} = 420$ MPa and elastic modulus of $E_c = 200000$ MPa was used. In Design Stage 2, rather than nominal values, the expected properties of materials for structural components, $f_{ce} = 1.3f_{ck} = 65$ MPa and $f_{ye} = 1.2f_{yk} = 504$ MPa, were employed in section analysis to evaluate the building's performance.

3.4.2. Mass Source

For the assessment of the building's dynamic characteristics, the mass source was defined as the combination of dead loads (permanent) and factored live loads (temporary) by utilizing the prescribed values in TS498 [71]. Dead load magnitudes that relied on the volume and material density of structural members were computed and concentrated at the joints intrinsically by the software [25]. In contrast, superimposed dead load (architectural, mechanical, electrical, and plumbing contents) and live load magnitudes were determined considering the functioning of the facility since they might vary from one occupancy type (residential, offices, shops, etc.) to another. They were then uniformly distributed to the slab elements manually. The magnitudes of gravity loads are summarized in Table 3.5.

Table 3.5. Magnitudes of uniformly distributed gravity loads.

Superimposed Dead Loads (kN/m^2)		**Live Loads (kN/m^2)**	
Ceiling plaster + Floor finishing + Installments	2.0	Residential floors	2.0
		Basement floors	5.0
Infill/partition walls	1.0	Landscape (Ground floor)	3.5
		Snow (Ground/top floors)	1.0

The seismic mass source must first be established for both static and dynamic analyses to determine the internal forces and simulate the response. The weight of the structure employed in the computation of seismic loads is dependent on the stated mass

source. For computational efficiency and solution accuracy, calculated loads are transferred equally to the three translational degrees-of-freedom (DOF) of joints as uncoupled lumped (distributed) masses without producing mass moments of inertia for the three rotational DOF [18]. The mass is calculated using a linear combination of gravitational load patterns multiplied by code-specified scaling factors. Since it is improbable that a structural system would constantly sustain the anticipated maximum live load, live loads are decreased with participation factors defined by stochastic techniques. The underlying notion suggests that once the loading area becomes large, the likelihood of the whole region being completely occupied in a single occurrence reduces. While dead loads were not scaled with any factor, the contribution factor of $n = 0.3$ for all live loads was applied as consistent with TBSC [74]. Seismic mass at each j node was computed by utilizing Equations (3.3) and (3.4) by the software [25] as:

$$w_j^{(s)} = w_{G,j}^{(s)} + n w_{Q,j}^{(s)} \tag{3.3}$$

$$m_j^{(s)} = \frac{w_j^{(s)}}{g}. \tag{3.4}$$

3.4.3. Load Combinations

A load combination superimposes the linear analysis outputs, including displacements and forces at joints, as well as internal member forces and stresses under specific load cases [18]. In line with the TS500 [72] and TBSC [74], the structural components must be constructed such that their design strength is equal or greater than the demands of the factored loads in the following combinations:

$$1.4G + 1.6Q \tag{3.5}$$

$$1.0G + 1.3Q + 1.3W \tag{3.6}$$

$$0.9G + 1.6W \tag{3.7}$$

$$1.0G + 1.0Q + 1.0E_e^{(H)} \tag{3.8}$$

$$0.9G + 1.0E_e^{(H)} \tag{3.9}$$

$$1.4G + 1.6Q + 1.6H \tag{3.10}$$

$$0.9G + 1.6H \tag{3.11}$$

$$G + Q + 0.2S + E_e^{(H)} + 0.3E_e^{(V)} \tag{3.12}$$

$$0.9G + H + E_e^{(H)} - 0.3E_e^{(V)} \tag{3.13}$$

$$E_e^{(H)} = \pm E_e^{(X)} \pm 0.3E_e^{(Y)} and \pm 0.3E_e^{(X)} \pm E_e^{(Y)} \tag{3.14}$$

where G is the dead load, Q is the live load, W is the wind load, $E_e^{(H)}$is the horizontal component of the earthquake load, $E_e^{(V)}$is the vertical component of the earthquake load, H is the lateral soil pressure and S is the snow load.

The vertical component of the ground motion was included in analyses with a simplified approach as:

$$E_e^{(V)} = \frac{2}{3} S_{DS} G \tag{3.15}$$

where S_{DS} is the short period design spectral acceleration and G is the dead weight of the building.

3.4.4. Modeling Techniques and Assumptions

1. The fundamental idea of meshing is to discretize a domain into finite pieces, each piece representing an element, and to calculate the stresses for each element to combine them for the global structural response. The larger the density of meshing, the greater the accuracy in convergence for response quantities. However, it is computationally efficient to subdivide the components for optimum configuration of topological requirements in performing a proper simulation where uniformity and continuity between nodes are considered. Since the shell objects had easily recognizable regular shapes, they were decomposed

into 4-node square grids no larger than a mesh size of 1.00 m for the analytical model.

2. PEER/ATC 72-1 [54] proposes the semi-rigid diaphragm flexibility as the most realistic model for slabs (e.g., backstay effects in the transfer floor) in the analytical modeling having a finite diaphragm stiffness calculated based on diaphragm thickness, dimensions, and material properties. The diaphragms are assumed as semi-rigid in modeling.

3. Even though frame elements were modeled as line elements connected at joints, the actual cross-sectional dimensions of the columns are large, and the length of the overlap is a vast fraction of the total length of the beams. A rigid-zone factor of 0.5 was applied for frame elements assuming 50% of the actual end offset rigid for bending and shear deformation, while it did not influence axial and torsional deformation [18].

4. An accidental eccentricity of 5% as a typical strategy was applied to the diaphragms to account for any unexpected source (e.g., geometric and material uncertainty, torsional ground motion) incorporating the torsional behavior [6].

5. The simulation did not explicitly account for the stiffness, plasticity, and damping characteristics of the soil medium kinematically interacting with the superstructure through the foundation, which would prolong the building's natural vibration period and shift the seismic demands [78]. As is customary, rigid base boundary conditions (fixed supports) were assigned in modeling, particularly assuming the foundation system extends to bedrock.

6. The magnitude of damping influences not only the peak values of several critical response indicators (e.g., peak inter-story drift) but also the time of the response and, as a result, the hysteretic behavior of structural and non-structural components under seismic excitations [47].

3.4.5. Modal Analysis

Eigenvalue analyses were conducted to determine natural vibration periods and associated modal mass participation ratios of the structure while taking account of different material properties and effective stiffness modifiers in Design Stages 1 and 2. To satisfy the total mass participating of 95% in both X and Y directions as specified in TBSC [74], the first 90 modes of the structure were considered in the analyses, including all modes contributing greater than 3%. Since the structural plan of the building model is symmetric, an unbalanced distribution of mass and stiffness, which likely to cause torsional irregularity in the dynamic behavior of the building, was not observed. The outputs are summarized in Table 3.6.

Table 3.6. Natural periods and corresponding mass participation ratios for Design Stages 1 and 2.

Mode #	Period (s)		Effective Modal Mass (%)					
	DS-I	DS-II	X (Translation)		Y (Translation)		Z (Rotation)	
			DS-I	DS-II	DS-I	DS-II	DS-I	DS-II
1	4.639	3.509	0.000	0.000	48.010	47.590	0.000	0.000
2	4.098	3.112	48.630	48.120	0.000	0.000	0.000	0.000
3	2.948	2.207	0.000	0.000	0.000	0.000	32.050	32.010
4	1.094	0.837	0.000	0.000	14.420	14.090	0.000	0.000
5	1.076	0.817	13.060	12.880	0.000	0.000	0.000	0.000
6	0.982	0.735	0.000	0.000	0.000	0.000	5.290	5.200
7	0.549	0.407	0.000	0.000	0.000	0.000	2.300	2.260
8	0.516	0.389	5.240	5.020	0.000	0.000	0.000	0.000
9	0.479	0.36	0.000	0.000	7.160	6.920	0.000	0.000
10	0.372	0.272	0.000	0.000	0.000	0.000	1.330	1.310
.	.	.	.	.	.	.	.	.
.	.	.	.	.	.	.	.	.
.	.	.	.	.	.	.	.	.
88	0.059	0.042	0.000	0.001	0.000	0.000	0.000	0.000
89	0.059	0.042	0.000	0.000	0.000	0.000	0.000	0.000
90	0.059	0.042	0.000	0.000	0.003	0.000	0.000	0.000
Σ			95.050	95.360	96.350	96.320	88.950	90.310

3.4.6. Dimensions of Structural Members

For the cross-sectional dimensions and reinforcement detailing of the structural members, the code provisions together with the calculation procedures were applied in

Design Stages 1 and 2. For the nonlinear time-history analyses of the building model in Design Stage 3, labeling the structural members for a specified story range is a useful technique to reduce the computational effort and time. The structural members standardized as element groups per 7-story (only the basement has 5-story), considering the change in stiffness between consecutive groups as the height of the structure increases, are given in Figure 3.6. The preliminary dimensions for structural members optimized to use in the forthcoming design phase are summarized in Table 3.7. After conducting the performance-based analysis of the building, these dimensions are reviewed and may be updated.

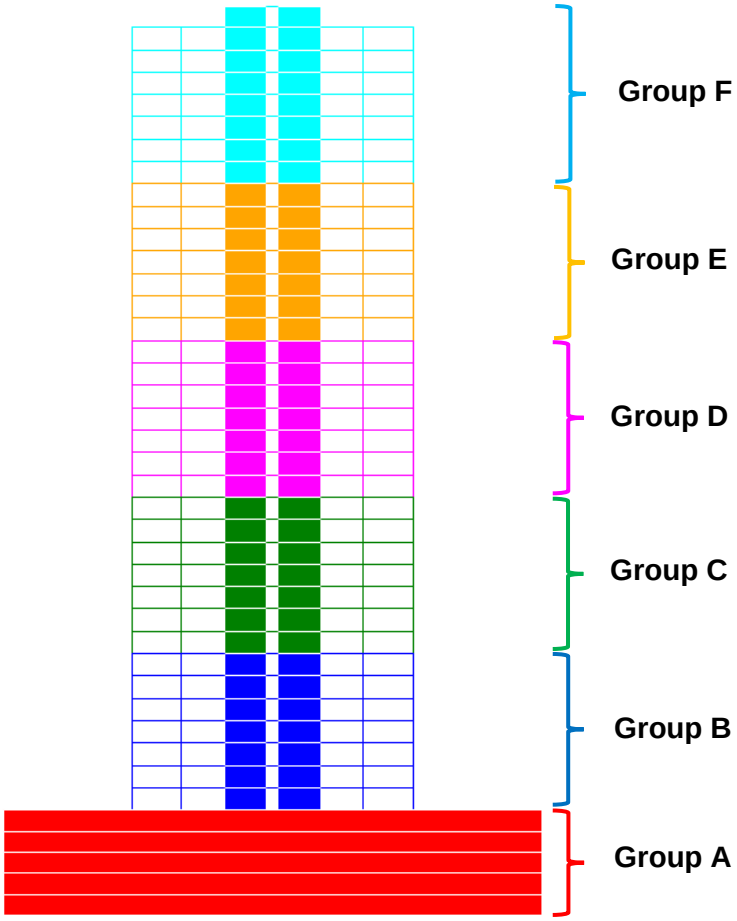

Figure 3.6. Labeling structural elements as groups for design purposes.

Table 3.7. The cross-sectional dimensions (cm) of structural members.

	Group A	Group B	Group C	Group D	Group E	Group F
Basement Columns	100X100	N/A				
Perimeter Columns	160X160	140X140	120X120	100X100	80X80	70X70
Interior Columns	170X170	150X150	130X130	110X110	90X90	70X70
Basement Walls	50	N/A				
Perimeter Beams	N/A	50X70				
Secondary Beams	40X60					
Coupling Beams	50X80					
Structural Walls	110	110	100	90	80	70
Tower Slab	N/A	30				
Transfer Slab	50	N/A				
Basement Slab	30	N/A				
Core Wall Slab	20					

3.5. Nonlinear Modelling and Analysis

Seismic performance assessment is applied using explicit non-prescriptive/nonlinear procedures. Deformation-controlled response components (ductile), expected to experience high inelastic deformation, are modeled besides force-controlled response components (brittle) expected to remain elastic. Columns, frame beams, coupling beams, and structural walls are structural components that were nonlinearly modeled. In contrast, basement slabs and perimeter retaining walls were considered linear-elastic in the analytical model. As with Design Stage 2, expected values of compressive strength of concrete and yield strength of reinforcing steel were utilized for actual performance capabilities in compliance with the quantities stated in TBSC [74] Table 5.1.

Nonlinear time-history analyses (NLTHA) of the building model were performed under DD-1 level ground motions for the deformation-based assessment and detailed design of the structural members by utilizing CSI PERFORM 3D [19]. Collapse prevention performance level was tried to be achieved in the design due to the specifications in the TBSC [74], and other supplementary codes [3], design guidelines [54, 56, 1], and recommendations [59].

3.5.1. Component Behavior Classification

As per TBSC [74], nonlinearly modeled deformation-controlled components were:

- Structural walls under biaxial flexure and axial load (P-M2-M3),
- Coupling beams with conventional reinforcement under flexure,
- Coupling beams with diagonal reinforcement under shear,
- Frame beams under flexure,
- Columns under biaxial and axial load (P-M2-M3).

Force-controlled components to be modeled linear-elastically:

- Shear forces in all members (except coupling beams with diagonal reinforcement),
- Columns under pure uniaxial compression which almost does not exist,
- Diaphragm forces in slabs.

3.5.2. Types of Nonlinear Models

Inelastic structural behavior is classified based on the plasticity expected to develop in the components. Various modeling options are available, from phenomenological hinge models to more physical continuum models. These mathematical models describing the stress-strain relationship of structural members after yielding, mainly focus on concentrated and distributed plasticity. In this study, plastic hinges (concentrated plasticity) for beams and columns and fiber sections (distributed plasticity) for boundary regions of structural walls were employed.

Inelastic deformations concentrate at the two ends of frame members where plastic hinges (lumped plasticity) are defined. It is assumed that all plastic deformations (mainly the hinge rotation) are concentrated at the zero-length plastic hinges. The inelastic behavior of the component is defined with the backbone curves which exhibit the nonlinear force-deformation behavior. The region between the two ends is modeled utilizing linear elastic line elements.

In fiber models, uniaxial stress-strain relationships for both concrete and reinforcing steel in several discrete fibers distributed along the length of the element are numerically

integrated to represent the nonlinear behavior of the component. In this model, plane sections remain plane assumption is valid. Despite the plastic hinge model, fiber models can capture the nonlinear behavior of a component along its length. Nevertheless, this model is more computationally intensive.

3.5.3. Modeling of Frame Elements

As TBSC [74] section 5.4.2 recommends, the nonlinear behavior of moment resisting reinforced concrete columns and beams was modeled by zero-length concentrated plastic hinges at the end regions. Moment-rotation hinges for flexural behavior of the beams, plastic shear hinges for coupling beams, and P-M-M hinges accounting for biaxial bending under axial stresses in columns were assigned to the potential inelasticity zones. Linear-elastic line components were used to represent the area between the plastic hinges. Yield moment (strength), moment vs. plastic rotation relationships, and hysteretic characteristics of plastic hinges were defined as well as shear strength at critical regions.

For the confined concrete strength, volumetric ratios in X and Y directions, the average distance between tied longitudinal bars, and the confined core area were computed individually for each cross-section, while using expected strength values for the concrete and reinforcing steel. Sectional analyses in XTRACT software [10] were employed to represent the moment-curvature relationship and P-M-M interaction of the reinforced concrete frame members and calculate their yield strength, while the uniaxial stress-strain relationship was characterized by Mander confined concrete model [43]. The parabolic strain hardening model was used for reinforcing steel in sectional analyses. The columns have a square cross-section; hence the moment capacity is expected to be the same for local axes 2 and 3. Nonetheless, the axial load levels can be different. Under the analysis of gravity loads, the average axial load was calculated per structural element group to be used in the moment-curvature analyses since axial load levels did not vary significantly among the columns in a specified group. For the computation of effective yield moment, strain limits for concrete and reinforcing steel were taken as $\varepsilon_c = 0.0035$ and $\varepsilon_s = 0.01$, respectively. For the confined concrete crushing strain, the total volumetric ratio was employed. The elastic modulus of the concrete was calculated as:

$$E_c = 5000\sqrt{f_{ce}} = 40311 \text{ MPa} \cdot \tag{3.16}$$

Effective stiffness modifiers for linear-elastic regions were computed by utilizing Equation (3.17) after calculating the yield rotation sections with Equation (3.18) by Biskinis and Fardis [8] accounting for flexural deformation, shear deformation, and bond-slip (yield penetration), respectively as follows:

$$(EI)_{ef} = \frac{M_y}{\theta_y}\frac{L_s}{3} \tag{3.17}$$

$$\theta_y = \frac{\phi_y L_s}{3} + 0.0015\eta\left(1 + 1.5\frac{h}{L_s}\right) + \frac{\phi_y d_b f_{ye}}{8\sqrt{f_{ce}}} \cdot \tag{3.18}$$

Effective yield moment (M_y) and effective yield curvature (ϕ_y) values were obtained from the moment-curvature analysis.

Based on the capacity design approach, to reduce the amount of damage to the structure when subjected to destructive lateral loads mainly imposed by earthquakes, the beams shall be designed to deform before the columns. This is because if any column is vulnerable to collapse due to potential plastic hinges to be formed at the lower and upper ends, the structure may immediately experience excessive displacement demands that eventually lead to collapse. However, if the beams are damaged or collapse, the structure may sustain some damage, but prevent the total collapse. As a result, beams should behave more ductile than columns.

The beams' compound component was composed of an elastic end zone, a plastic hinge component, an elastic segment with a uniform cross-section, a second plastic hinge, and a second elastic end zone, as well as shear strength sections at the plastic hinge locations, to ensure that the shear strength was not exceeded [19]. Compared to the beams', the columns' compound components, were adjusted with the P-M2-M3 hinge component and stiff end zones at the ends. Elastic components remain mostly linear, while inelastic components are always nonlinear. Shear strength demand-capacity ratios at interior locations in beam and column components were calculated using the strength sections.

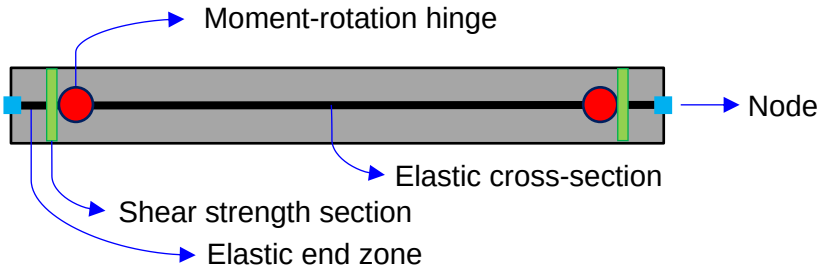

Figure 3.7. Modeling of frame beams.

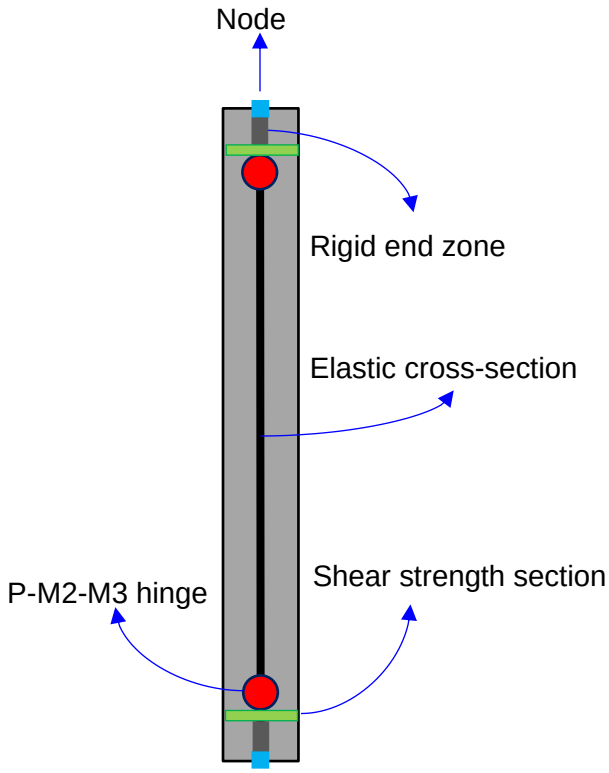

Figure 3.8. Modeling of frame columns.

Monotonic backbone curves can be converted into hysteretic backbone curves, including cyclic strength and stiffness degradation properties. For frame members, ASCE 41-17 [3] already specifies nonlinear modeling parameters and acceptance criteria for plastic rotations in constructing backbone curves, while it does not refer to any specific hysteretic rule. TBSC [74], however, recommends the implementation of elastic–perfectly (infinitely) plastic backbone curves rather than any prescribed backbone curve forms. It also permits ignoring strain hardening and strength loss properties in the moment-plastic rotation relationships. While applying the TBSC [74] procedure, we adopted energy factors

suggested by Naish et al. [50] for stiffness degradation in our model. CSI PERFORM 3D [19] is not capable of applying unloading stiffness factors to elastic-perfectly plastic force-deformation relationships. Therefore, a minimum level of strain hardening (5%) was introduced to the backbone curves to obtain a cyclic behavior similar to the peak-oriented hysteretic rule. Maximum compression load (pure compression), maximum tension load, maximum bending moment (balance point), the bending moment at $P = 0$ (pure bending) for the P-M2-M3 interaction in the hinge definition of the columns were employed. Since no cyclic degradation parameters were defined for the columns, strength loss was not considered. Although strength loss after peak strength was not considered in the elastic-perfectly plastic model, plastic deformation limits in TBSC [74] were set such that allowable plastic rotations were not near to the structural members' rotation capacity [52]. This brings a conservative approach compared to ASCE 41-17 [3] plastic rotation limits.

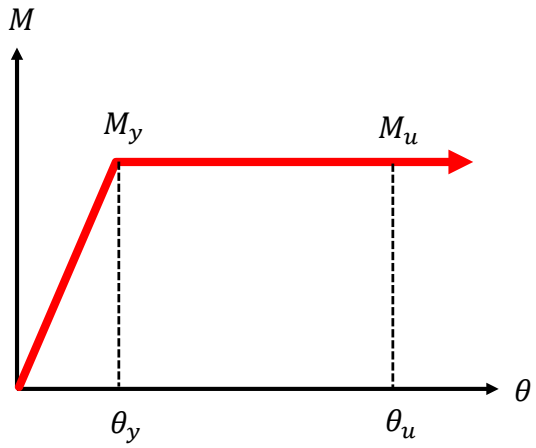

Figure 3.9. Elastic-perfectly plastic backbone curve.

Plastic rotation capacity corresponding collapse prevention limit for frame members was calculated by using the following empirical equation:

$$\theta_P^{(CP)} = \frac{2}{3}\left[(\phi_u - \phi_y)L_p\left(1 - 0.5\frac{L_p}{L_s}\right)\right] + 4.5\phi_u d_b \cdot \tag{3.19}$$

For the calculation of ultimate curvature (ϕ_u) in Equation (3.19), the collapse prevention strain limit of confined concrete was determined by Equation (3.20):

$$\varepsilon_c^{(CP)} = 0.0035 + 0.04\sqrt{\omega_{we}} \leq 0.018 \tag{3.20}$$

where

$$\omega_{we} = \alpha_{se}\rho_{sh,min}\frac{f_{ywe}}{f_{ce}} \tag{3.21}$$

$$\alpha_{se} = \left(1 - \frac{\sum a_i^2}{6b_o h_o}\right)\left(1 - \frac{s}{2b_o}\right)\left(1 - \frac{s}{2h_o}\right) \tag{3.22}$$

$$\rho_{sh} = \frac{A_{sh}}{b_k s}. \tag{3.23}$$

Collapse prevention strain limit for the reinforcing steel was taken as:

$$\varepsilon_s^{(CP)} = 0.4\varepsilon_{su}. \tag{3.24}$$

Shear was defined as the nominal elastic strength of perimeter frame beams. We do not anticipate perimeter beams to suffer inelastic deformation in shear, unlike coupling beams. Their behavior is notably governed by flexural deformations.

Typically, we needed to calculate the shear capacity of the column at the span. Since the column dimensions are relatively big and the story height is relatively low, we confined the entire length of the column with the same interval. Thus, shear reinforcement is constant along with the span of the columns.

3.5.4. Modeling of Coupling Beams

Coupling beams with a low span-to-depth ratio (e.g., $L/h < 4.0$) are the structural members expected to dissipate most of the inelastic energy during the nonlinear response history of the structure. Therefore, the hysteretic behavior and acceptance criteria of these elements shall be accurately defined since the inelastic damping characteristics of the tall building can be particularly affected by their response [52].

As TBSC (2018) Section 5.4.3.3 allows the utilization of special modeling techniques for coupling beams, diagonally reinforced coupling beam, the so-called nonlinear shear hinge model was decided to use for the building model of interest. For coupling beams, we did not define end zones since all coupling beams were connected to structural walls in their strong direction.

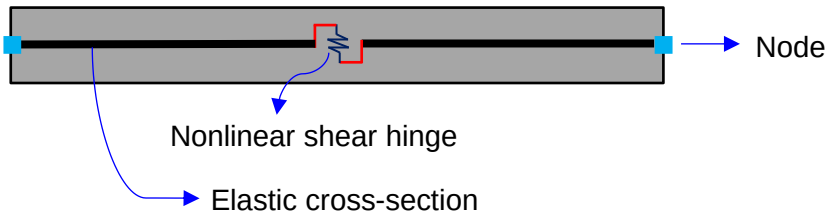

Figure 3.10. Modeling coupling beams.

Deformation measure for demand/capacity calculations was defined in terms of plastic rotations for flexure-controlled members, and chord rotations for shear-controlled members as stated in ASCE 41-17 [3]. The shear displacement, hence, the deformation demand/capacity ratio, was estimated by assigning rigid-plastic shear springs to the mid-span. Effective stiffness properties for linear-elastic regions of coupling beams designed with conventional reinforcement were calculated by using Equations (3.17) and (3.18), and plastic rotation capacity was obtained by Equation (3.19) similar to the procedure defined for the frame elements. The plastic deformation of the displacement type shear spring was obtained from the plastic rotation capacity as follows:

$$\theta_p = \frac{\Delta_p/2}{L/2} = \frac{\Delta_p}{L}. \tag{3.25}$$

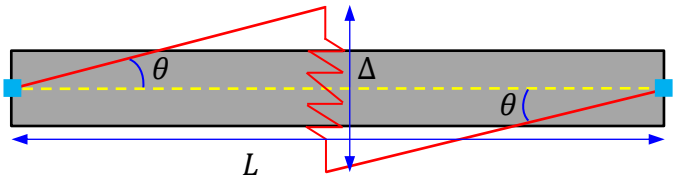

Figure 3.11. Illustration of the chord rotation (Δ) for shear-controlled members.

3.5.5. Modeling of Structural Walls

The structural wall system is the major load resisting part of tall buildings, and they should be accurately modeled for reliable nonlinear behavior. All possible failure modes along with the wall height, stiffness, and strength degradation characteristics during the time history of the structure shall be properly represented.

As TBSC [74] Section 5.4.3.2 specifies, the nonlinear flexural (P-M2-M3) behavior was modeled by using fiber model elements. In fiber modeling, wall sections were subdivided into concrete and steel fibers. Uniaxial stress-strain relationships were applied for each fiber segment. Nonlinear flexural deformations along the structural wall were numerically integrated with each analytical time step by CSI PERFORM 3D [19]. Following assumptions were made: (1) plane sections remain plane after bending, (2) shear (elastic or inelastic) and flexural behaviors are uncoupled.

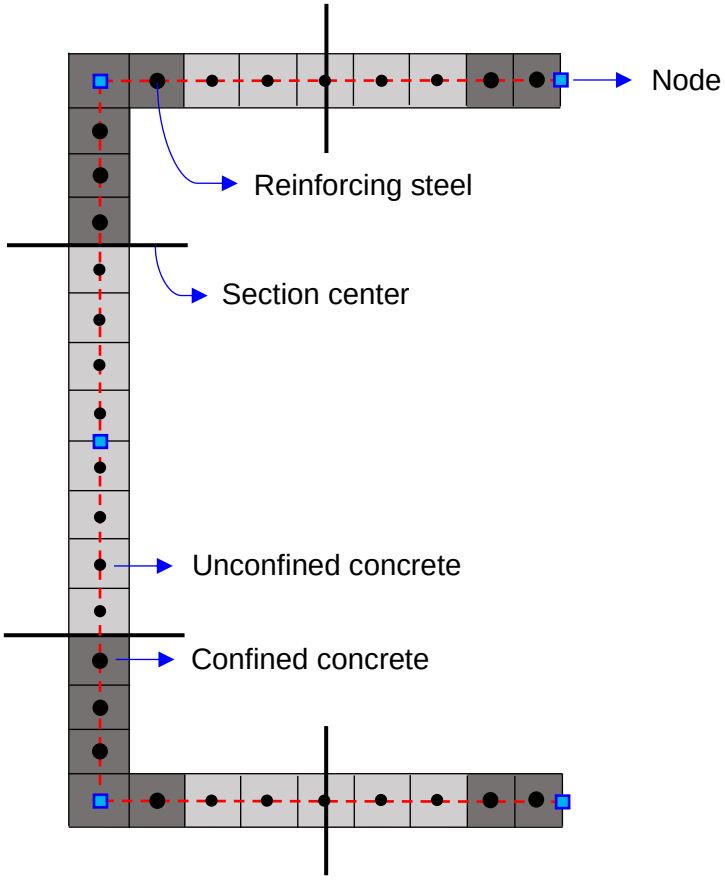

Figure 3.12. Fiber modeling of structural walls.

A fiber model has no rotational DOF at its nodes, only represents the vertical axial/flexural features of the structural wall. Linear-elastic stiffness modifiers (effective shear) were assigned to the fibers to accommodate horizontal axial and bending behaviors. The reinforcement ratio and the concrete model for boundary and web regions are different. The area, coordinate and material type of each fiber cell was defined manually in "Fixed Size" cross-sections in which different materials can be arranged together in CSI PERFORM 3D [19]. The width of the fiber element shall be identical to the width of the fixed cross-section.

For modeling the structural walls, the linearized stress-strain relationship of the confined concrete material model was defined with regard to TBSC [74] Section 5A.1 while tensile strength was neglected. The computation process began with determining the effective confinement coefficient (k_e) as:

$$k_e = \left(1 - \frac{\sum a_i^2}{6 b_o h_o}\right)\left(1 - \frac{s}{2 b_o}\right)\left(1 - \frac{s}{2 h_o}\right)\left(1 - \frac{A_s}{b_o h_o}\right)^{-1} . \tag{3.26}$$

The average effective confining pressure (f_e) was then calculated for two perpendicular directions in rectangular sections as follows:

$$f_{ex} = k_e \rho_x f_{sye} \tag{3.27}$$

$$f_{ey} = k_e \rho_y f_{sye} . \tag{3.28}$$

Following that, we determined the compressive strength magnification factor (λ_c) of confined concrete as:

$$\lambda_c = 2.254 \sqrt{1 + 7.94 \frac{f_e}{f_{co}}} - 2 \frac{f_e}{f_{co}} - 1.254 \tag{3.29}$$

where

$$f_e = \frac{f_{ex} + f_{ey}}{2} \cdot \tag{3.30}$$

Then, the modified compressive strength of concrete (f_{cc}) was estimated as:

$$f_{cc} = \lambda_c f_{co} \cdot \tag{3.31}$$

Meanwhile, the modified strain (ε_{cc}) corresponds to confined concrete modified compressive strength was estimated as:

$$\varepsilon_{cc} = \varepsilon_{co}[1 + 5(\lambda_c - 1)] \tag{3.32}$$

where

$$\varepsilon_{co} = \frac{(f_{co})^{0.25}}{1150} \cdot \tag{3.33}$$

Further, the elasticity modulus of unconfined concrete (E_c) was determined as:

$$E_c = 5000\sqrt{f_{co}} \cdot \tag{3.34}$$

Additionally, the secant elasticity modulus of confined concrete (E_{sec}) was computed to employ in further calculations of strength-related parameters following:

$$E_{sec} = \frac{f_{cc}}{\varepsilon_{cc}} \cdot \tag{3.35}$$

Subsequently, the parameters used to generate the stress-strain relationship of confined concrete were calculated as follows:

$$x = \frac{\varepsilon_c}{\varepsilon_{cc}} \tag{3.36}$$

$$r = \frac{E_c}{E_c - E_{sec}} \cdot \tag{3.37}$$

In the last stage, the amplified strength of confined concrete (f_c) was plotted to linearize and utilize in the nonlinear analytical model following:

$$f_c = \frac{f_{cc} x r}{r - 1 + x^r} \cdot \tag{3.38}$$

Based on the thickness of the wall, confinement properties, and the critical wall height (H_{cr}), the linearized stress-strain relationships of the confined concrete materials were compared. A similar pattern was observed for the confined concrete materials above the critical height. For the sake of simplicity, confined concrete models were classified based on the critical wall height for the same thickness of 110 cm. The descending part of the stress-strain relationships was extended linearly to the zero stress for the possible excessive compressive strains in the nonlinear response. For the cyclic stiffness degradation parameters for concrete, recommended values by Lowes et al. [42] were utilized.

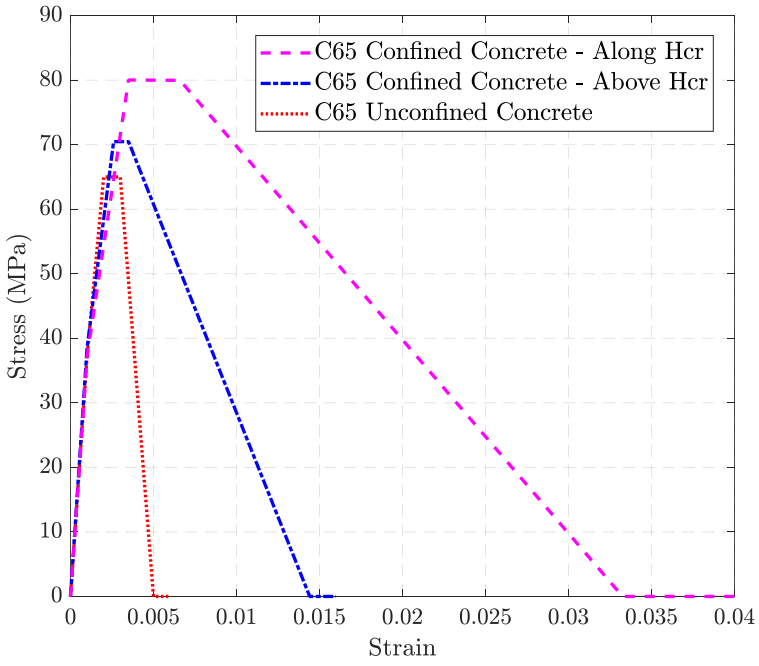

Figure 3.13. Linearized stress-strain relationships of concrete material models.

The linearized stress-strain relationship of B420C grade reinforcing steel by applying Equations (3.39) through (3.41) in TBSC [74] Section 5A.2. was also defined while accounting for cyclic degradation due to the Bauschinger effect with energy factors and unloading stiffness factor in nonlinear modeling as:

$$f_s = E_s \varepsilon_s \qquad (\varepsilon_s \leq \varepsilon_{sy}) \tag{3.39}$$

$$f_s = E_s \varepsilon_s \qquad (\varepsilon_s \leq \varepsilon_{sy}) \tag{3.40}$$

$$f_s = f_{su} - (f_{su} - f_{sy}) \frac{(\varepsilon_{su} - \varepsilon_s)^2}{(\varepsilon_{su} - \varepsilon_{sh})^2} \qquad (\varepsilon_{sh} < \varepsilon_s \leq \varepsilon_{su}) \cdot \tag{3.41}$$

Table 3.8. Reinforcing steel material properties.

E_s	f_{sye}	ε_{sye}	ε_{sh}	ε_{su}	f_{su}
200 GPa	504 MPa	0.0025	0.008	0.08	605 MPa

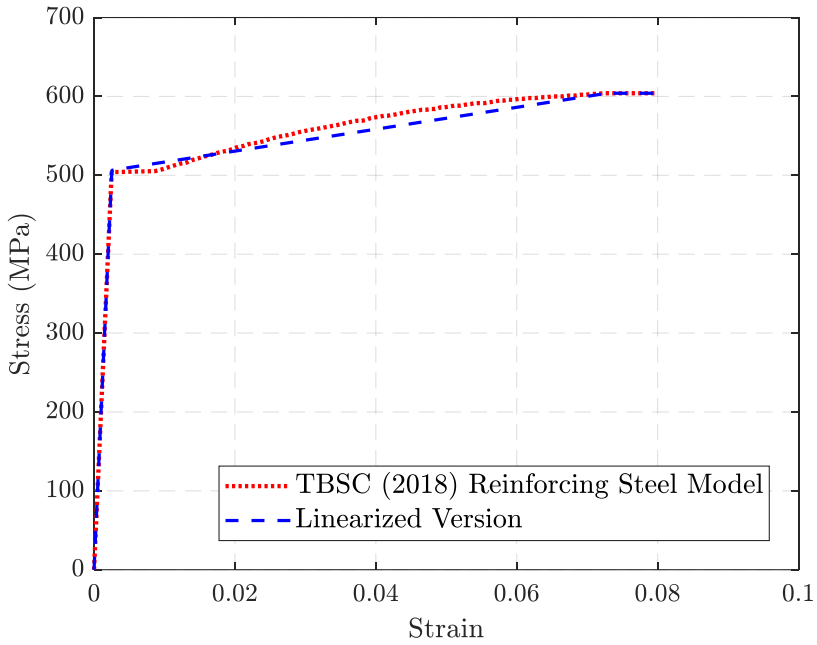

Figure 3.14. Stress-strain relationship of reinforcing steel.

3.5.6. Other Modeling Details

1. Given that the fiber models defined for structural walls have no rotational DOF, an embedded beam is modeled inside the structural wall to establish the correct behavior between the coupling beam and the structural wall if the coupling beam connects to a structural wall diagonally or in-plane direction (strong axis) of the structural wall in CSI PERFORM 3D [19]. Linear-elastic embedded beams offer a fixed (rigid) connection between coupling beams that link the core wall structural system in a strong direction. Otherwise, the connection remains a pin connection, with no distribution of moment to the coupling beams. To enable this manipulation, we define the flexural stiffness of the embedded beams (EI/L), as 20 times of the coupling beams, ensuring that embedded beams remain linear-elastic. However, the axial rigidity of embedded beams was not magnified since it contributes to structural wall stiffness and likely to alter the behavior of the structural system.

2. Since nonlinear behavior under axial or in-plane flexural behavior was not anticipated in the basement walls, they were assumed to remain linear-elastic.

3. Slavings were assigned to the tower floors' nodes for the rigid diaphragm behavior, whereas the transfer floor and the floor below of the podium were modeled with elastic/flexible shell elements to distribute the seismic forces to the retaining walls accurately and avoid backstay effects.

4. The design load is the combination of both horizontal and vertical components of ground motions. Contrary to Design Stages 1 and 2, gravity loads cannot be linearly superimposed with the earthquake loads. They are used to obtain initial deformations, capacities, or stiffnesses of structural members prior to the earthquake loads. For to be an initial state of earthquake analysis, gravity loads are used in nonlinear static analyses.

5. The vertical ground motion was simulated with a simplified approach used in Design Stages 1 and 2.

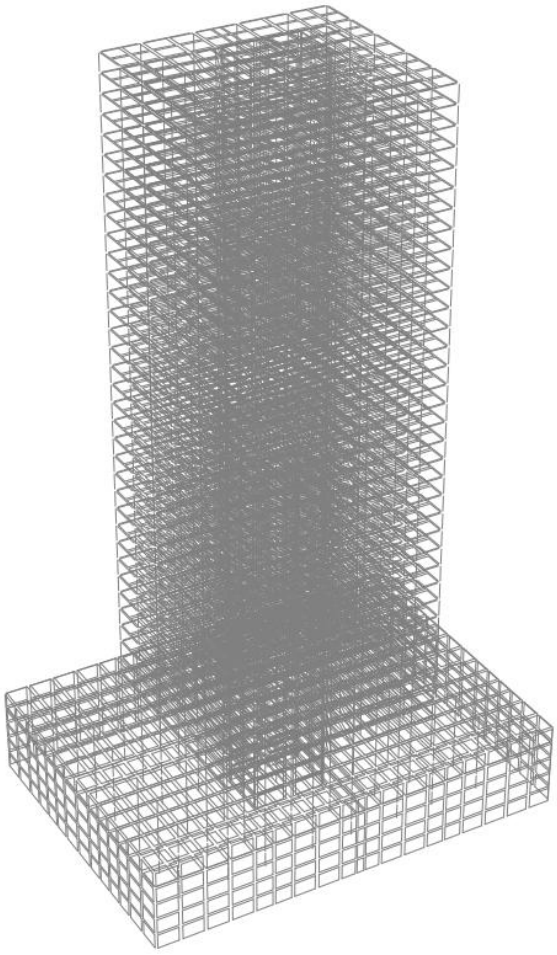

Figure 3.15. Nonlinear building model generated in CSI PERFORM 3D [19].

3.5.7. Selecting and Scaling Ground Motion Records

For the nonlinear time-history analyses of the building model, the source of the demand was defined by the ground motions. When selecting and scaling ground motions for a specific structure at a specific location, a target spectrum representing the severity of the expected ground acceleration demands corresponding to the selected ground motion intensity level is needed. Compatible input ground motions selected from the NGA-West2 Ground Motion Database [55] were linearly scaled again by matching the SRSS resultant acceleration spectra of the ground motion components with a target spectrum that is 1.3 times the 5% damped DD-1 level design spectrum as defined in TBSC [74] for the design purposes. However, the 5% damped DD-2 level spectrum was not multiplied with any factor and employed as it was for the ground motion scaling. While designing the building according to the amplified DD-1 level ground motion intensity, the maximum inter-story

drift value as a reference for the subsequent earthquake simulation tests of the fire door samples was planned to be obtained under the DD-2 level ground motion intensity.

For filtering the ground motion data, the following search criteria were specified:

- The range of the magnitude (M_w) as 6.3-7.6
- The range of the Joyner-Boore distance (R_{JB}) as 5-40 km
- The range of the shear wave velocity of the first 30 m soil ($V_{s,30}$) as 300-760 m/s
- The fault type as strike-slip
- The range of the scale factor as 0-7

Table 3.9 lists the eleven pairs of filtered and selected ground motions that matched the specified benchmarks with the lowest mean squared error values and acceptable lowest usable frequencies for better resemblance.

Table 3.9. Selected 11-ground motion for the time-history analyses of the building model.

Record Sequence Number	**Earthquake Name**	**Record Station**	**Modified Scale Factor**		M_w	R_{JB} **(km)**	$V_{s,30}$ **(m/s)**
			DD-1 (MCE Level)	**DD-2 (Design Level)**			
164	Imperial Valley-06 (1979)	Cerro Prieto	5.0	2.0	6.53	15.19	471.53
187	Imperial Valley-06 (1979)	Parachute Test Site	6.0	3.0	6.53	12.69	348.69
850	Landers (1992)	Desert Hot Springs	5.0	2.0	7.28	21.78	359.00
864	Landers (1992)	Joshua Tree	2.5	1.0	7.28	11.03	379.32
884	Landers (1992)	Palm Springs Airport	6.0	3.0	7.28	36.15	312.47
1107	Kobe – Japan (1995)	Kakogawa	3.2	1.0	6.9	22.5	312.00
1166	Kocaeli – Turkey (1999)	Iznik	4.0	3.0	7.51	30.73	476.62
1614	Duzce – Turkey (1999)	Lamont 531	6.5	3.0	7.14	11.46	481.00
1619	Duzce – Turkey (1999)	Mudurnu	6.5	3.0	7.14	34.3	535.24
1633	Manjil - Iran (1990)	Abbar	1.5	1.0	7.37	12.55	723.95
1787	Hector Mine (1999)	Hector	2.4	1.0	7.13	10.35	726.00

In the amplitude scaling procedure, the average of the SRSS resultant spectra of the selected records shall not be less than the spectral accelerations on the target spectrum over a period range between $0.2Tp$ and $1.5Tp$, where Tp is the fundamental period of the building in the direction of shaking. The fundamental period was obtained as $Tp = 4.54\ s$ in the Y direction at Design Stage 1 by using expected material properties and effective stiffness modifiers.

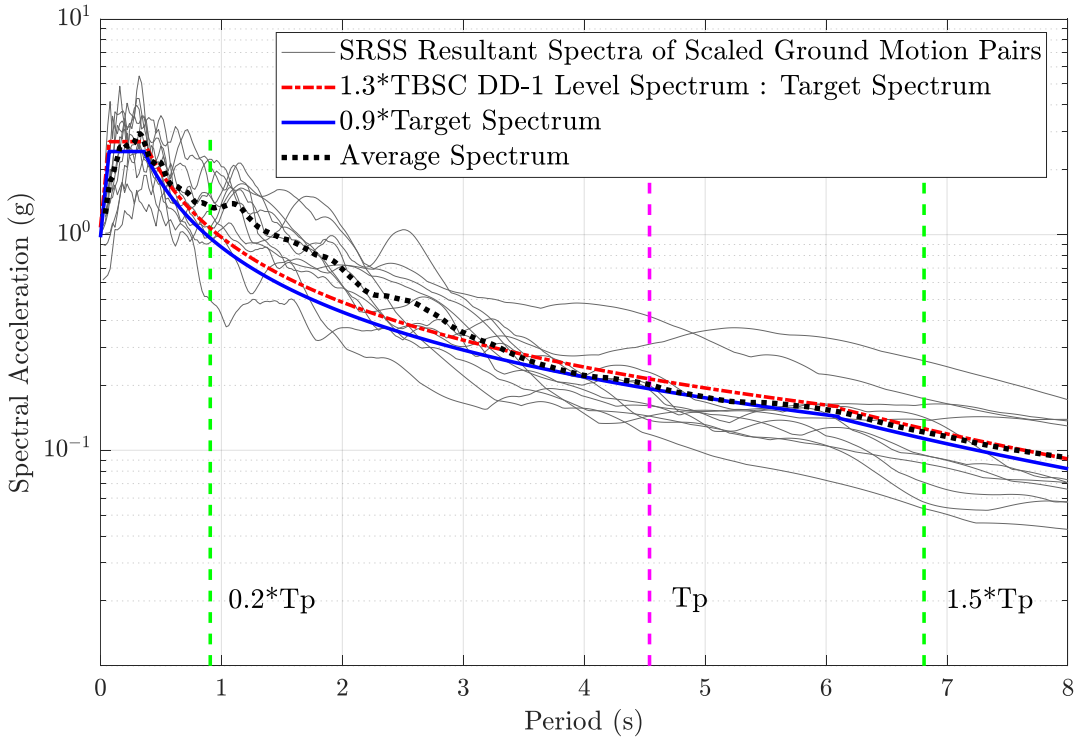

Figure 3.16. DD-1 level SRSS acceleration spectra of the selected ground motions.

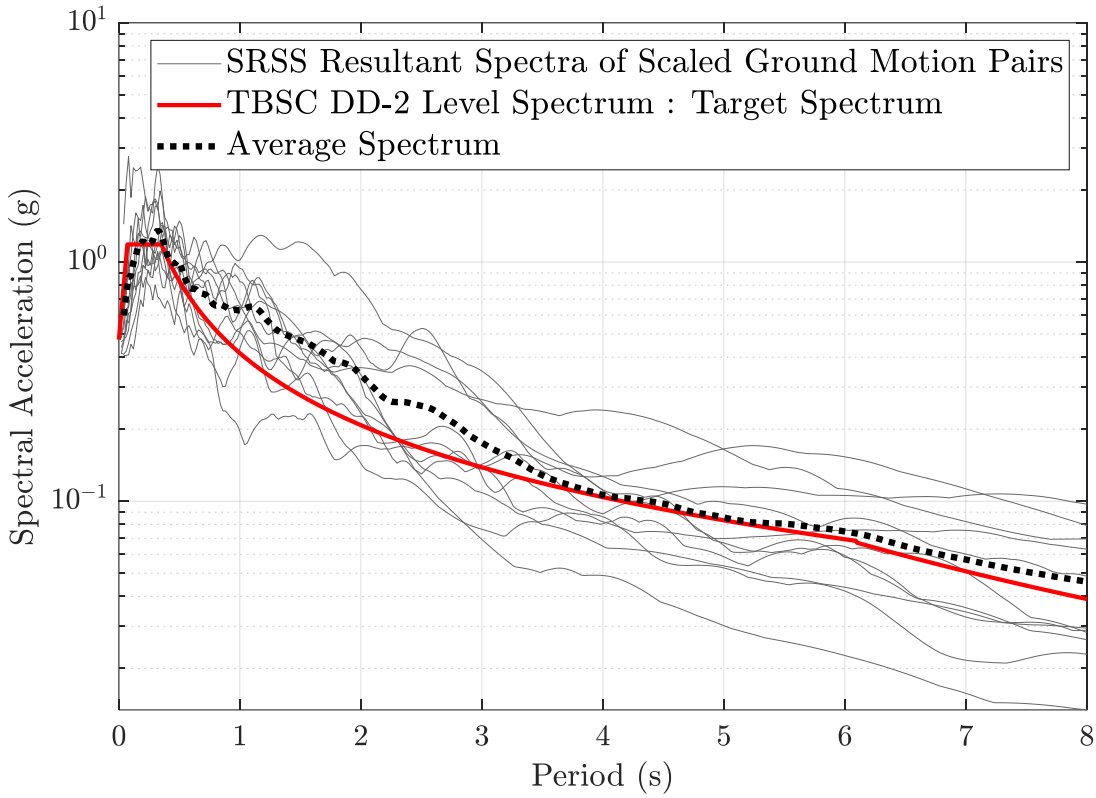

Figure 3.17. DD-2 level SRSS acceleration spectra of the selected ground motions.

3.5.8. Performance Assessment Stage

An overview of the acceptance criteria specified in TBSC [74] for the performance assessment was followed as given in Table 3.10.

Table 3.10. Performance assessment procedure of the tall building model.

Earthquake Level	DD-1 Ground Motion Intensity
Target Performance Level	Collapse Prevention
Analysis Method	Nonlinear time-history history analyses in 3D
Acceptance Criteria	Strain / Plastic rotations / Inter-story drift ratio
Strength and Stiffness Parameters	Expected Strength
Damping Ratio	2.5%
Structural Wall Shear Checks	TBSC (2018) Section 13.6.4.2
Confined Concrete Strain Limits	TBSC (2018) Equation 5.4b
Reinforcement Strain Limits	TBSC (2018) Equation 5.5
Beam Plastic Rotation Limits	TBSC (2018) Equation 5.6
Column Plastic Rotation Limits	TBSC (2018) Equation 5.6
Beam and Column Shear Checks	TBSC (2018) Section 13.6.4.2
Inter-story Drift Ratio Limits	3.0% (mean), 4.5% (maximum)

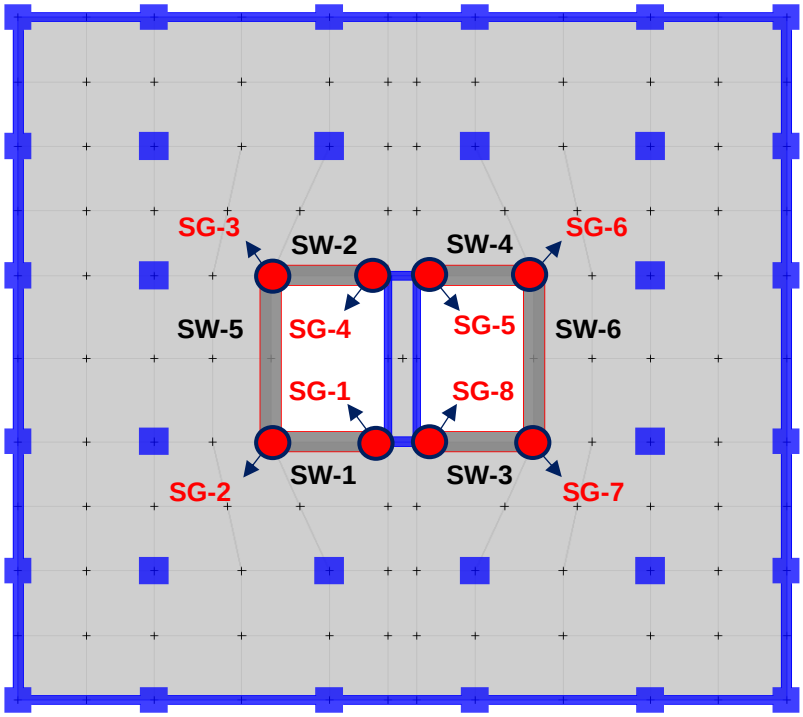

Figure 3.18. Labeling the structural walls and the strain gauges.

The critical shear force demands for the structural walls to be compared with the allowable shear capacities, calculated by following TBSC [74] Section 7.6.7, were based on the largest absolute values from each of the 22 analyses were calculated by adding one standard deviation to the mean. The thickness of the structural walls shall be revised if Equation (3.42) for uncoupled walls and Equation (3.43) for coupled walls are not satisfied:

$$V \leq 0.85 A_{ch} \sqrt{f_{ce}} \tag{3.42}$$

$$V \leq 0.65 A_{ch} \sqrt{f_{ce}} \cdot \tag{3.43}$$

As shown in the following figures, the structural walls have an adequate code-specified shear capacity that does require revision of the wall thickness.

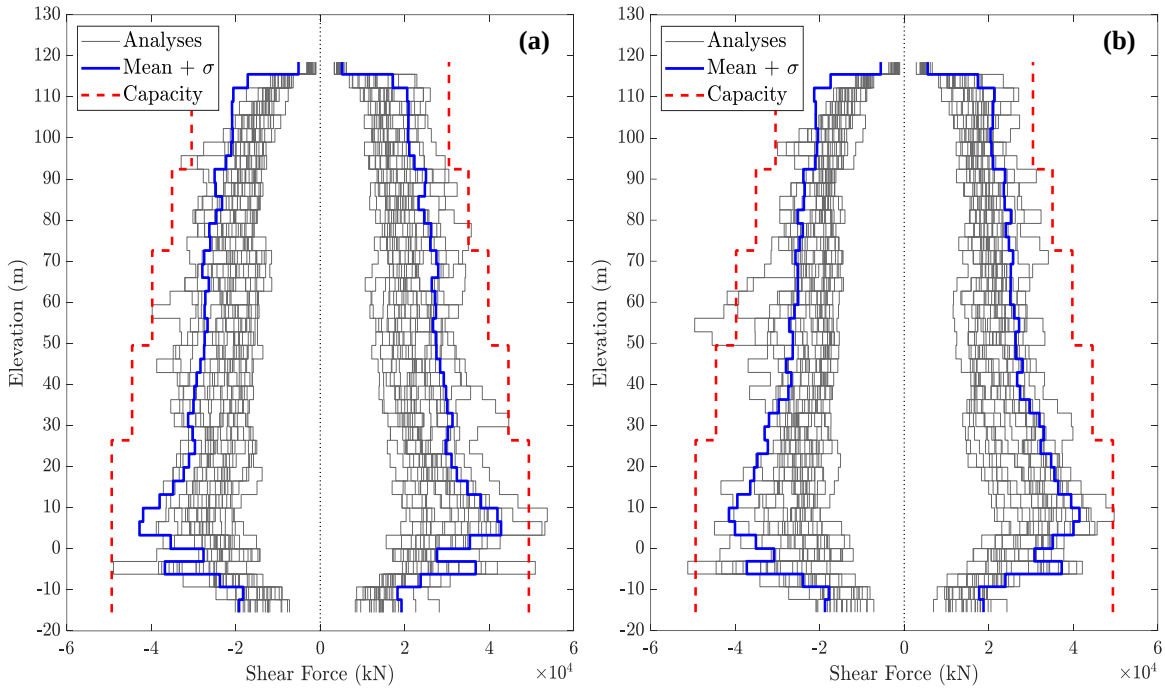

Figure 3.19. Structural wall shear force demand-capacity checks for (a) SW-1 and (b) SW-2.

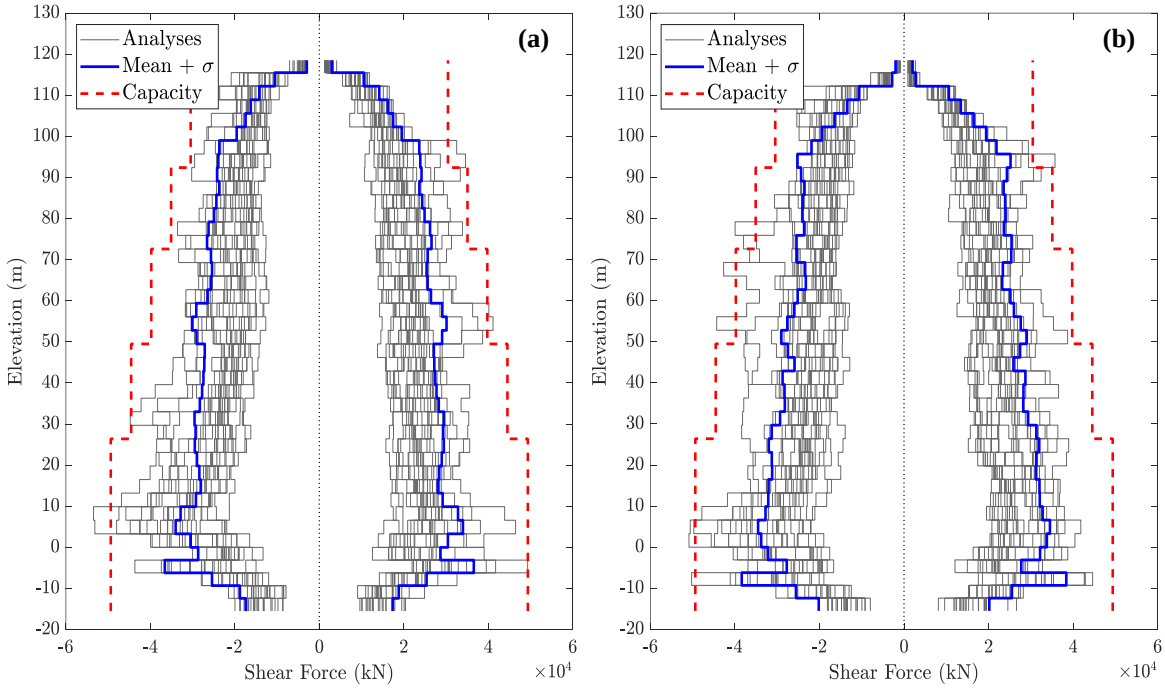

Figure 3.20. Structural wall shear force demand-capacity checks for (a) SW-3 and (b) SW-4.

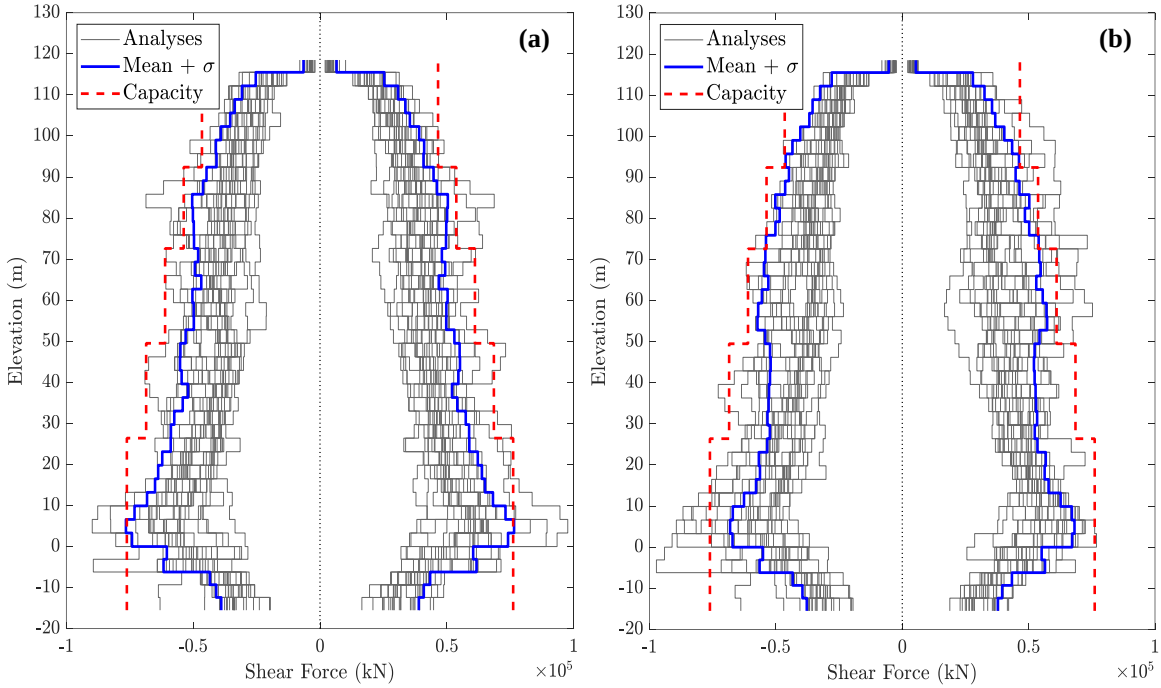

Figure 3.21. Structural wall shear force demand-capacity checks for (a) SW-5 and (b) SW-6.

The inelastic longitudinal strain demands on concrete (compression) and reinforcing steel (tension) in all structural wall cross-sections were investigated under 22-ground motion history at their two ends. The mean strain values were computed to compare with the strain limits specified in TBSC [74] Section 5.8.1.1 for each performance level. Since our target performance level is Collapse Prevention and the strain values in both concrete and steel could not even reach the Life Safety performance level, the design meets the requirements given in the code for the issued 8-strain gauge.

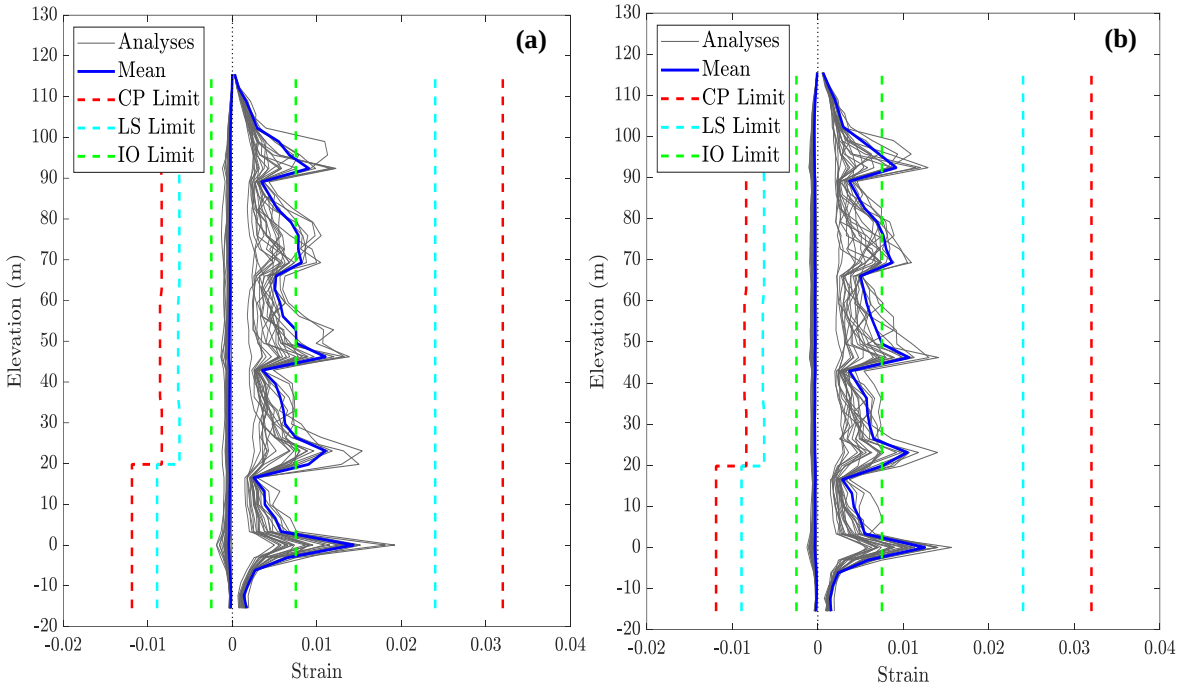

Figure 3.22. Strain gauge readings for the inelastic deformation demands at (a) SG-1 and (b) SG-2.

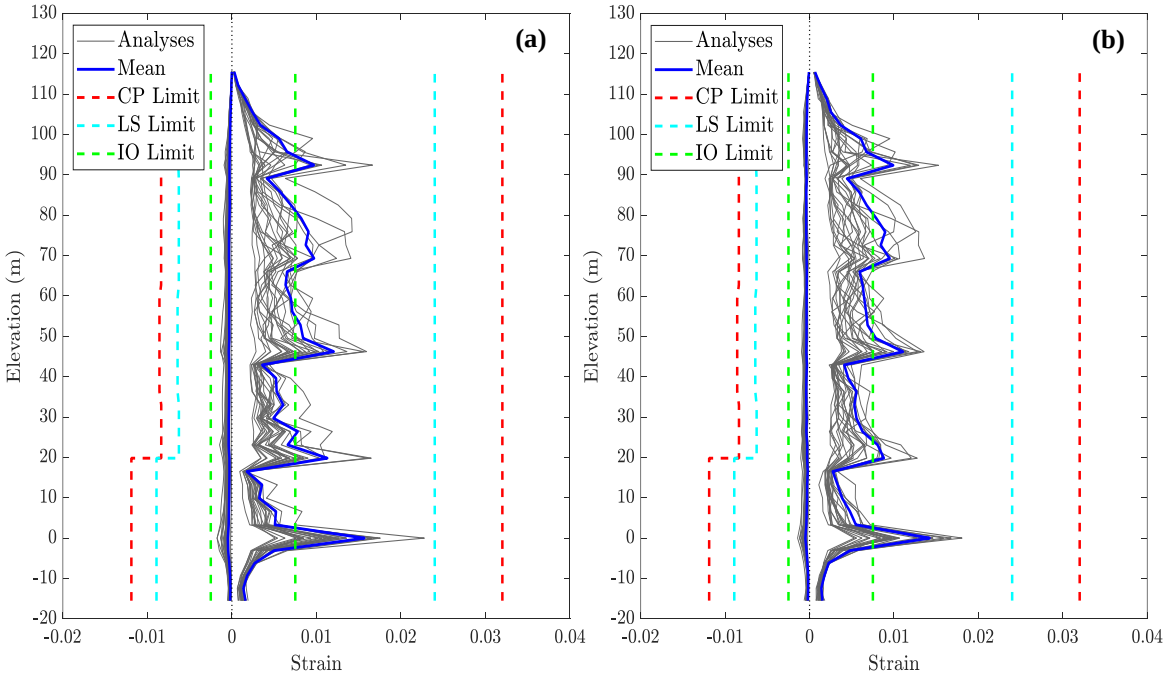

Figure 3.23. Strain gauge readings for the inelastic deformation demands at (a) SG-3 and (b) SG-4.

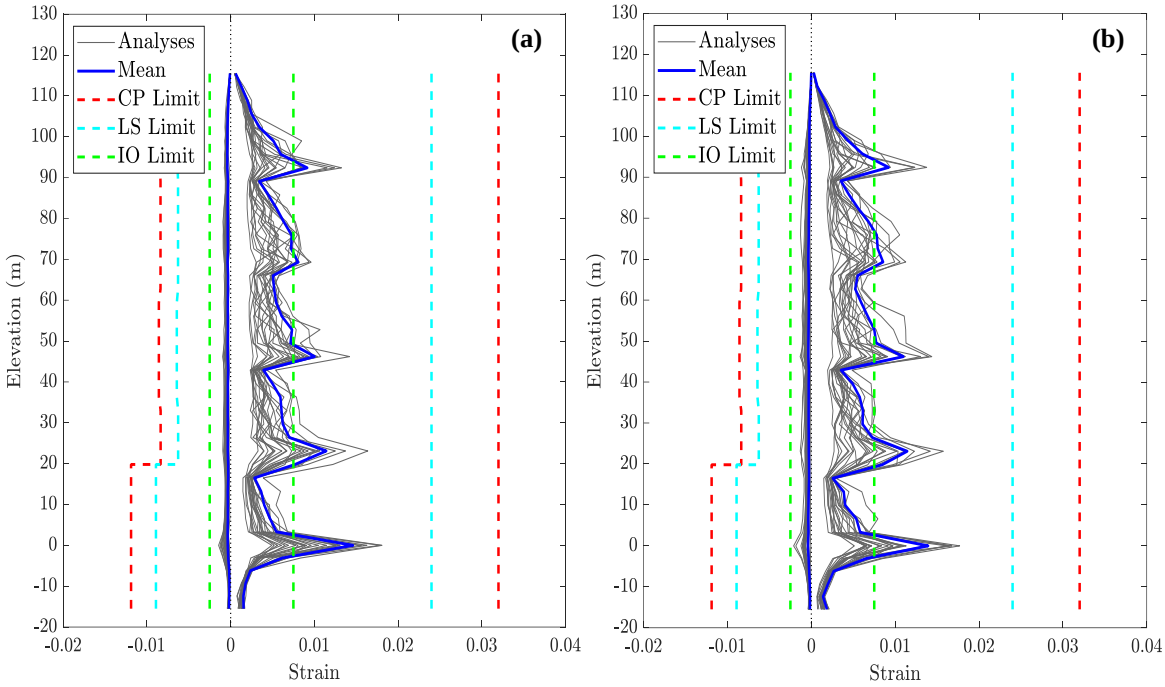

Figure 3.24. Strain gauge readings for the inelastic deformation demands at (a) SG-5 and (b) SG-6.

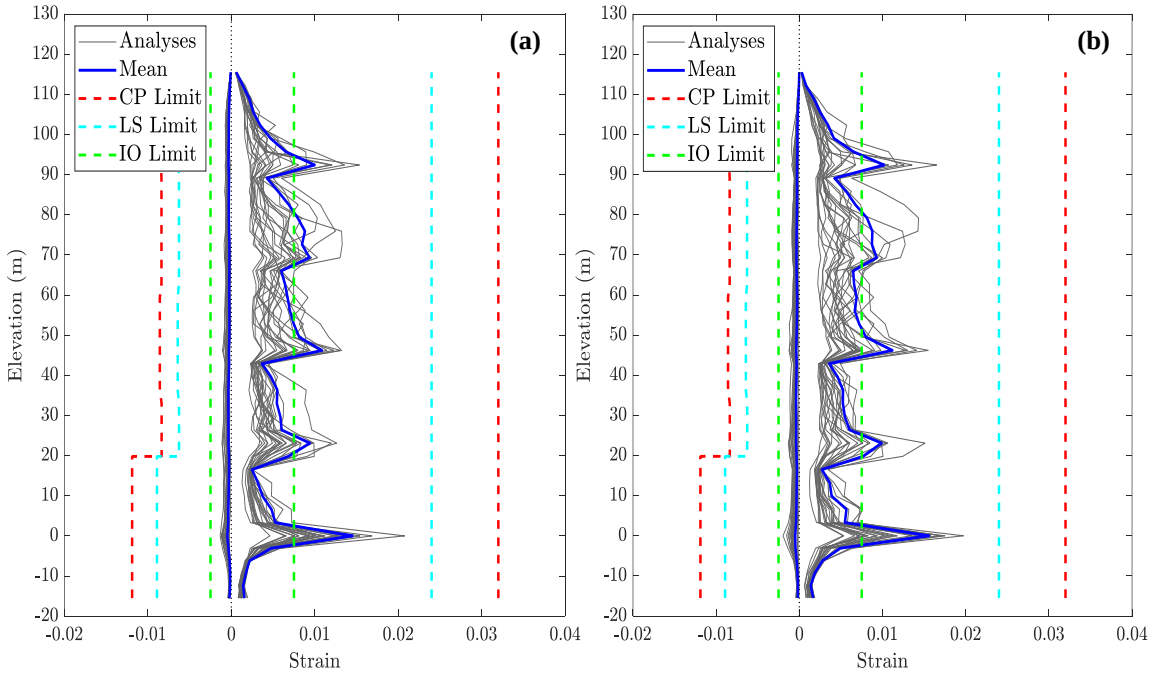

Figure 3.25. Strain gauge readings for the inelastic deformation demands at (a) SG-7 and (b) SG-8.

Following the TBSC [74] Section 5.8.1.2, the mean values of plastic rotations at both ends of all frame beam and column elements under NLTHA were compared with their available capacities. The results approved that the plastic rotation demands are in the safe zone although they reach higher values at the top floors, where the most oscillations are expected to occur in the nonlinear response history of the building model. Figure 3.26 and Figure 3.27 represent only the one loading axis (Axis 2) of one end (I end) of the beam and column elements.

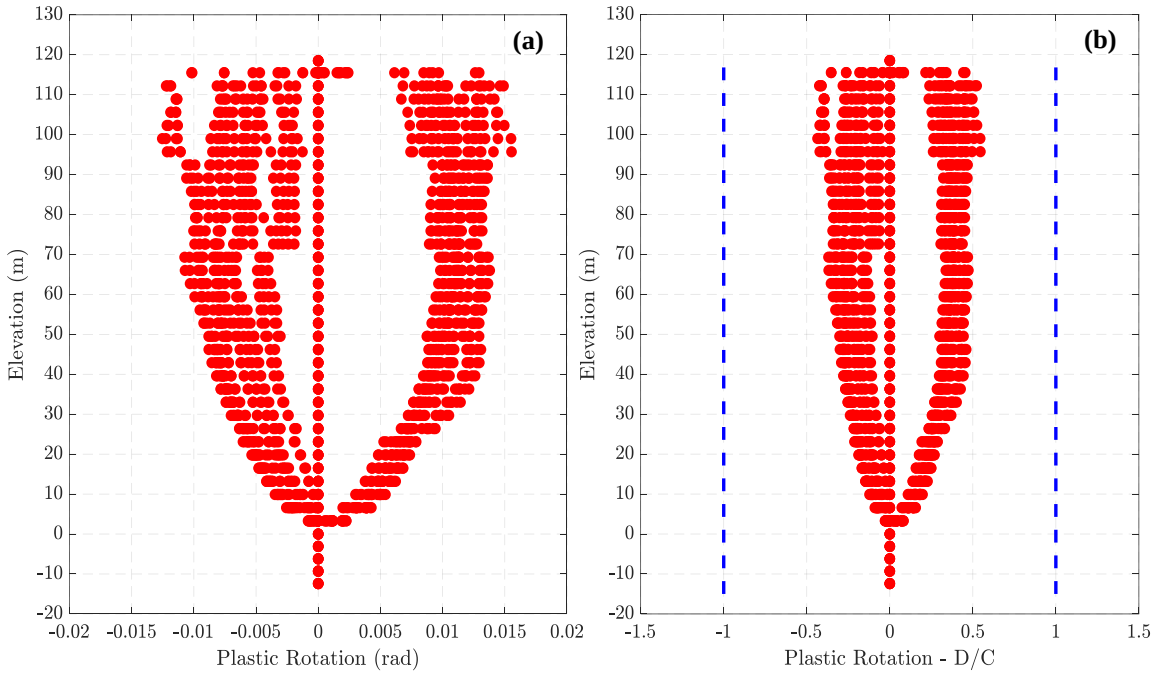

Figure 3.26. Beam plastic rotation (a) demands and (b) demand/capacity ratios.

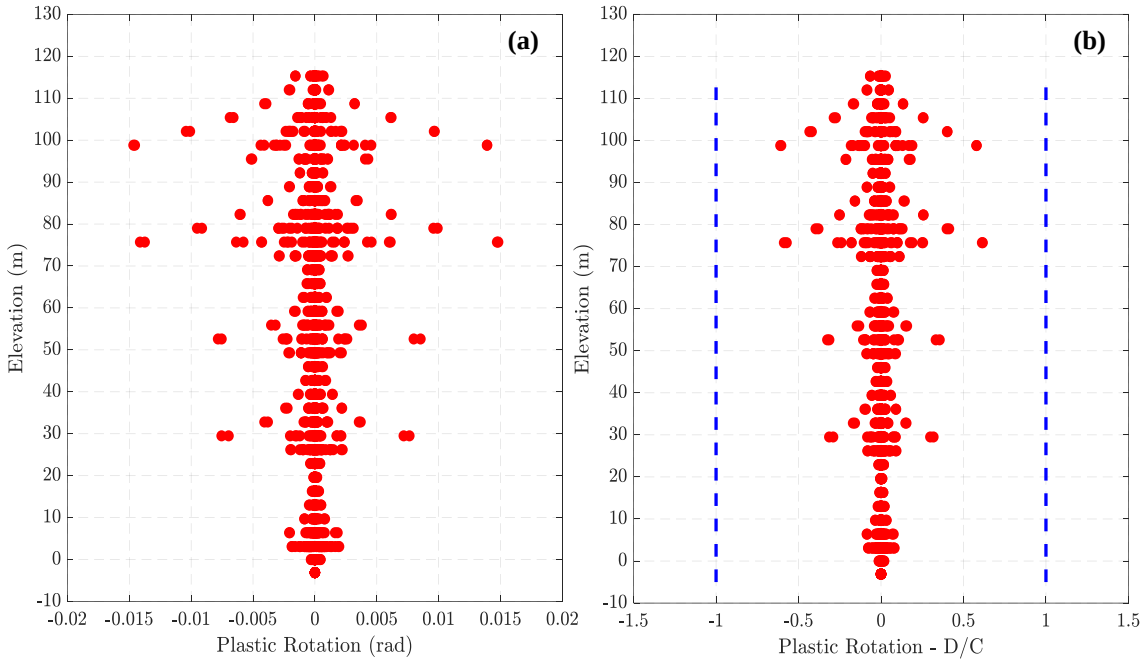

Figure 3.27. Column plastic rotation (a) demands and (b) demand/capacity ratios.

Neglecting the contribution of concrete to shear strength, shear force demands at each end of the beams shall satisfy Equation (3.44), whereas shear force demand on columns shall satisfy Equation (3.45) as:

$$V \leq V_r = V_w = \frac{A_{sw}}{s} f_{ywe} d \tag{3.44}$$

$$V_r = V_c + V_w = 0.52 f_{cte} b_w d \left(1 + \lambda \frac{N_d}{A_c}\right) + \frac{A_{sw}}{s} f_{ywd} d \cdot \tag{3.45}$$

Shear demand/capacity ratios were calculated by taking the lowest shear force capacity of the column and beam elements on each floor. Despite this, Figure 3.28 and Figure 3.29 reveal that the resulting shear demands are quite low in comparison to the capacities for one end (I end) of the frame beams and columns, respectively.

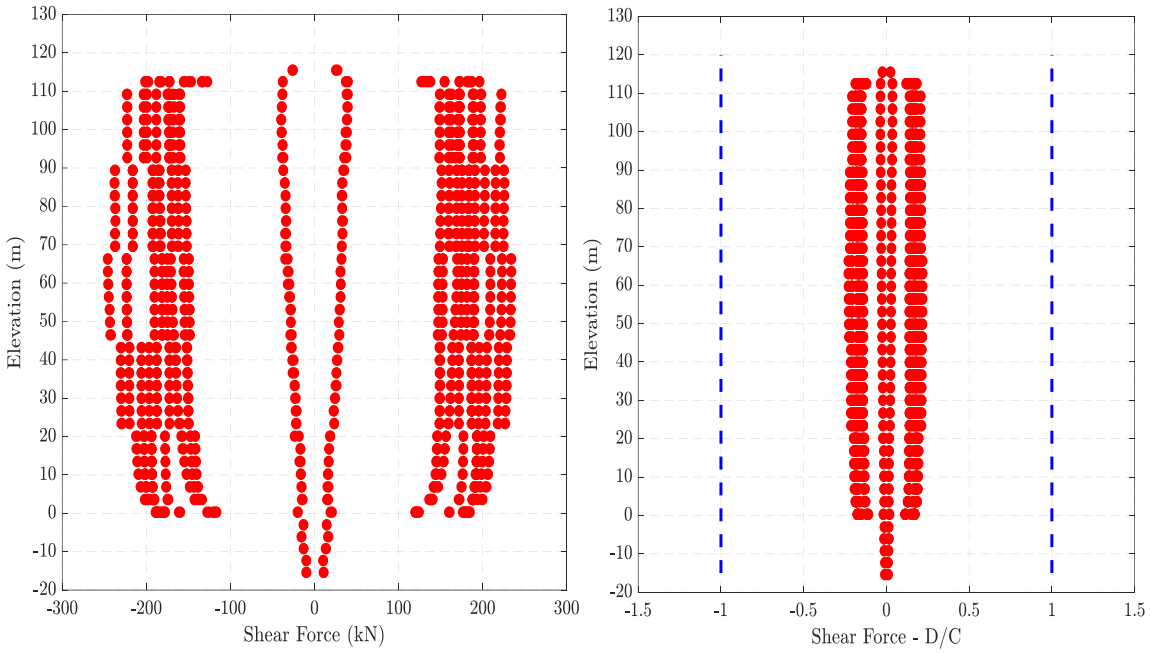

Figure 3.28. Beam shear force (a) demands and (b) demand/capacity ratios.

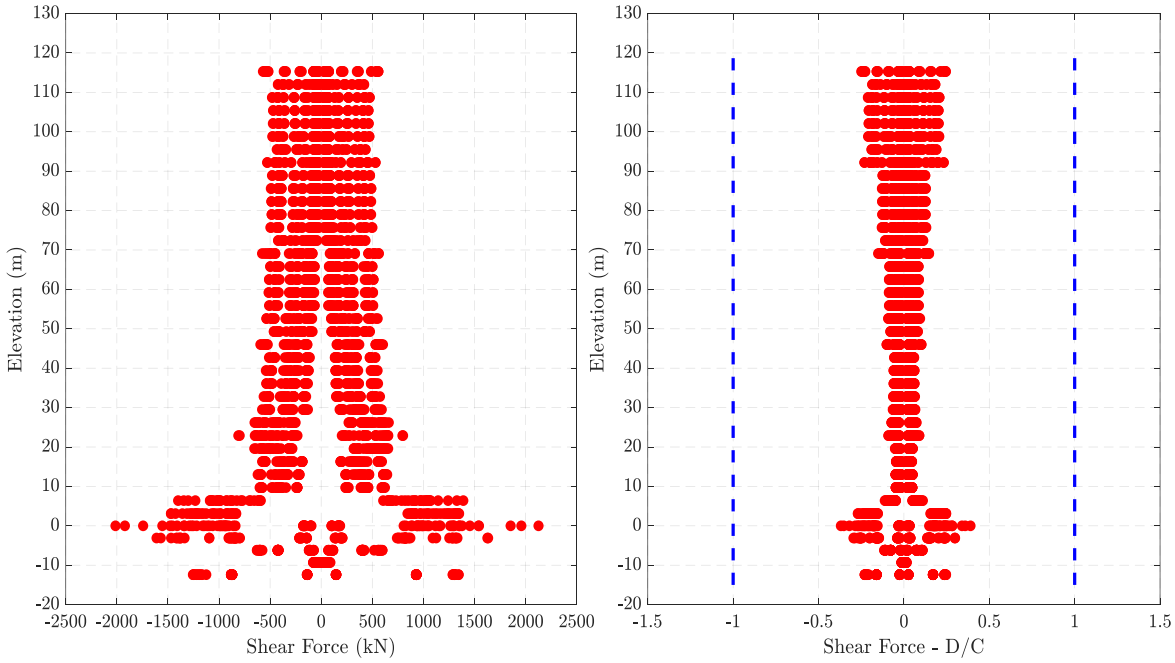

Figure 3.29. Column shear force (a) demands and (b) demand/capacity ratios.

The average plastic rotation demands of 22 analyses in coupling beams reached the capacity (almost 0.050 rad) at the middle floors but failed to exceed the limit. Revision of reinforcement detailing by increasing confinement can decrease the demand/capacity ratios. However, the objective of the tall building modeling is to provide reference IDR values that

can be imposed on door systems. The design fulfilled the code requirements without revisions.

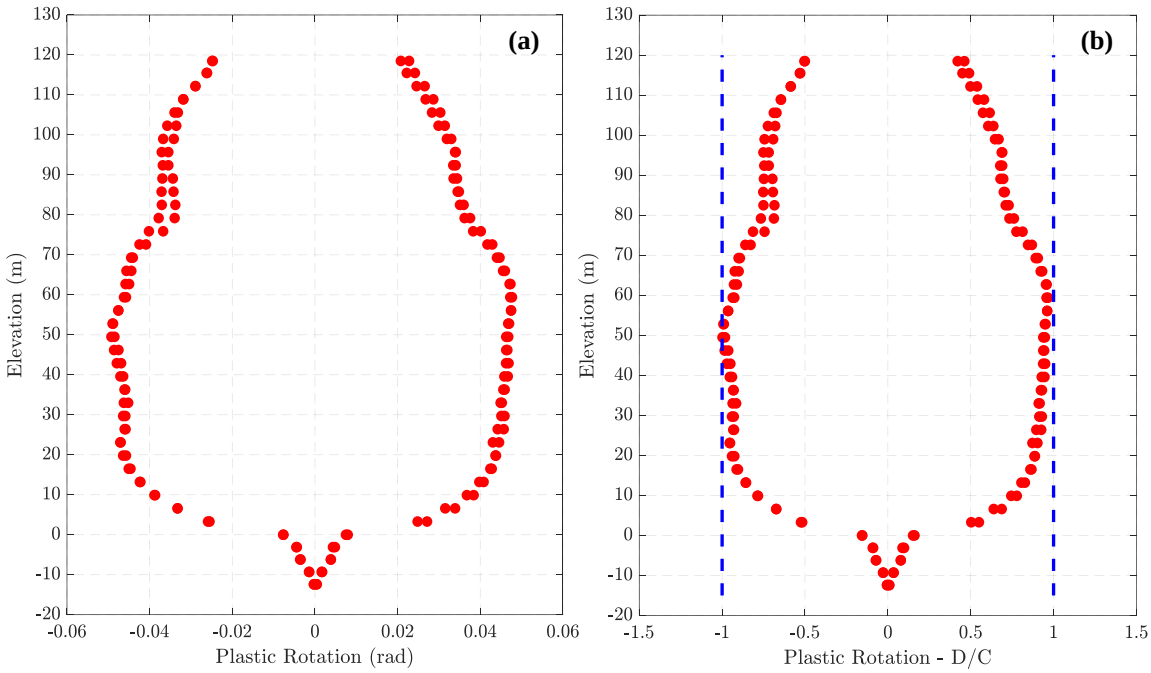

Figure 3.30. Coupling beam plastic rotation (a) demands and (b) demand/capacity ratios.

IDRs obtained for all eleven analyses in both X and Y directions at the specified 25 points on the typical floor plan presented in Figure 3.31 were recorded. Following TBSC [74] Section 13.6.5.2. IDRs measured at all locations in both perpendicular directions of the structure satisfied the mean IDR (3%) and maximum IDR (4.5%) for individual ground motion. Figure 3.32 shows the IDRs obtained at the midpoint of the building model under the 22 DD-1 level ground motions, while Figure 3.33 shows the maximum IDRs obtained from all specified points, regardless of the loading direction, under the DD-1 and DD-2 level ground motions.

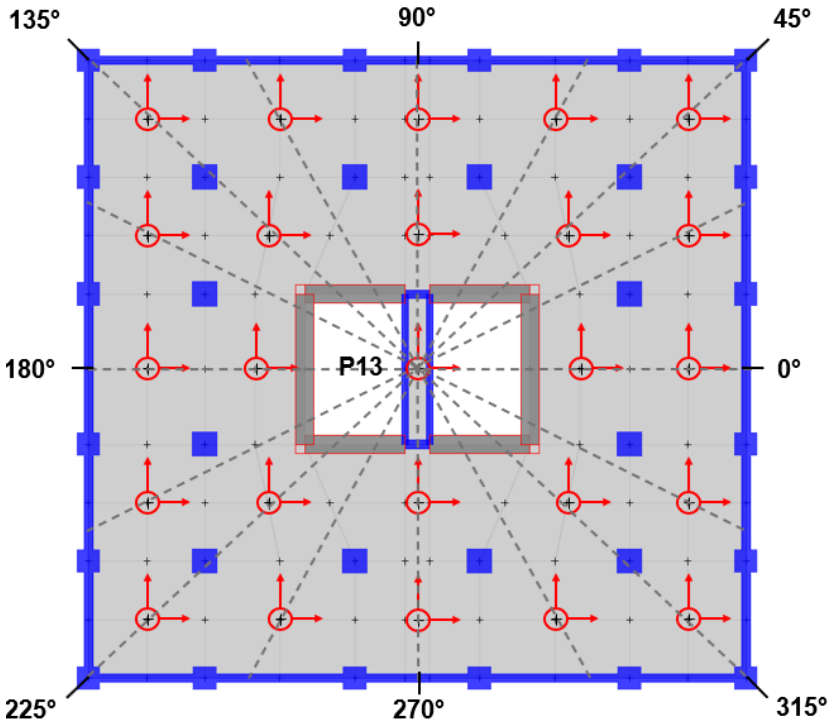

Figure 3.31. The locations where IDRs are measured on the typical floor plan.

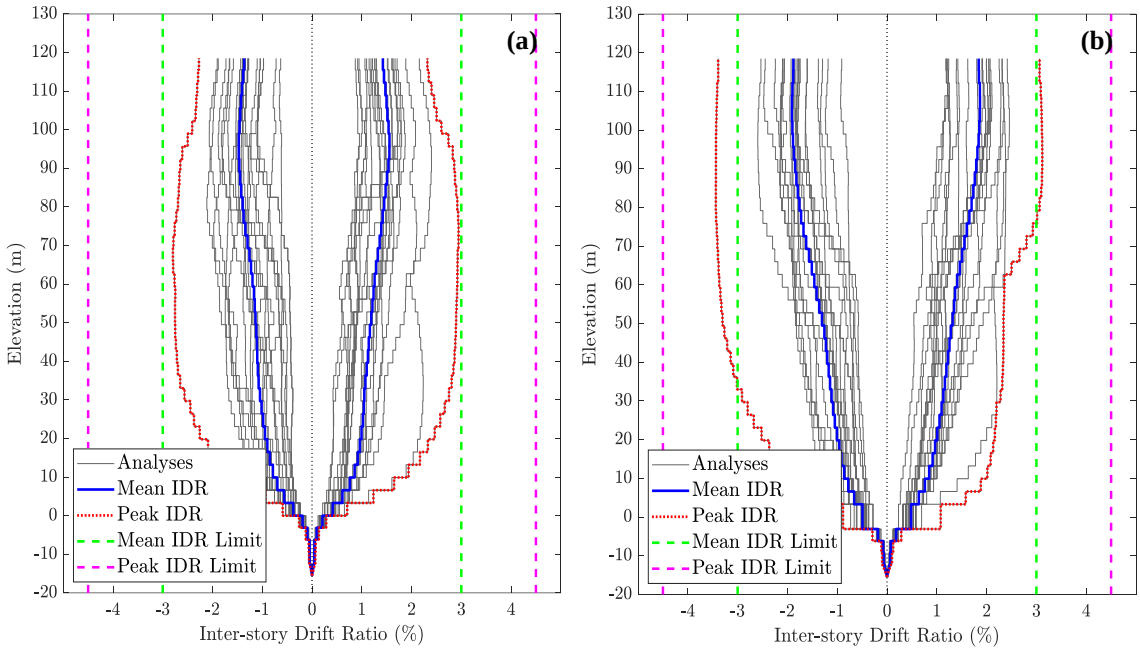

Figure 3.32. IDRs recorded at the middle (P13) of the building model for the X direction and (b) the Y direction of loading of DD-1 level ground motions.

The peak IDRs for the DD-1 and DD-2 ground motion intensity levels are obtained as 3.56% at the 34th story and 2.37% at the 30th story, respectively as shown in Figure 3.33.

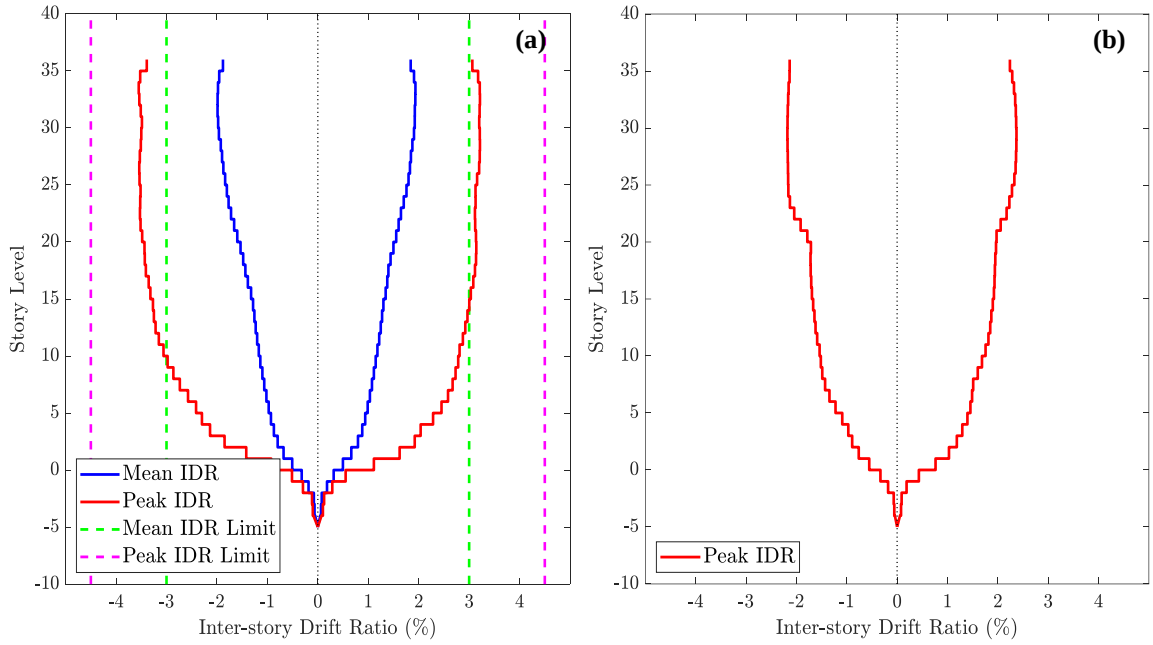

Figure 3.33. Vertical distribution of the peak IDRs for the entire building model under (a) DD-1 and (b) DD-2 level ground motions regardless of the loading direction.

The planar variation of IDR results obtained under the loading with the seismic incidence angles of $\theta_1 = 0°$ (X direction) and $\theta_2 = 90°$ (Y direction) is shown in Figure 3.34. Since the building has a regular structural plan, the distribution of maximum IDRs is close to uniform on the floor area.

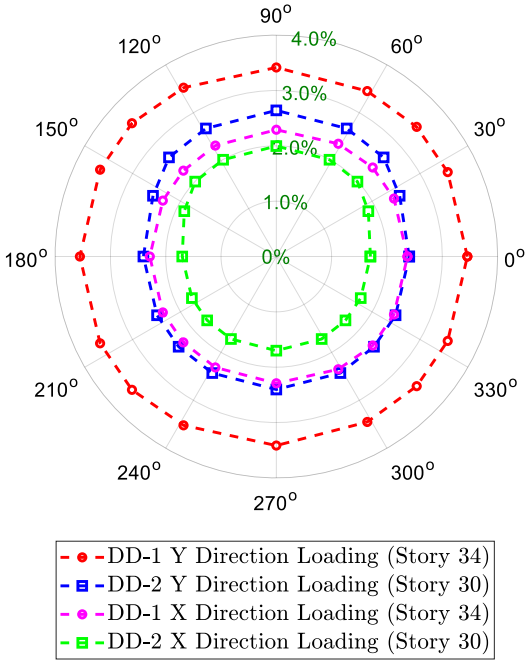

Figure 3.34. Planar distribution of the peak IDRs at the specified story levels obtained under 11-analysis for each direction of loading.

In a comprehensive effort to interpret the IDR results, they are converted to a frequency chart as shown in Figure 3.35. For DD-2 level ground motions, only 1% of all IDR measurements for the building model exceeded 2% drift level. For DD-1 level ground motions, 11% of all IDR measurements exceeded 2% drift level.

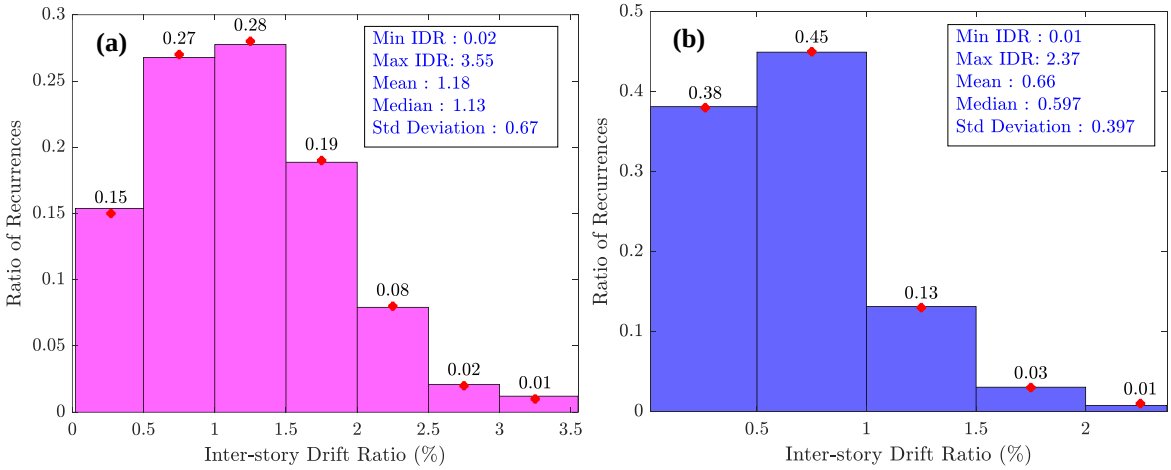

Figure 3.35. The ratio of recurrences of IDR results (regardless of the loading direction) at the specified 25 points for each floor obtained by NLTHA under (a) DD-1 and (b) DD-2 level ground motions.

4. FIRE DOOR TESTS

4.1. Earthquake Simulation Experiments

An analytical nonlinear structural model was created to precisely estimate the displacement demands on fire doors in tall buildings under seismic excitations and then these values were adapted for laboratory inquiry. It was decided to determine a demand parameter that properly correlates with damage levels under seismic excitations. Among all the displacement-related parameters, inter-story drift (the amount of relative deflection between two consecutive floors) is considered a significant cause that leads to the damage of buildings when subjected to earthquake ground motion [48, 49].

Drift-sensitive NCSs [29], if they are light and anchored, are primarily susceptible to displacement effects that they can move or swing by large amounts in translation and rotation under elastic or inelastic deformations of structural elements interacted with them during the response to earthquake shaking [27, 40]. To quantify the deformations on the fire doors during experiments, IDRs as response parameter at specified locations on the floor plan were obtained by NLTHA of the building model.

The damage state of a fire door is defined by the static cyclic loading and a deformation demand parameter is obtained as the drift ratio. Each fire door as shown in Figure 4.1 is certified with 120-minute-rated for integrity (E) and 90-minute-rated for insulation (EI_2). The leaf is covered by steel plates at both sides with gypsum board, stone wool, and ceramic fiber blanket insulation. The leaf is reinforced with a box-shaped steel profile. The entire double rebate door frame and the panel of the door leaf are made of 2 mm and 1.2 mm thick cold-rolled steel sheets, respectively. The door frame has 1170 mm width and 2400 mm height, while the door leaf has a thickness of 62 mm. The door set has no self-closing (C) features. The seismic tests of the fire doors were performed at the Bogazici University Structures Laboratory. The proposed seismic testing for each fire door is given in Table 4.1.

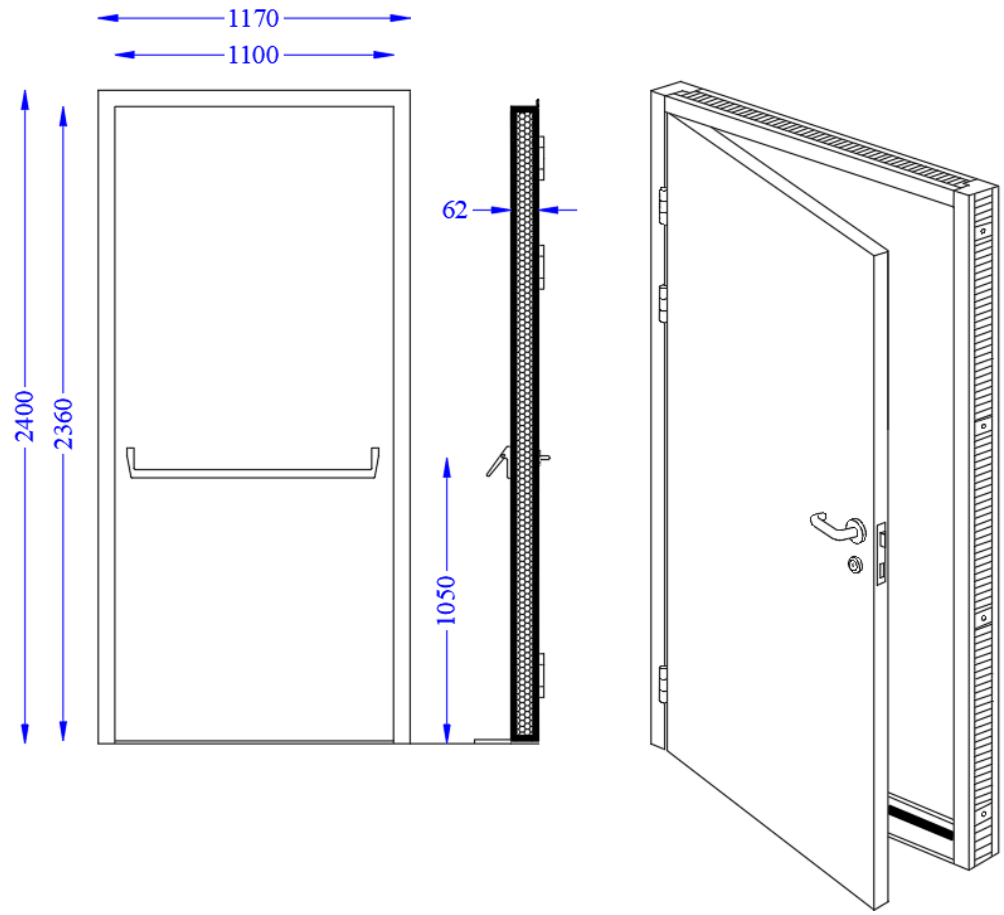

Figure 4.1. Construction details and dimensions (mm) of the fire door specimen.

Table 4.1. Details about the fire door specimens and proposed seismic tests.

Door Label	Door Description	Seismic Test
Door 1	Single-swing hollow metal door with a hollow metal frame (1170 x 2400 mm)	Static Loading
Door 2		Quasi-static Cyclic Loading-1
Door 3		Quasi-static Cyclic Loading-2
Door 4		Quasi-static Cyclic Loading-3
Control Door		N/A

In both in-plane static and quasi-static cyclic loading tests, a load cell was attached to the hydraulic jack to monitor the load. Hold-down connectors were used at each bottom corner to minimize the uplift and rocking of the fire door. The fire door deflection was measured by a main potentiometric linear transducer on the top plate and five other deflection potentiometers were used to apply corrections for the uplift in the lower right and left ends, the horizontal displacements in the lower right and left ends and the bottom slip. The test specimens are bolted to the loading beam and centered with sliding arms supported

by rigid columns at the top to prevent out-of-plane movement during loading and unloading (See Figure 4.2). The anchor holes drilled on the door frame were filled with fire-resisting material prior to FRR testing.

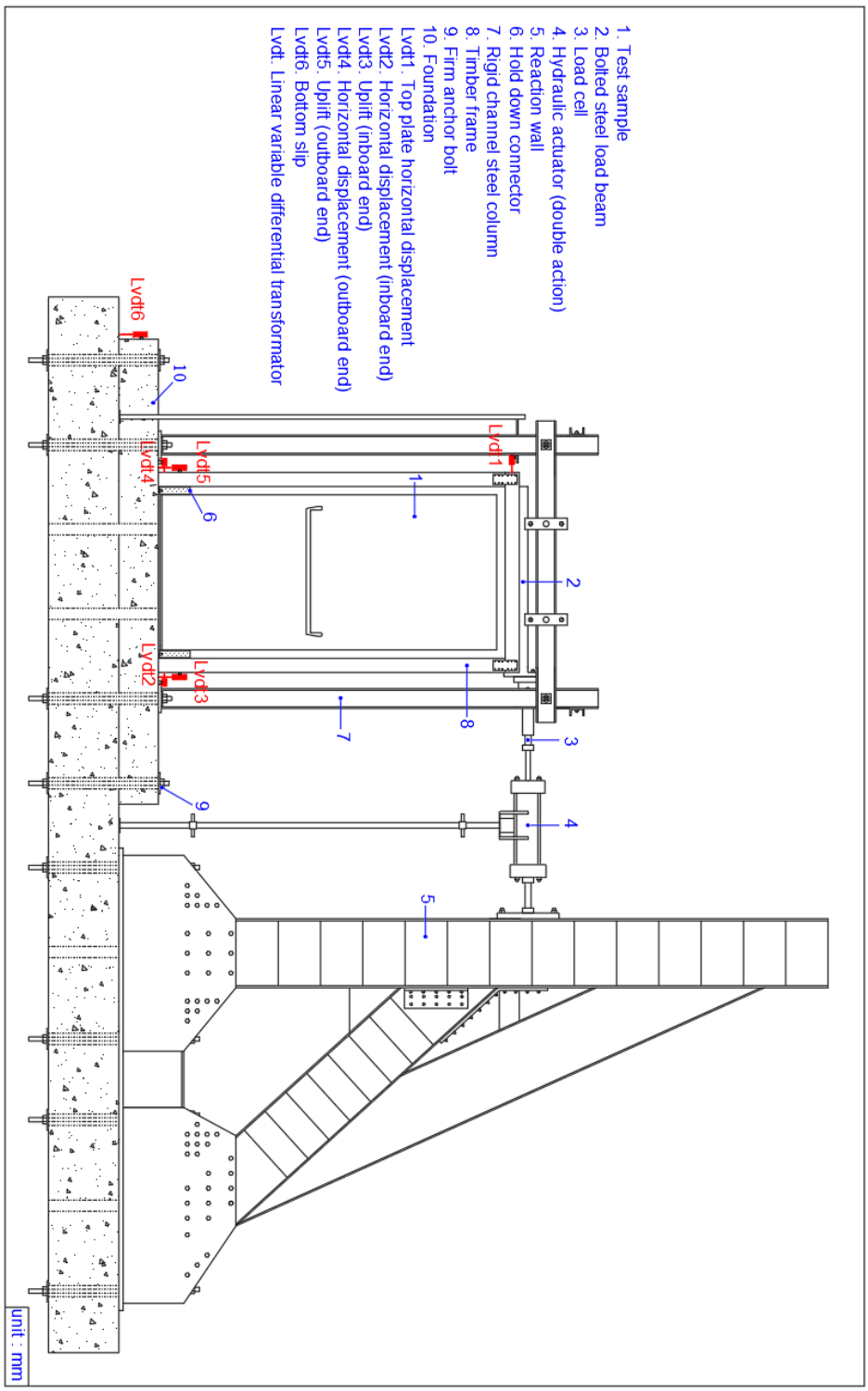

Figure 4.2. Test setup for both static and quasi-static reversed cyclic loadings.

4.1.1. Static Load Test

In order to thoroughly evaluate the seismic performance of full-scale drift-sensitive NCSs under realistic simulations independent of earthquake records, it is necessary to choose a suitable testing protocol that allows for the relationship between damage levels and deformation demands. For the static loading, the ASTM E564 [4] protocol, which is primarily used for static load testing for shear resistance of framed walls in buildings is utilized for Door 1.

Table 4.2. ASTM E564 one-way static cyclic loading procedure.

Step #	Stage	Loading Rate (mm/s)	Drift Ratio (%)
1	10% of peak (7.20 mm) – 5 min	0.024	0.3
	Load remained – 5 min		
	Load removed		
	Wait-time for the next step – 5 min		
2	1/3 of peak (24.00 mm) – 5 min	0.080	1
	Load remained – 5 min		
	Load removed		
	Wait-time for the next step – 5 min		
3	2/3 of peak (48.00 mm) – 5 min	0.160	2
	Load remained – 5 min		
	Load removed		
	Wait-time for the next step – 5 min		
4	Load to failure (72.00 mm) – 5 min	0.240	3
	Load remained – 5 min		
	Load removed		

The fire door is deformed by displacing the top of the specimen monotonically at a constant displacement rate for each step such that the ultimate displacement is achieved in no less than 5 min. The ultimate displacement is estimated as the value that corresponds to a 3% drift ratio. A multi-step loading history is shown in Table 4.2. At the first step, a preload of approximately 10% of the estimated ultimate displacement is applied with the loading rate of 0.024 m/s, and this load is held constant for 5 min before it is completely removed. A waiting time of 5 min is applied between each step. 1/3 and 2/3 of the ultimate displacements are reached at the second and third steps, respectively. The specimen is loaded and unloaded in this manner up to a 3% drift ratio.

In the 3rd step of the static loading, there is a sudden drop in the load value from 5.2 kN to 2.6 kN, indicating a reduction of more than 20% of the peak load (See Figure 4.3 and Figure 4.4). This failure coincided with the opening of the door leaf. Since the door frame could not resist the applied load upon opening of the door leaf, the drift ratio level caused disengagement of the door leaf from the door lock was considered as a damage state. However, to be able to interpret the seismic performance of the fire door at higher drift demands, Door 1 was subjected to further loading even though the damage state was obtained previously.

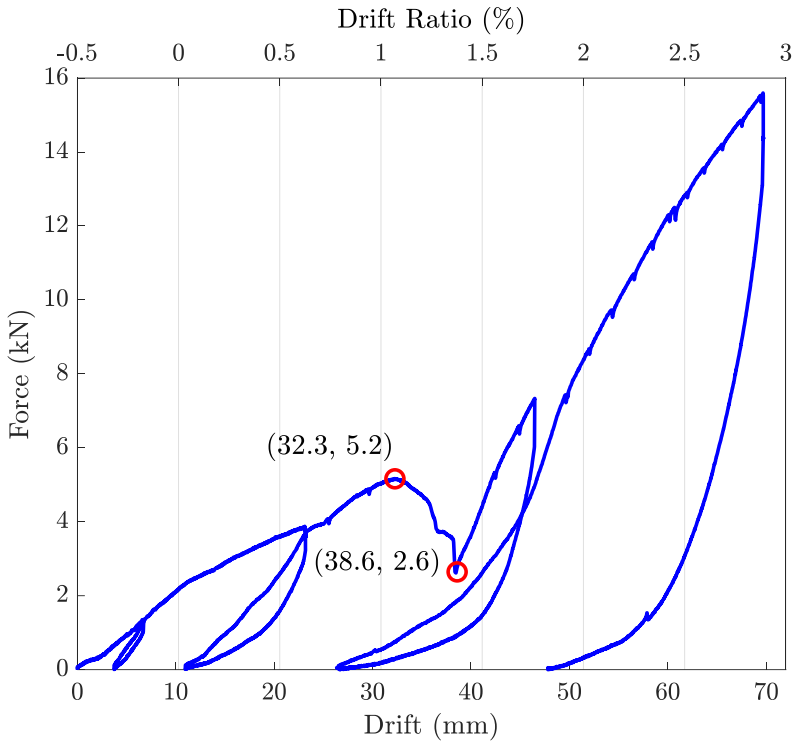

Figure 4.3. Force-drift relationship of Door 1 obtained under the static cyclic loading.

A dramatic increase in the resistance of the door set was observed when the bottom right corner of the door leaf contacted the concrete block underneath. It was predicted before the experiment that such a scenario would arise, but it was not prevented to reflect real circumstances.

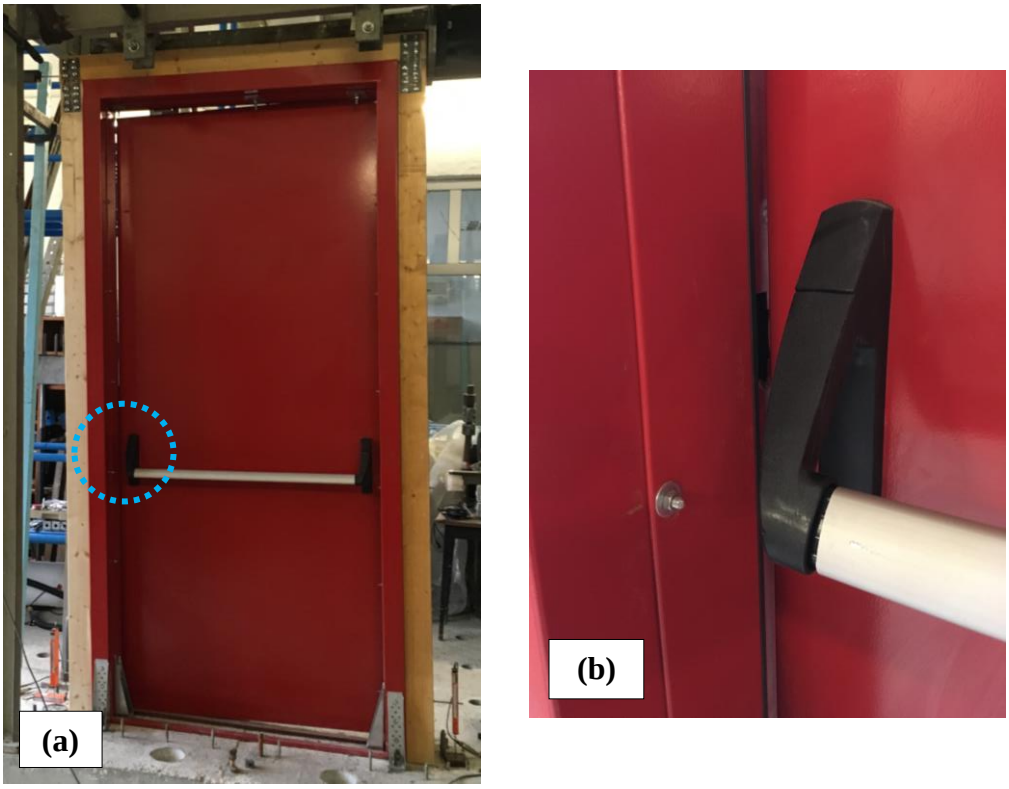

Figure 4.4. (a) Opening of the leaf of Door 1, (b) a closer view.

Damage to the fire doors is principally caused by the in-plane shear distortion, as represented by the IDR parameter. The damage state occurred at the relative displacement of 32.3 mm. With the door height of 2400 mm, this value corresponds to a 1.35% IDR. For the ultimate target displacement value in the subsequent three quasi-static cyclic loading tests, this IDR was taken as a reference.

4.1.2. Quasi-static Cyclic Load Tests

FEMA 461 [28] offers a displacement-controlled quasi-static loading protocol to assess the seismic performance of structural and nonstructural components and to quantify one or more damage levels with incremental displacement amplitudes. Two cycles per amplitude shall be completed as shown in Figure 4.5.

Table 4.3. FEMA 461 quasi-static cyclic loading protocol.

Step #	Drift (mm)	Loading Rate (mm/s)	Drift Ratio (%)
1	±1.6	0.026	0.07
2	±2.1	0.037	0.09
3	±3.1	0.051	0.13
4	±4.3	0.072	0.18
5	±6.0	0.100	0.25
6	±8.4	0.140	0.35
7	±11.8	0.196	0.49
8	±16.5	0.275	0.69
9	±23.1	0.385	0.96
10	±32.3	0.538	1.35
11	±42.0	0.700	1.75
12	±54.6	0.910	2.28
13	±71.0	1.183	2.96

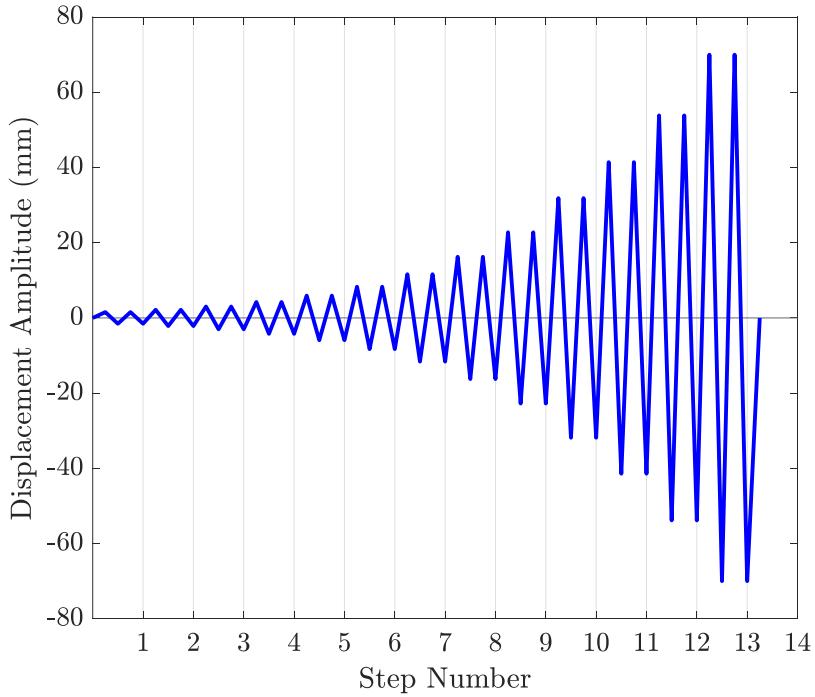

Figure 4.5. Quasi-static reversed cyclic displacement loading protocol by FEMA 461.

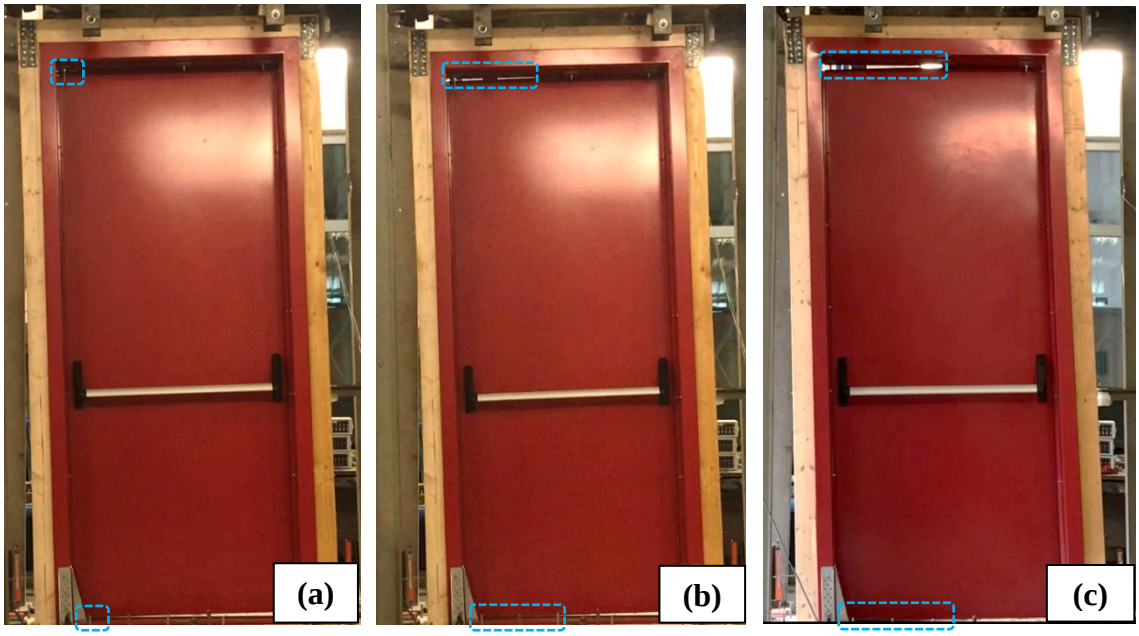

Figure 4.6. Deflected shapes of fire doors at the (a) IDR of 0.66% under the QSCL-1, (b) ultimate IDR of 2.28% under the QSCL-1, (c) ultimate IDR of 3.00% under the Static Loading.

Figure 4.6 demonstrates the expanded gaps between the door leaf and door frame at the top corners, as well as the rubbing of the door leaf against the concrete block underneath and the severe distortion of the door frame at different IDR levels. Here, 0.66% IDR represents the average IDR recorded on the floors of the building model under the design-level NLTHA. 2.28% IDR is the maximum IDR achieved by Door 2 upon failure, and 3.00% IDR is the ultimate loading level applied to Door 1 in the static load test.

During the quasi-static cyclic loadings, as the drift amplitude increased, the door resisted racking when the leaf contacted the frame, but the frame, in turn, was damaged by the door lock, tearing the frame's surface up to 20 mm (See Figure 4.7.a). The clearances between the leaf and the frame introduced flexibility to the relatively rigid leaf until the door lock began to tear the frame and eventually jammed with the frame. The movement of the leaf within the frame has the effect of distributing the load and damage more evenly over the door assembly. At greater drift amplitudes, the leaf and frame began to move not as individual parts of the door set but as one element. Hence, this prevented the door leaf to open.

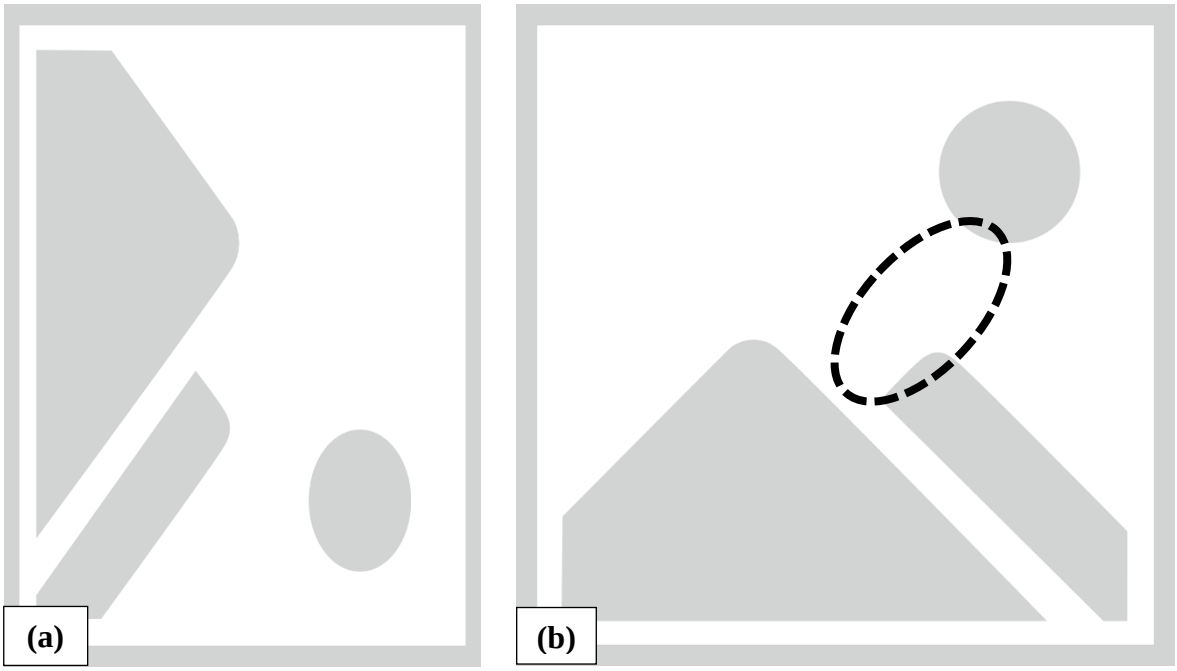

Figure 4.7. (a) The tear on the door frame caused by the door lock while pushing Door 2, (b) a slight door frame gapping on the interior top corner of Door 2.

The behavior of the fire door under cyclic loading, representative of the effects of a seismic event, was characterized by hysteretic loops with progressive degradation of strength and stiffness that eventually lead to failure. The shapes of hysteresis loops appear to be pinched in the middle. The physical reasoning behind this behavior is the softening of the connection points. As the loading was increased on the specimen, cracks propagate as seen on the top corner of the frame of Door 2 (See Figure 4.7.b).

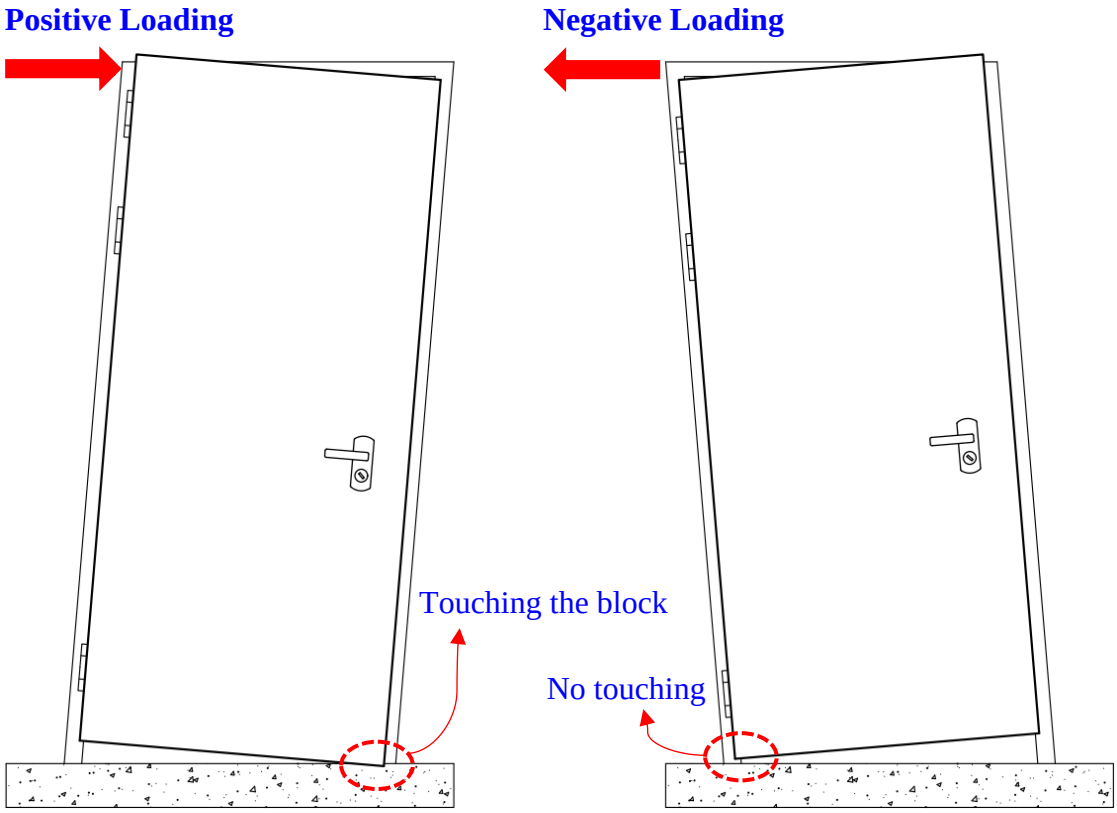

Figure 4.8. Fire door deflection mechanism under lateral loading.

The fire doors were hinged from their left sides only. When the actuator pulled the fire door, the door leaf's left end corner did not touch the concrete block underneath (See Figure 4.8). Due to hinges fixed to the door frame, the door leaf was unable to move further to the left. As a result, the peak load levels achieved with negative loading are lower than those obtained with positive loading. As shown in Figure 4.9 through Figure 4.11, this leads to asymmetric hysteresis behavior. The red circles in the plots show the peak load achieved before the failure and the load corresponding to more than a 20% decrease where the failure occurs. The failures of the specimens occurred at 2.28%, 1.90%, and 2.30% IDRs, respectively.

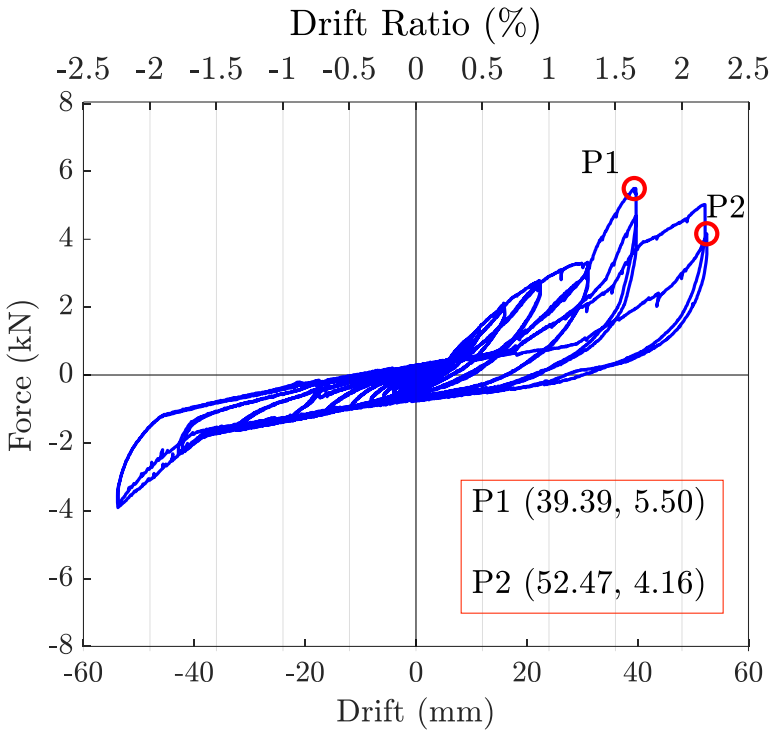

Figure 4.9. Recorded hysteresis curve for Door 2.

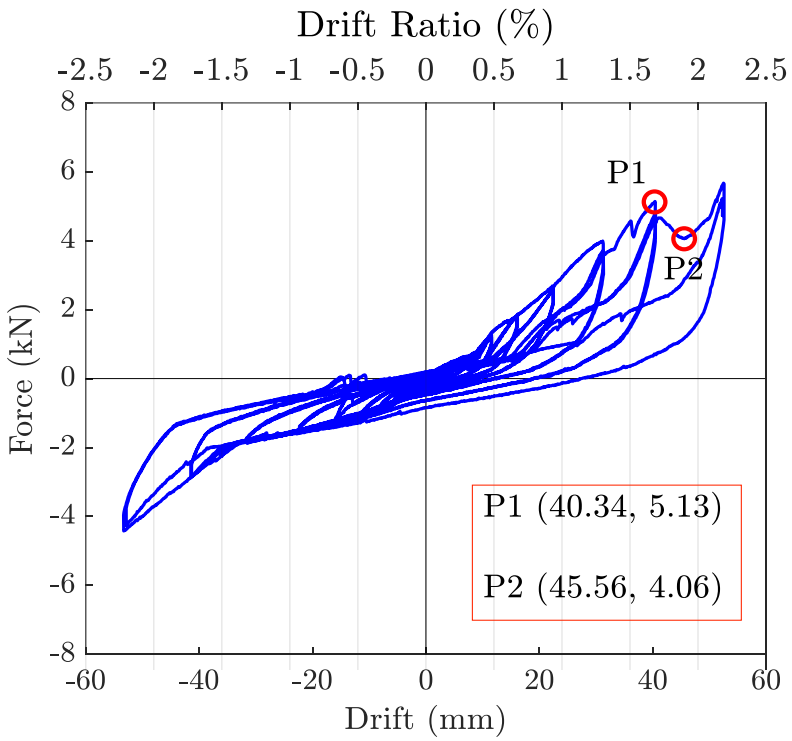

Figure 4.10. Recorded hysteresis curve for Door 3.

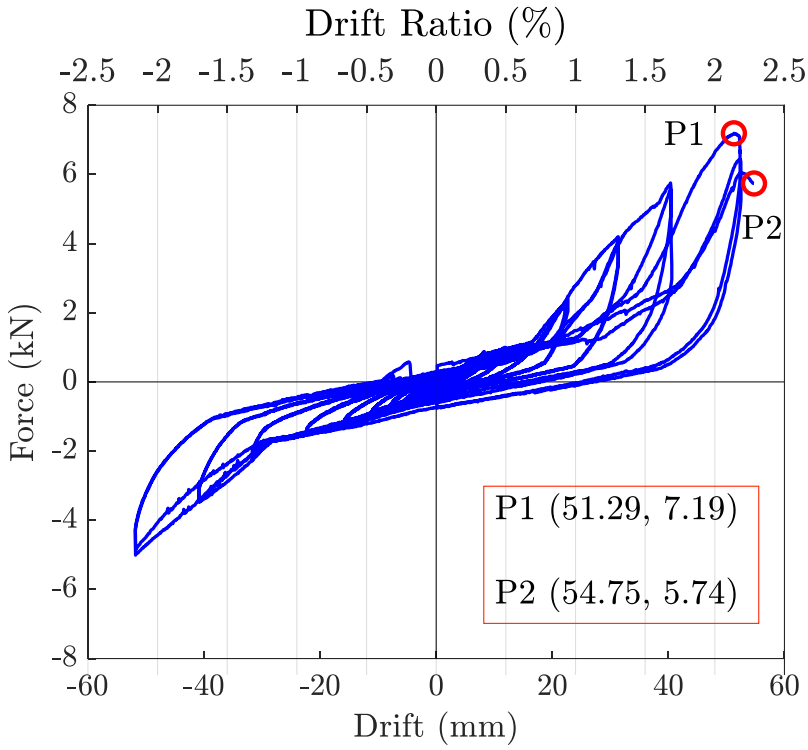

Figure 4.11. Recorded hysteresis curve for Door 4.

The enveloped curves are generated from the outer perimeter of the extremities of deflections and forces in the hysteresis plots to compare the pattern matching. Except for the divergence in the maximum load levels, especially for the positive loading range, the specimens demonstrated analogous hysteresis behavior and covered a similar amount of maximum energy for a cycle.

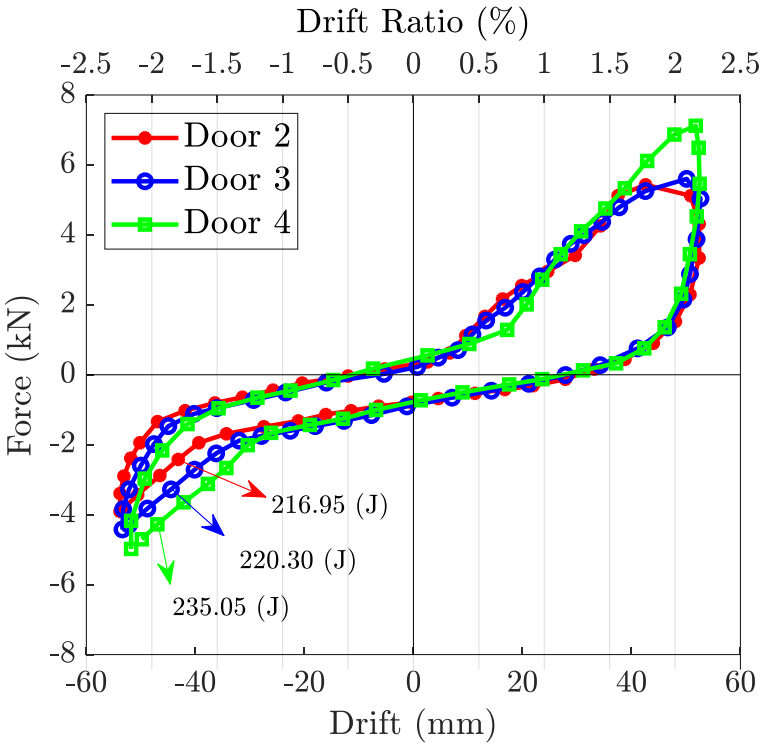

Figure 4.12. Comparing the enveloped hysteresis curves of each fire door subjected to the quasi-static cyclic loadings.

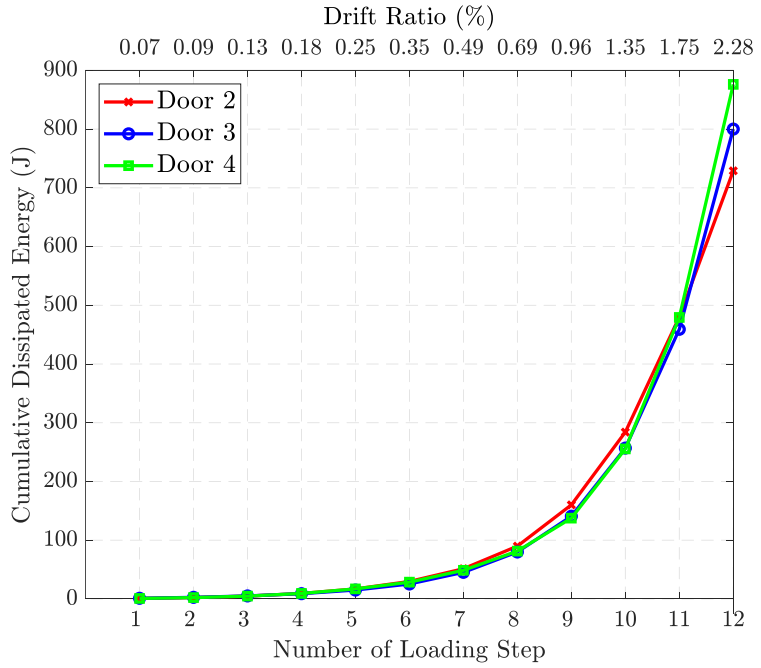

Figure 4.13. Comparing the cumulative hysteretic energy dissipated by the specimens at the end of each step.

More concisely, the correlation between the cumulative hysteretic energy dissipation paths drawn by each test sample is convincing when comparing their response to the simulated reversed cyclic loadings (See Figure 4.13). As the energy absorption amounts diverge at higher drift ratio levels, the paths evolve into a high-order nonlinear curve.

Sequential behavior of the specimens for each loading cycle was monitored, and the common visual observations were reported during the quasi-static cyclic tests (See Table 4.4). The findings allow the assessment of the scale of seismic damages to a fire door assembly.

Table 4.4. Common damage modes observed at the associated IDRs in each quasi-static cyclic test.

Step #	**Drift (mm)**	**Drift Ratio (%)**	**Damage State Description**
1	±1.6	0.07	No damage
2	±2.1	0.09	No damage
3	±3.1	0.13	Slight spacing between the door leaf and door frame
4	±4.3	0.18	Minor in-plane rotation of the door leaf within the door frame
5	±6.0	0.25	Jamming of the door leaf / Misalignment of the door frame
6	±8.4	0.35	Beginning of the tearing on the door frame by the door lock
7	±11.8	0.49	Door leaf's bottom corner touches the concrete foundation underneath / Door leaf and door frame move as a unit
8	±16.5	0.69	Door frame and door hinge loosening / Door frame gapping at the top corners / Door leaf's bottom corner rubs the concrete foundation
9	±23.1	0.96	Excessive spacing between the door leaf and door frame / Significant in-plane rotation of the door leaf within the door frame / Clear view of the distorted geometry of the door frame to a parallelogram
10	±32.3	1.35	Visible crack propagations on the door frame's top corners
11	±42.0	1.75	Door frame severe distortion / Local buckling on the door frame
12	±54.6	2.28	Residual drifts in the door assembly / Permanent, visible cracks at the door frame's top corners / ≈ 20 mm tearing on the door frame by the door lock

4.1.3. Limitations in the Seismic Testing Setup

- *Fire Door-Partition Wall Interaction:*

Fire doors are mounted in partition walls in practice, and hence additional stiffness is provided by surrounding walls under seismic action. Although the door set and the wall interact, seismic excitations can lead the wall to move with structural elements, dissipating substantial earthquake-induced damages before being experienced by the door assembly. When the door set is excited by inter-story movements, partition walls can be damaged again where the door frame meets the upper corners. Increased movement of the door frame, greater than clearances around the leaf, is more likely to result in additional cracking and displacement of the partition wall. To reflect the real boundary conditions of fire doors, the most feasible and cost-effective technique (timber frame encasement) available within the funding package was applied at the laboratory.

- *Boundaries of the Fire Door/Timber Frame Encasement:*

Rather than building a wall around the fire door specimens, as a practical approach, cross-laminated carbonized bamboo lumbers were assembled to the fire doors via screws at 5-point on the side frames and 3-point on the top frame to avoid applying displacement demands directly to the fire door set. However, it was not investigated quantitively how much the timber frame contributed to the strength of the fire door specimen against the seismic displacement effects.

- *Out-of-plane Loading Effect:*

The combined in-plane and out-of-plane seismic excitation of partition wall systems is one of the complicated yet insufficiently studied areas in the seismic vulnerability assessment. Although seismic waves propagate in 3D, we are particularly examining the drift effects on the fire doors assemblies in only one horizontal direction, as is customary, neglecting the vertical and the other horizontal components of an earthquake. While the door set is subjected to racking shear in its

loading plane, the extent of the damage may increase significantly by adding out-of-plane bending and implicitly the tension effects.

4.2. Fire-resistance Rating Experiments

The fire doors include intumescent seals in the frame designed to expand on heating and restrict the flow of hot gases from the allowed clearances for a sufficient period to permit the required fire resistance to be achieved. The measurement of the clearances was taken just before the FRR tests. The locations of the measurement points are shown in Figure 4.14.

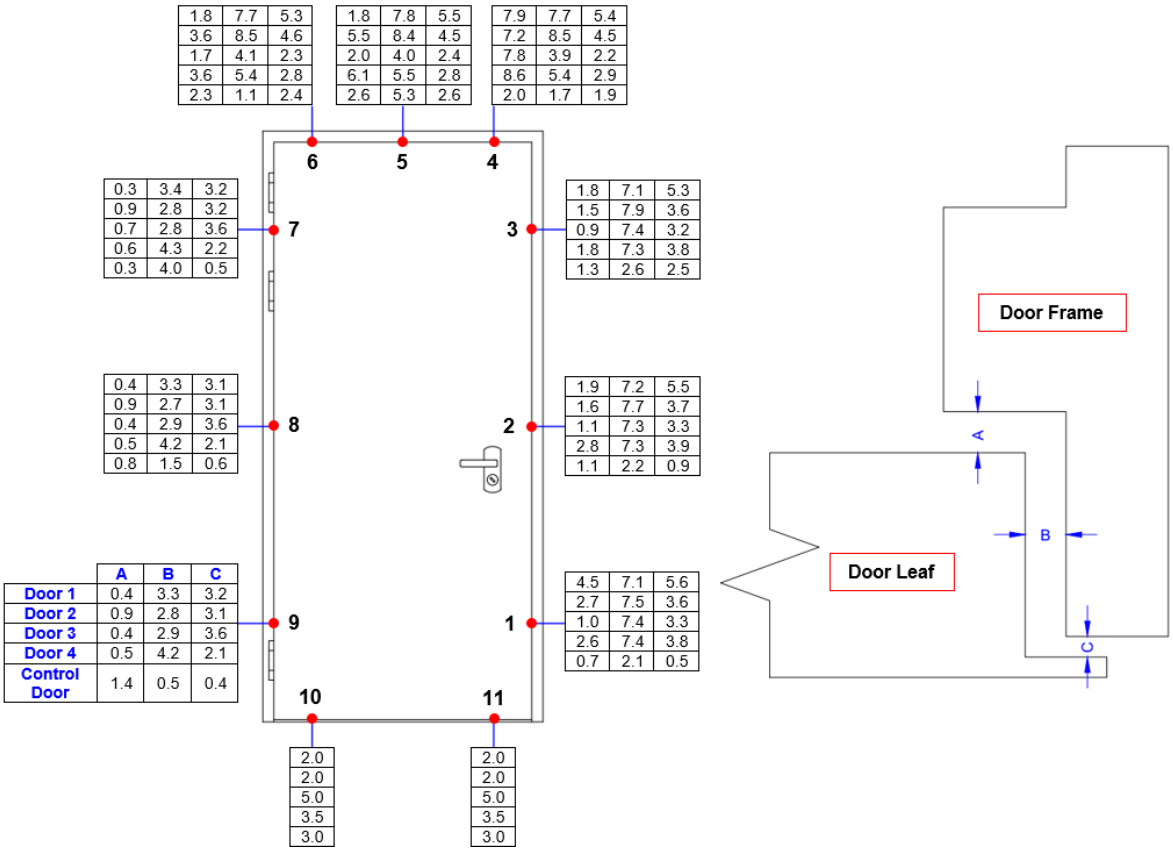

Figure 4.14. Door leaf/frame bottom, top and side gaps measurements (mm) taken just before the fire-resistance rating tests.

Under the seismic drift demands resisted by each door assembly, the clearances between the door leaf and door frame widened further along the door lock side than the hinged side, as seen in Figure 4.14. Although the gap measurements on the hinged side of each specimen are relatively close to the clearances for the Control Door, the gap sizes on the top edges of the doors considerably apart from the recorded spaces for the Control Door.

As per the measurements at point 4, the region that experienced the largest gap change between the door leaf and frame is the top right corner of each damaged door set.

The size of the gaps around the perimeter of these swinging doors affects fire growth by heat transfer and smoke flow through these enlarged spaces. As these excessive gaps surpass the limits given in EN 1634-1 [24], they are also likely to lead to the Integrity (E) failure to be reached in a short time. As per EN 1634-1, the maximum clearances between the fixed and moveable parts shall not exceed 25mm at the sill or 6 mm at 150 mm intervals elsewhere.

The classification of fire resistance of fire doors in terms of time rating shall be determined based on the time-temperature curves and visual observations in accordance with EN 1634-1. The devices used in the tests shall provide the provisions of EN 1363-1 [23]. Each of these parts must show a certain thermal and mechanical stability summarized as the integrity criterion (E) and the insulation criterion (I**)** to provide complementary functionalities [23, 24]. In the scope of the fire-resistance rating tests conducted, the following failures were monitored and assessed:

- Fire Integrity (E) failure: A sustained flaming for more than 10s on the unexposed side occurs. It is also characterized by the formations of cracks, gaps, and fissures, or ignition (by glowing or flaming) of a cotton pad held on the unexposed fire door surface.

- Fire Insulation (I_1 and I_2) failure: The temperature of any insulated individual metal thermocouple attached to the unexposed face of the test specimen increases by more than 180°C (the limit for I_1) and 360°C (the limit for I_2) above the initial temperature, or the average temperature rise of a group of thermocouples exceeds 140°C above the initial average temperature.

The FRR tests were conducted at the Construction Materials Fire and Acoustic Laboratory of Turkish Standards Institution (TSE). The masonry supporting construction in which fire doors are mounted is supplied by the test laboratory and consisted of aerated concrete blocks which have a density of 450 kg/m^3 and a thickness of 200 mm.

The heating of the test samples was carried out according to the Standard ISO 834-1 [37] fire curve. This relationship is the model of a fully developed fire in a room and is described with Equation (4.1) as follows:

$$T(t) = 345 \log10 (8t + 1) + 20 \cdot \quad (4.1)$$

The thermocouples were intended to measure the temperature rises on the surface of the leaf and frame of the earthquake-damaged fire door set as demonstrated in Figure 4.15. Thermocouples from TC1 to TC5 on the unexposed surface of the door leaf are used to collect the mean and maximum temperatures, whereas the thermocouples from TC6 to TC17 monitored the maximum temperatures only, either on the edges of the door leaf or door frame.

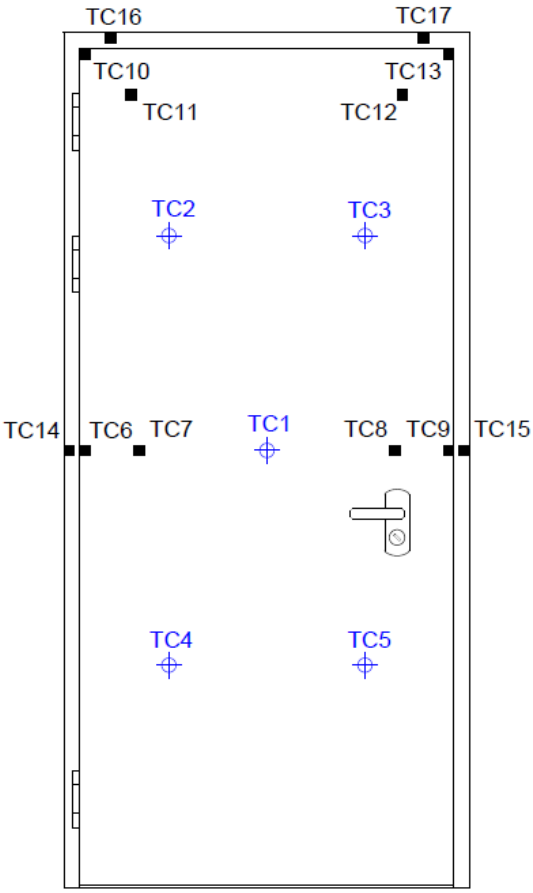

Figure 4.15. The layout of thermocouples on the unexposed fire door surface.

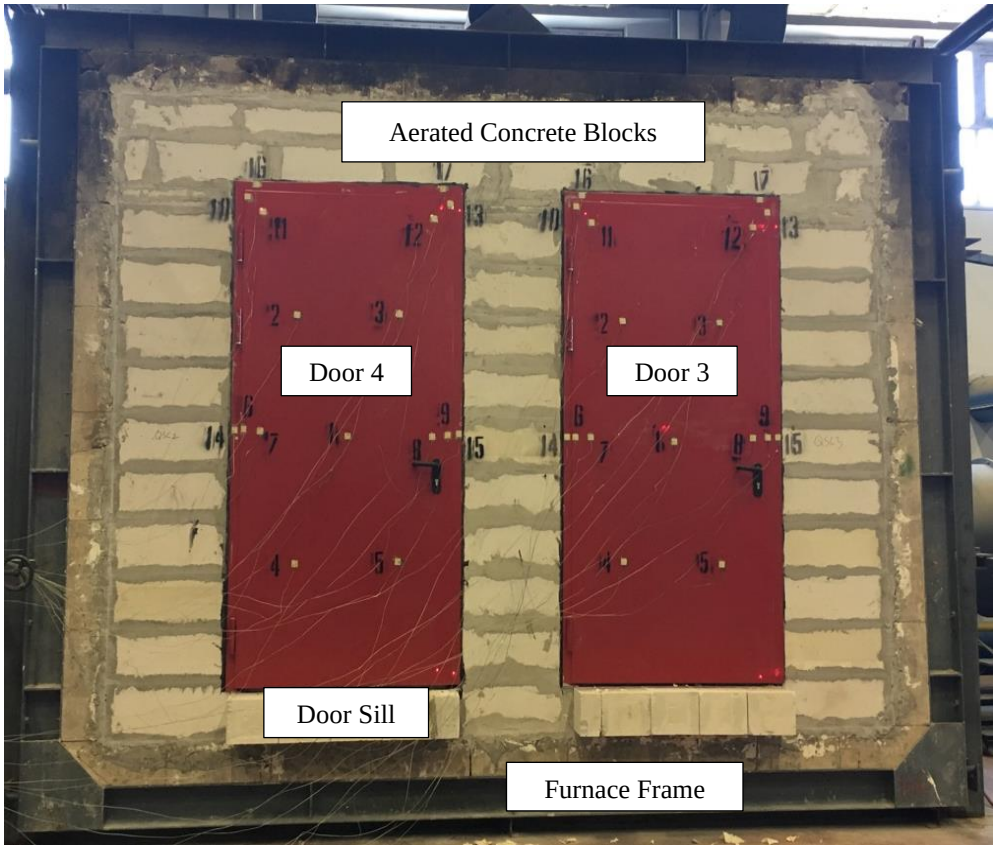

Figure 4.16. Fire-resistance rating test setup (unexposed sides of the test specimens).

To compare the reduction in the FRR performance of the earthquake-damaged fire doors with an undamaged fire door with the same construction details, a control specimen was also subjected to the FRR test. Two fire doors were mounted in each furnace test.

For FRR tests of Door 1 through 4, integrity failure occurred at about 30 minutes. Thermal bowing away from the fire at the top and bottom edges of the door leaves in a short time provided the means for the flow of flames and hot gasses from the furnace [24] and eventually caused the integrity failure by flaming and ignition of a cotton pad held on the top corner regions. The door frame behaved similarly, but because it was fixed to the supporting construction, it could not move as much as the door leaf. As Cheung et al. [14] found out, larger door openings showed less resistance to the spread of hot gases or smoke and allowed for higher temperatures to pass through the gaps.

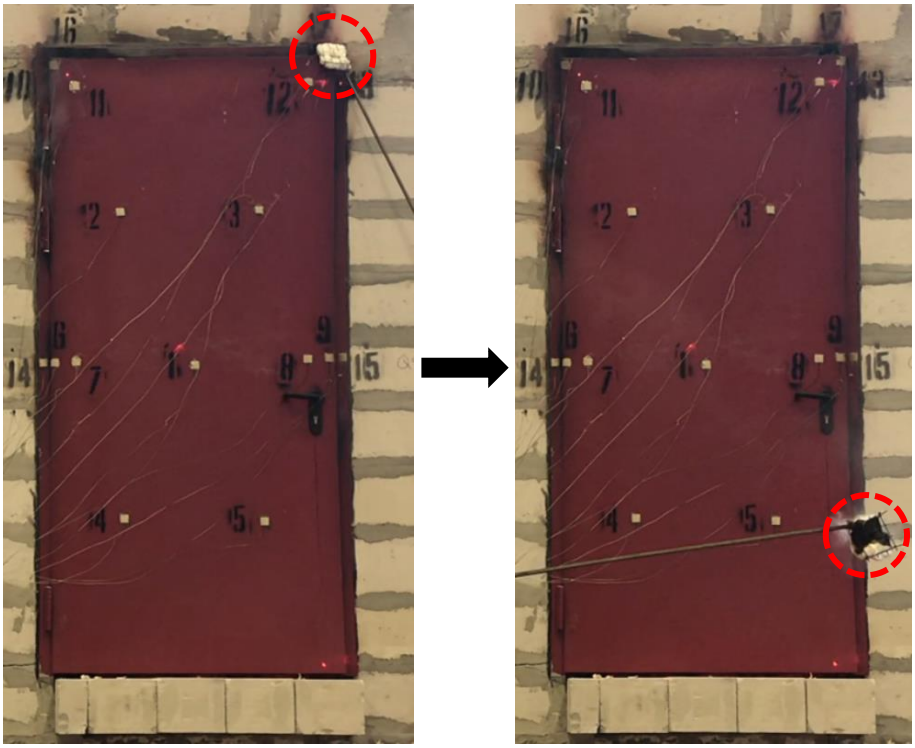

Figure 4.17. The ignition of a cotton pad held on the top right corner of Door 4 caused the integrity (E) failure at the 37th minute.

During all FRR tests, the fire insulation failure due to the mean temperature rise exceeding 140°C was not observed for any test specimens as seen in Figure 4.18. The main reason is that the door leaves had no physical damages during seismic testing, instead the door frames were distorted severely. Therefore, the excessive temperature rise on the central surfaces of the door leaves did not occur because the insulation material inside the door leaves had no previous damage before the FRR tests.

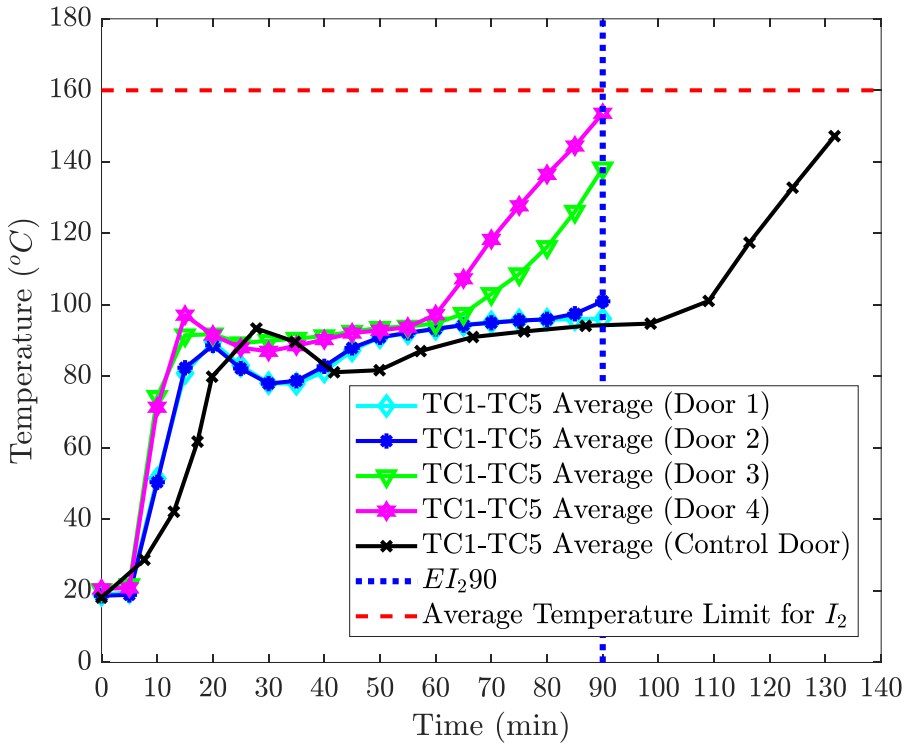

Figure 4.18. Average central surface temperatures (TC1-TC5) on the unexposed side of each fire door.

Even though the fire doors did not surpass the average temperature threshold for fire insulation, they failed the maximum temperature criterion because of excessive temperature rise on the door frames at around 40th minute. Figure 4.19 shows the critical surface temperature rise (TC17) that reached above 360°C on the door frames earlier than the TC15 on the Control Door's frame. Concerning the insulation criterion, a dramatic reduction in the fire rating is observed for the damaged fire doors having excessive gap measurements notably at the top right corner. The thermographic image (See Figure 4.20) confirms the temperature and smoke distribution around the perimeter of the fire door samples, noticeably the heat intensity around the corners.

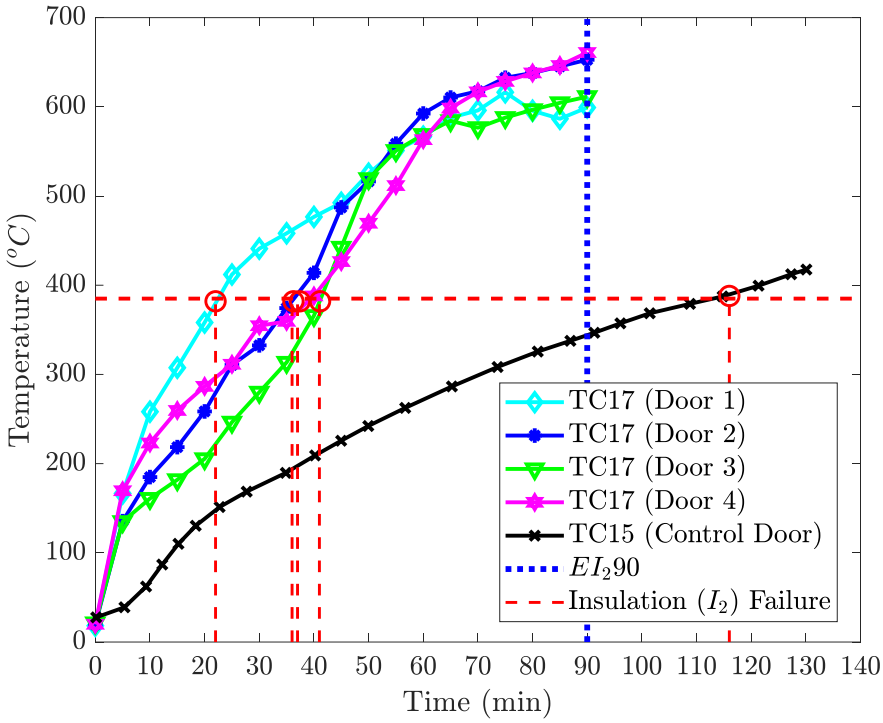

Figure 4.19. The critical surface temperatures caused the insulation (I_2) failure on the unexposed side of each fire door.

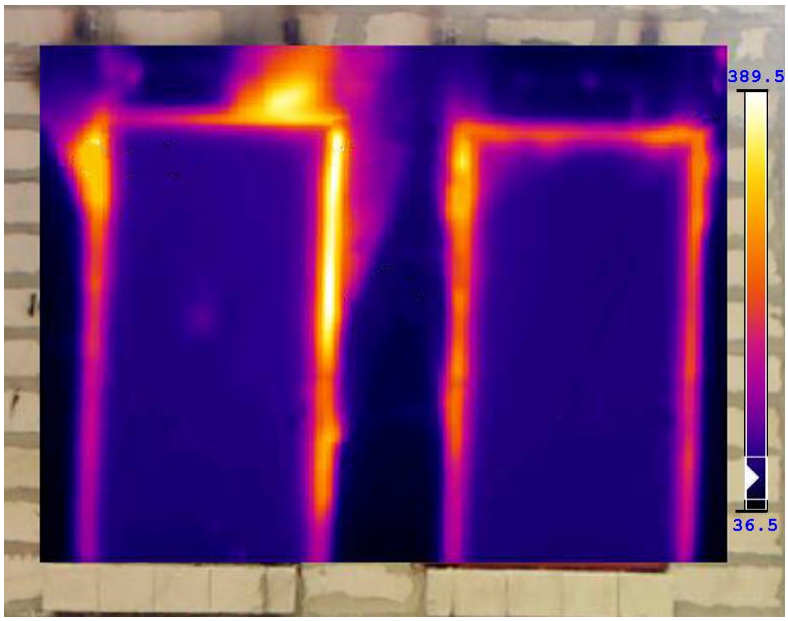

Figure 4.20. Thermographic camera image of the air leakage around the perimeter and temperature distribution over the unexposed sides of Door 4 (left) and Door 3 (right) at the 40th minute.

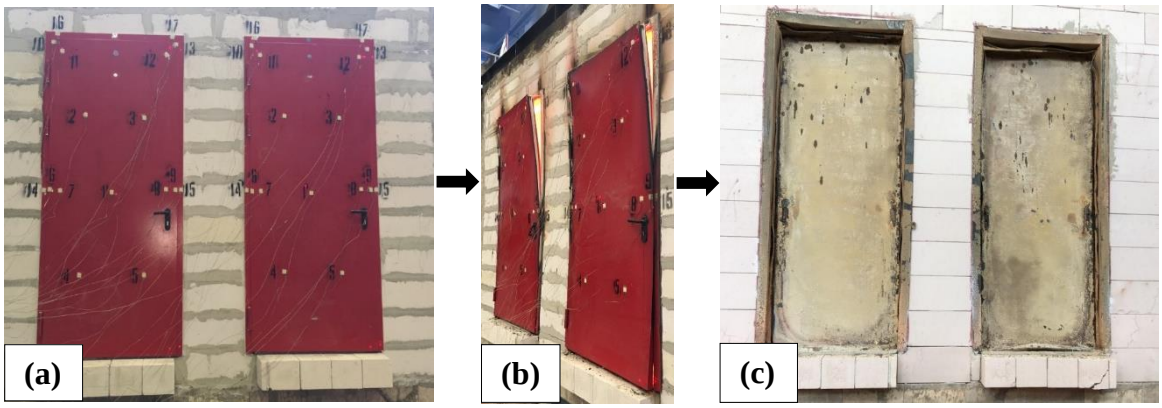

Figure 4.21. Door 4 (left) and Door 3 (right) (a) before FRR test, (b) during FRR test (unexposed side), (c) after FRR test (exposed side).

Table 4.5. Summary of the experimental results.

Door Label	**Seismic Testing**		**Fire Resistance Rating**			
	Test Name	*IDR at Ultimate (%)*	*Integrity, **E** (min)*	*Reduction in **E** (%)*	*Insulation, I_2 (min)*	*Reduction in I_2 (%)*
Door 1	ML	3.00	32	73	22 (TC17)	76
Door 2	QSCL	2.28	36	70	36 (TC17)	60
Door 3	QSCL	2.28	38	68	41 (TC17)	54
Door 4	QSCL	2.30	37	69	37 (TC17)	59
Control Door	N/A	N/A	No failure	N/A	116 (TC15)	N/A
The heating was terminated at 91st minute for Door Nr. 1 through Door Nr. 4, and at 132nd minute for the Control Door.						

5. CONCLUSIONS AND RECOMMENDATIONS

5.1. Overview

Post-earthquake fire is not considered as a specific loading case by most seismic design approaches; furthermore, a certain degree of damage in structural members is tolerated in structural design philosophies. As previous studies reported, seismic damage induced on fire protection systems may cause reductions in their fire resistance capacity and make them vulnerable to fire, thereby increasing the risks to the viability and property loss in case of an outbreak of fire spread.

Since the seismic response of PFP systems is poorly understood and the reduction in their fire resistance is similarly uncertain, the results of previous studies that tried to quantify and classify earthquake damages induced on PFP systems are highly variable. Previous research on fire protection partitions has suggested reductions in their FRR up to 50% when subjected to 0.6% IDR or less. The UCSD post-earthquake fire experiments on the floors with fire-rated doors did not quantify the extent of the damage to their FRR performance except stating that the fire-rated doors are nonfunctional after subsequent fire tests. As in the preceding earthquake experiments conducted to learn the seismic performance of fire-rated or non-fire-rated door systems, relatively severe damages occurred on the door frames (e.g., door frame gapping, loosening, severe distortion, or detachment) for a door assembly.

5.2. Conclusions

In this study, tested earthquake-damaged fire doors failed to satisfy the integrity and insulation criteria mainly due to previous earthquake-induced damages on the door frames. The fire doors subjected to 2.3% IDR prior to the FRR test experienced a reduction of 69 ± 1% in their fire integrity (E) and up to 60% reduction in their fire insulation (I_2) performance. When the IDR level goes up to 3%, as is the case for Door 1, the reduction in the FRR, especially for the fire insulation, is extensive (See Figure 5.1).

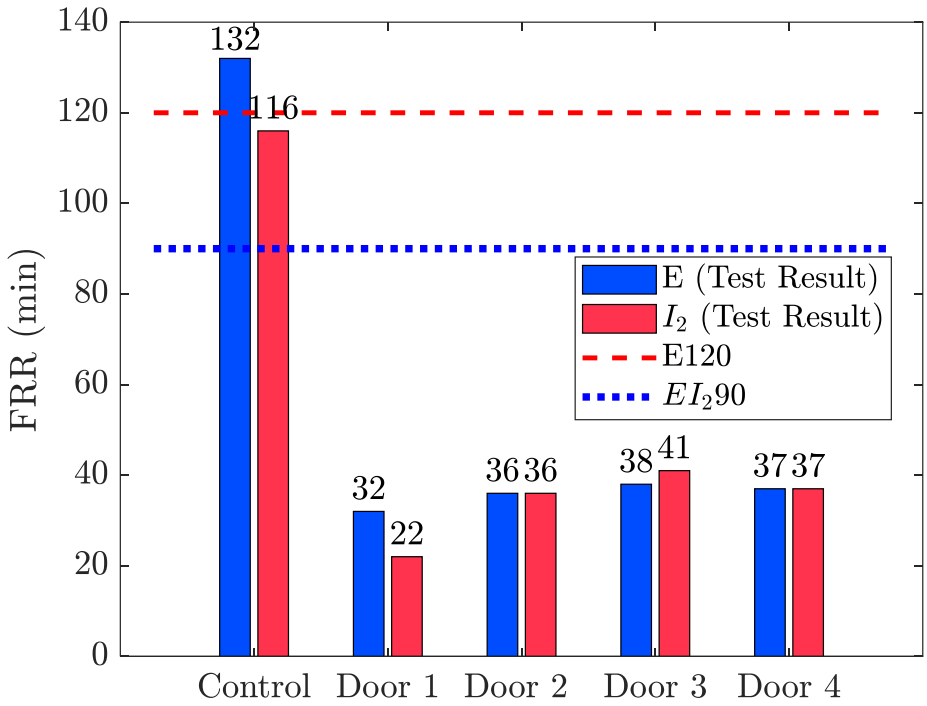

Figure 5.1. FRR test results for each specimen in terms of fire integrity (E) and fire insulation (I_2) performance.

The seismic drifts applied during the experiments caused the door frames to deform to a parallelogram, increasing the scale of the damage, notably at the corner regions. Therefore, the sensitivity of the fire integrity to widening of the gaps at these locations was dramatically affected, and hence, the fire integrity was impaired very soon. The intumescent seal was unlikely to expand sufficiently to fill these enlarged spaces.

The fire insulation performance of a steel fire door mainly depends on infill insulation with high strength and low thermal conductivity. Because the mean temperatures on the leaf surface did not exceed 140°C throughout each test, it is clear that the infill insulation material behaved properly. After the test was initiated, the high-temperature gases easily transferred to the unexposed side of the previously damaged specimens, which made the unexposed surface temperature of the door frames fail by insulation criteria in a short time.

The findings from both the quasi-static cyclic loading and fire-resistance rating experiments on the fire doors bear a close resemblance such that the seismic behavior and the FRR performance of these three test samples are consistent with each other. As the results

suggested, a fire door could be jammed or non-functional as the door frame could be distorted and the door lock could be damaged during a seismic action, and its FRR performance is expected to be below specification after a design level earthquake even the building itself is structurally sound.

When fire doors are subjected to higher drift demands in case of a design-level earthquake, it may not be possible to restore their initial fire performance as it is concluded that the remaining fire resistance is nearly one-third of their certified value. Thus, it is recommended to replace severely damaged fire doors instead of repairing them. However, the complete replacement of damaged fire doors can be costly. In line with previous experimental results, the level of damage on a door system is amplified by the distortion of the door frame, and the door leaf is hardly damaged except for the door latch failure. This allows protecting the fire door leaf's geometry while avoiding damage to the insulation material inside. Therefore, only the replacement of the door frame can be recommended even for severely damaged fire door systems such as those observed in this study. However, more fire door specimens subjected to varying levels of IDR should be tested for fire resistance to confidently classify at which level of drift to restore or replace the door frame.

5.3. Recommendations for Future Studies

This experimental program was undertaken to evaluate the performance of fire-rated doors during post-earthquake fires. It contributes to the next-generation design codes. This research illustrated that fire doors in a tall building can experience damage in the form of cracks or openings under large seismic drifts and it is unlikely to detect these damages visually without doing inspections after seismic activity, which, in turn, could impact occupant life safety, emergency response, and property losses during a fire event. Therefore, the time intervals for routine fire door inspections should be reduced and technical investigations should be performed promptly in the aftermath of moderate to major earthquakes, especially in heavily occupied tall buildings. After a comprehensive inspection, decisions addressing the replacement or repair of earthquake-damaged sections of fire doors should be taken within the technical team's expertise. Nevertheless, there is no specification or guideline worldwide specifically regards the professional review of fire doors in the built environments after a certain magnitude of an earthquake. Besides, there is an ongoing need for the proper integration of fire and earthquake hazards in design codes.

To further this research, it is intended to perform the same experimental procedure for various levels of IDRs. The prediction of the damage levels for both earthquake and post-earthquake fire events would be easier by developing fragility curves upon obtaining applicable results for more IDR cases. However, a suitable seismic testing protocol for fire doors that considers their easy disengagement and composite structure is required.

Future work will also focus on modeling and numerical analysis of a fire door assembly in a CFD/FEA platform that is proficient to perform earthquake and fire analyses subsequently.

REFERENCES

1. *An Alternative Procedure For Seismic Analysis and Design of Tall Buildings Located in the Los Angeles Region*, Los Angeles Tall Buildings Structural Design Council, Los Angeles, USA, 2018.

2. Aoki, K., *Door for Buildings*, Official Gazette of the United States Patent and Trademark Office, Vol. 1039, US Patent No 4.429.495, U.S. Government Depository Items Greenville County Library, 1984.

3. *ASCE 41-17: Seismic Evaluation and Retrofit of Existing Buildings*, American Society of Civil Engineers, Reston, Virginia, USA, 2017.

4. *ASTM E564: Standard Practice for Static Load Test for Shear Resistance of Framed Walls for Buildings*, American Society for Testing and Materials International, PA, USA, 2018, http://www.astm.org/cgibin/resolver.cgi?E564.

5. Aydınoğlu, M. N., and Vuran, E., "Development in Seismic Design of Tall Buildings: Preliminary Design of Coupled Core Wall Systems", *Perspectives on European Earthquake Engineering and Seismology*, 2015.

6. Basu, D., and Giri, S., "Accidental Eccentricity in Multistory Buildings Due to Torsional Ground Motion", *Bulletin of Earthquake Engineering*, 2015.

7. Bathe, K. J., and Wilson, E. L., *Numerical Methods in Finite Element Analysis*, Prentice-Hall, Englewood Cliffs, NJ, USA, 1976.

8. Biskinis, D., and Fardis, M. N., "Flexure-controlled Ultimate Deformations of Members with Continuous or Lap-spliced Bars", *Structural Concerete*, 2010.

9. *BS 9999: Code of Practice for Fire Safety in the Design, Management and Use of Buildings*, British Standards, 2008.

10. Chadwell, C. B., and Imbsen, R. A., "XTRACT: A Tool for Axial Force - Ultimate Curvature Interactions", *American Society of Civil Engineers*, Nashville, Tennessee, USA, 2004.

11. Chang, J., Chen, C., and Woo, T., "Performance Test of Window Glass and Metal Door Under Horizontally Cyclic Loading", *13th World Conference on Earthquake Engineering*, Vancouver, BC, Canada, 2004.

12. Chen, C., Chang, J., and Chen, T., 2004, "Earthquake Damage of Window Glass and Door of A Hotel Damaged in The 1999 Chi-Chi Taiwan Earthquake", *13th World Conference on Earthquake Engineering*, Vancouver, BC, Canada.

13. Chen, S., Lee, G. C., and Masanobu S., "Hazard Mitigation for Earthquake and Subsequent Fire", *Multidisciplinary Center for Earthquake Engineering Research*, University at Buffalo-SUNY, USA, 2004.

14. Cheung, S., Lo, S., Yeoh, G., and Yuen, R. K, "The Influence of Gaps of Fire-resisting Doors on the Smoke Spread in A Building", *Fire Safety Journal*, pp. 539-546, 2006.

15. Collier, P. C., *Post-Earthquake Performance of Passive Fire Protection Systems,* BRANZ Study Report 147, Judgeford, Wellington, New Zealand, 2005.

16. Collier, P. C., *Post-Earthquake Performance of Passive Fire Protection Systems,* BRANZ Study Report 304, Judgeford, Wellington, New Zealand, 2013.

17. *Compliance Document for New Zealand Building Code Clauses C1, C2, C3, C4, Fire Safety*, Department of Building and Housing, Wellington, New Zealand, 2011.

18. *CSI Analysis Reference Manual*, Computers and Structures Inc., Berkeley, California, USA, 2017.

19. *CSI PERFORM 3D: Nonlinear Analysis and Performance Assessment for 3D Structures*, vs. 7.0.0, Computers and Structures Inc., Berkeley, California, USA, 2018.

20. Deam, B. L., "Seismic Rating for Residential Timber Buildings", *Building Research Association of New Zealand*, Judgeford, Wellington, New Zealand, 1997.

21. Deirlein, G. G., Reinhorn, A. M., and Willford, W. R., *Nonlinear Structural Analysis For Seismic Design*, National Institute of Standards and Technology, 2010.

22. Elwood, K. J., Pampanin, S., and Kam, W. Y., "22 February 2011 Christchurch Earthquake and Implications for the Design of Concrete Structures", *Proceedings of The International Symposium on Engineering Lessons Learned from The 2011 Great East Japan Earthquake*, Tokyo, 2012.

23. *EN 1363-1: Fire Resistance Tests-Part 1: General Requirements*, European Committee for Standardization (CEN), Brussels, 2012.

24. *EN 1634-1: Fire Resistance Tests for Door and Shutter Assemblies-Part 1: Fire Doors and Shutters*, European Committee for Standardization (CEN), Brussels 2014.

25. *ETABS: Extended 3D Analysis of Building Structures*, vs.16.1.0, Computers and Structures Inc., Berkeley, California, USA, 2017.

26. Faggiano, B., "Fire After Earthquake", *Proceeding from WG1 Meeting*: *Urban Habitat Constructions under Catastrophic Events*, 2007.

27. *FEMA 356: Prestandard and Commentary for the Seismic Rehabilitation of Buildings*, Federal Emergency Management Agency, Washington DC, 2000.

28. *FEMA 461: Interim Testing Protocols for Determining The Seismic Performance Characteristics of Structural and Nonstructural Components*, Federal Emergency Management Agency, Washington DC, 2007.

29. *FEMA E-74: Reducing the Risks of Nonstructural Earthquake Damage – A Practical Guide*, Federal Emergency Management Agency, Washington DC, 2011.

30. Fleming, R., "Analysis of Fire Sprinkler System Performance in The Northridge Earthquake", *National Institute of Standards and Technology*, Gaithersburg, 1998.

31. Forcael, E., Gonzalez, V., Orozco, F., Opazo, A., Belmar, C., & Vera, J., "Study of Structural Capacity and Serviceability Affecting the Obstruction of Residential Door", *Latin American Journal of Solids and Structures*, pp. 410-436, 2014.

32. Fu, F., *Fire Safety Design for Tall Buildings*, CRC Press, Taylor & Francis Group, 6000 Broken Sound Parkway NW, Suite 300, Boca Raton, FL 33487-2742, 2021.

33. Hoehler, M., Lutz, C., and Schulze, P., "Testing Passive Fire-resistance Systems for Fire Follow Earthquakes", *American Society of Civil Engineers*, 2012.

34. Hurley, M. J., *SPFE Handbook of Fire Protection Engineering*, Springer, Greenbelt, MD, USA, 2016.

35. *Guidebook for Design and Practice of Fire Compartment*, The Architectural Institute of Japan, 1990.

36. *Investigation Report on Damages to Fire Protection Systems Caused by the Hanshin-Awaji Earthquake in Kobe*, Kobe City Department, 1995.

37. *ISO 834-1: Fire-resistance Tests - Elements of Building Construction - Part 1: General Requirements*, International Organization for Standards, Geneva, 2017.

38. Kelly, P., *Mechanics Lecture Notes: An Introduction to Solid Mechanics*, http://homepages.engineering.auckland.ac.nz/~pkel015/SolidMechanicsBooks/index.html, Accessed on February 2021.

39. Khorasani, N. E., and Garlock, M. E., "Overview of Fire Following Earthquake: Historical Events and Community Responses", *International Journal of Disaster Resilience in the Built Environment*, pp. 158-174, 2017.

40. Kumar, R. P., Murty, C. V., Vijayanarayanan, A. R., and Mehta, V. V., *Introduction to Earthquake Protection of Nonstructural Elements in Buildings*, Gujarat State Disaster Management Authority, Gandhinagar, 2012.

41. LeGrone, P., "An Analysis of Fire Sprinkler System Failures During The Northridge Earthquake and Comparison with The Seismic Design Standard for These Systems", *13th World Conference on Earthquake Engineering*, Vancouver, 2004.

42. Lowes, L., Lehman, D. E., and Baker, C., *Recommendations for Modeling the Nonlinear Response of Slender Reinforced Concrete Walls Using PERFORM-3D*, University of Washington, Seattle, WA, 2018.

43. Mander, J. B., Priestley, M. J., and Park, R., "Theoretical Stress-Strain Model for Confined Concrete", *American Society of Civil Engineers*, pp. 1804-1826, 1988.

44. Meacham, B. J., Kim, J., and Park, H., "Shake Table Testing of A Full-scale Five-story Building: Post-earthquake Fire Performance", *Structures Congress 2013: Bridging Your Passion with Your Profession*, 2013.

45. Meacham, B. J., "Post-Earthquake Fire Performance of Buildings: Summary of a Large-Scale Experiment and Conceptual Framework for Integrated Performance-Based Seismic and Fire Design", *Fire Technology*, pp. 1133-1157, 2016.

46. Miranda, E., and Taghavi, S., "Estimation of Seismic Demands on Acceleration-sensitive Nonstructural Components in Critical Facilities", *The Seminar on Seismic Design, Performance, and Retrofit of Nonstructural Components in Critical Facilities*, ATC 29−2, pp. 347-360, 2003.

47. Miranda, E., and Cruz, C., "Damping Ratios in Tall Buildings Inferred From Instrumented Tall Buildings in California", *International Workshop on Performance-Based Seismic Design of Structures*, Tongji University, Shanghai, China, 2017.

48. Moehle, J. P., "Strong Motion Drift Estimates for R/C Structures", *American Society of Civil Engineers*, 1984.

49. Moehle, J. P., "Displacement-Based Design of RC Structures Subjected to Earthquakes", *Earthquake Spectra*, pp. 403-428, 1992.

50. Naish, D., Fry, A., Klemencic, R., and Wallace, J. W., *Experimental Evaluation and Analytical Modeling of ACI 318-05/08 Reinforced Concrete Coupling Beams Subjected to Reversed Cyclic Loading*, UCLA SGEL Report 2009/06, University of California, Los Angeles, 2009.

51. *NFPA 80: Standard for Fire Doors and Other Opening Protectives*, National Fire Codes, National Fire Protection Association, 2019.

52. Orakçal K., *CE.58K Performance-Based Design for Tall Buildings Lecture Notes*, Bogazici University, Bebek, Istanbul, 2020.

53. Pantoli, E., Chen, M. C., Wang, X., Astroza, R., Ebrahimian, H., Hutchinson, T. C., Conte, J. P., Restrepo, J. I., Marin, C., Walsh, K. D., Bachman, R. E., Hoehler, M. S., Englekirk, R., and Faghihi, M., "Full-Scale Structural and Nonstructural Building System Performance During Earthquakes: Part II–NCS Damage States", *Earthquake Spectra*, 2016.

54. *PEER/ATC 72-1: Modeling and Acceptance Criteria for Seismic Design and Analysis of Tall Buildings*, Pacific Earthquake Engineering Research Center, Redwood City, California, 2010.

55. *PEER Next Generation Attenuation-West2*, Pacific Earthquake Engineering Research Center, 2013, http://ngawest2.berkeley.edu/, Accessed on February 2021.

56. *PEER/TBI: Tall Buildings Initiative: Guidelines for Performance-Based Seismic Design of Tall Buildings Version 2.03*, Pacific Earthquake Engineering Research Center, California, 2017.

57. Plevris, V., Kremmyda, G., and Fahjan, Y., *Performance-Based Seismic Design of Concrete Structures and Infrastructures*, Advances in Civil and Industrial Engineering, IGI Global, Hershey PA, USA 17033, 2017.

58. Porter, K. A., Kiremidjian, A. S., & Le Grue, J. S., "Assembly-based Vulnerability of Buildings and Its Use in Performance Evaluation", *Earthquake Spectra*, 17(2), pp. 291-312, 2001.

59. Powell, G. H., *Modeling for Structural Analysis, Behavior and Basics,* Computers and Structures Inc., Berkeley, California, 2010.

60. *Report of The 1995 Hyogo-Ken Nanbu Earthquake,* Fire and Disaster Management Agency, 2006.

61. Rezaeian, S., Bozorgnia, Y., Idriss, I. M., Campbell, K., Abrahamson, N., and Silva, W., *Spectral Damping Scaling Factors for Shallow Crustal Earthquakes in Active Tectonic Regions*, Pacific Earthquake Engineering Research Center, Berkeley, 2012.

62. Scawthorn, C., *Fire Following Earthquakes, Earthquake Engineering Handbook*, CRC Press, pp. 1244-1308, Florida, 2003.

63. Scawthorn, C., Eidinger, J., and Schiff, A., "Fire Following Earthquake, Technical Council on Lifeline Earthquake Engineering Monograph", *American Society of Civil Engineers*, 26. Reston, VA, 2005.

64. Scawthorn, C., *Fire Following Earthquake*, United States Geological Survey, USA, 2008.

65. Sekizawa, A., Ebihara, M., and Notake, H., "Development of Seismic-induced Fire Risk Assessment Method for A Building", *Proceedings 15th Meeting of the UJNR Panel and Fire Research and Safety*, pp. 145-152, San Antonio, 2000.

66. Sekizawa, A., Ebihara, M., & Notake, H., "Development of Seismic-induced Fire Risk Assessment Method for A Building", *Fire Safety Science, Proceedings of The Seventh International Symposium*, pp. 309-320, 2003.

67. Sharp, G. S., *Earthquake Damage to Passive Fire Protection Systems in Tall Buildings and Its Impact on Fire Safety*, Master's Thesis, University of Canterbury, Department of Civil Engineering, Christchurch, New Zealand, 2003.

68. Sharp, G. S., and Buchanan, A. H., "Earthquake Damage to Passive Fire Protection Systems in Tall Buildings", *New Zealand Society for Earthquake Engineering Conference*, 2004.

69. Soroushian, S., Maragakis, E., Zaghi, A. E., Echevaria, A., Tian, Y., and Filiatrault, A., *Comprehensive Analytical Seismic Fragility of Fire Sprinkler Piping Systems,* Technical Report MCEER-14-0002, University at Buffalo-SUNY, USA, 2014.

70. Taylor, J. M., *Post-Earthquake Fire in Tall Buildings and The New Zealand Building Code*, Master's Thesis, University of Canterbury, Department of the Civil Engineering, Christchurch, New Zealand, 2003.

71. *TS498: Design Loads for Buildings*, Turkish Standards Institute, Ankara, Turkey ,1997.

72. *TS500: Requirements for Design and Construction of Reinforced Concrete Structures*, Turkish Standards Institute, Ankara, Turkey, 2000.

73. *Turkish Earthquake Hazard Map*, AFAD (Disaster and Emergency Management Presidency), Ankara, Turkey, 2017, https://tdth.afad.gov.tr/, Accessed on February 2021.

74. *Turkish Building Seismic Code*: *Specifications for Design of Buildings Under Earthquake Action,* Disaster and Emergency Management Presidency, Ankara, Turkey, 2018.

75. Usami, T., *Nihon Higai Jishin Soran (List of Damaging Japanese Earthquakes)*, University of Tokyo, Tokyo, Japan, 1996.

76. *User Guide Perform 3D-Nonlinear Analysis and Performance Assessment for 3D Structures*, Computers and Structures Inc., Berkeley, California, USA, 2018.

77. Wang, X., Hutchinson, T., Hegemier, G. A., Gunisetty, S., Kamath, P., and Meacham, B., *Earthquake and Fire Performance of A Mid-rise Cold-formed Steel Framed Building-Test Program and Test Results: Final Report*, University of California, San Diego, Department of Structural Engineering, La Jolla, California, 2016.

78. Willford, M., Whittaker, A., and Klemencic, R., "Recommendations for the Seismic Design of High-rise Buildings", *Council on Tall Buildings and Urban Habitat*, 2008.